Fabrication and Characterisation of Epitaxial PMN-PT Nano-structures

Thèse N° 7450

Présentée le 17 décembre 2019

à la Faculté des sciences et techniques de l'ingénieur
Groupe SCI STI PM
Programme doctoral en microsystèmes et microélectronique

pour l'obtention du grade de Docteur ès Sciences

par

Xiao DI

Acceptée sur proposition du jury

Prof. J. Brugger, président du jury
Prof. P. Muralt, Prof. D. Damjanovic, directeurs de thèse
Dr M.-A. Dubois, rapporteur
Prof. K. Dörr, rapporteuse
Dr I. Stolichnov, rapporteur

2019

EPFL
ÉCOLE POLYTECHNIQUE
FÉDÉRALE DE LAUSANNE

Do the difficult things while they are easy
and do the great things while they are small.
A journey of a thousand miles must begin
with a single step.
— Lao Tzu

天下难事必作于易，天下大事必作于细。
千里之行，始于足下。
—老子

Acknowledgements

First of all, I would like to thank my thesis advisor Prof. Paul Muralt, who offered me the opportunity to do my Ph.D and has given me every support throughout my thesis work. I sincerely appreciate Paul's guidance with his abundant scientific expertise and patience to help me on this new direction of my study. I always appreciate how much I have learnt from him in terms of critical thinking and problem solving. When I looked back the past four years, there were too many times that I went to him with bad results and failures in instruments. He always encouraged me and even dedicated so much time with me to repair the tools. I feel lucky to work with him.

I would thank my co-advisor, Prof. Dragan Damjanovic. I learnt from him a lot on fundamentals of piezoelectric and ferroelectric materials. I must also thank him for his supervision and generous support in the last few months of my Ph.D, when Paul was retired.

I also want to thank Prof. Brugger Jürgen, Dr. Stolichnov Igor, Dr. Dubois Marc-Alexandre from CSEM and Prof. Dörr Kathrin from University of Halle for being the jury members. Their discussions and comments were inspiring for me to improve the thesis report.

I would like to thank all the colleagues from former Ceramic lab, Electroceramic thin films group and Group for ferroelectrics and functional oxides. Their trainings and great experience helped me a lot in many experimental works. Barbara Fraygola and Arnaud Crassous helped me to start my work on pulsed laser deposition. Cosmin Sandu performed many times SEM and TEM measurements. Chu Kanghyun helped me on piezoresponse force microscopy measurement. Park Daesung travelled to Germany to measure XRD of our samples. And so on. There were too much kindness and dedication from them that I could not mention all here. I also enjoyed the working time and beer time with other colleagues: Meurisse Thibaut, Yamashita Kaoru, Stefan Mertin, Vladimir Pashchenko, Andrea Mazzalai, Clemens Nyffeler, Riemer Lukas, Sina Hashemi Zadeh, Hadad Mahmoud, Fazel Parsapour, Zhuo Fangping, Zhou Yaming, Huang Zhen, Zhang Meng and Meng Xiangda. I must thank in particularly Nigon Robin and Ramin Matloub, who have been my officemates so nicely in the past four years, for their countless help in work and daily life. I am grateful to Lino Olivetta for his support on lab orders and Yuko Kagata for her constant help on administrative matters.

A lot of the fabrication of samples was done in the EPFL Center of MicroNanotechnology (CMi). Therefore, I would like to thank the support from all staff of CMi. In particular, I appreciate Benes Zdenek for the techniques he taught me and the help on improving the electron beam lithography process.

Lausanne 25. November. 2019   邸啸   DI Xiao

Abstract

Downscaling of the minimal feature size, or the gate length has been the key for the exponential improvement of the performance of the logic CMOS integrated circuits over the last six decades. However, since about 2003, some fundamental limits in the device physics were reached. Further scaling with increased clock speed at lower voltage was limited by excessive increase of power consumption and noise. This challenge motivated numerous efforts to search for next generation transistors. The piezoelectronic transistor (PET), based on piezoelectricity and piezoresistivity, is one of the proposed devices. In this work, we seek to contribute to the scaling of ferroelectrics lead magnesium niobate – lead titanate xPb(Mg$_{1/3}$Nb$_{2/3}$)O$_3$-$(1-x)$PbTiO$_3$ (PMN-PT) for PET applications.

The first important issue is the deposition of high quality epitaxial PMN-PT films. We studied the two film compositions 60/40 and 67/33, which are at the morphotropic phase boundary (MPB) and slightly in the tetragonal phase. A process of growing epitaxial (001)-oriented PMN-PT thin films on SrRuO$_3$-buffered SrTiO$_3$ substrates by pulsed laser deposition was developed. The deposition conditions, such as substrate temperature, O$_2$ pressure, target compositions were optimized for achieving smooth and phase pure perovskite thin films.

The patterning process for damage-free nanostructures of PMN-PT was subsequently investigated. Pattern transfer was carried out with electron beam lithography (eBL) with the goal to reach sub-100 nm structures. We developed a novel lift-off technique consisting in using a bilayer mask incorporating the electron-beam resist hydrogen silsesquioxane (HSQ) on top of amorphous aluminum oxide (AlO$_x$). The bilayer mask forms undercut profile and is thermally stable at the high temperature deposition process. Epitaxial PMN-PT/SrRuO$_3$ heterostructures were grown inside the mold of AlO$_x$. The lift-off was performed in NaOH aqueous solution, leaving untouched the arrays of PMN-PT/SrRuO$_3$ nanostructures. The film structures grown inside the openings follows the shape of the mold, producing the obtuse angle at the edge of the nanostructure. The thickness of the nanostructures varied with the width of the openings, and is less than the thickness of plain films. We developed a model to predict the thickness of the nanostructures. The minimum features fabricated with this method have a lateral size of 70 nm. The crystalline of the nanostructures were studied with Transmission electron microscopy (TEM).

Piezoresponse force microscopy (PFM) revealed a clear polarization switching of the patterned, 12 to 15 nm high PMN-PT nanostructures with a piezoelectric response that was larger than ~10 pm/V and possibly reaching even ~150 pm/V, Furthermore, short-range (10 – 20 nm) ferroelectric domain patterns prominently appear after poling the nanostructured ferroelectrics, indicating the coexistence of tetragonal *a*- and *c*-domains, mixed with fewer rhombohedral domains. The presented nanofabrication method enables to step towards nanoscale engineering of ferroelectrics for the advancement of efficient electromechanical device applications.

Keywords

Résumé

La diminution de la taille minimale résolvable et de la longueur de grille ont été la clé de l'augmentation exponentielle des performances des circuits logiques intégrés de type CMOS durant les 6 dernières décennies. Cependant, depuis environ 2003, certaines limites fondamentales de la physique des circuits ont été atteintes. La poursuite de la miniaturisation, avec une vitesse d'horloge plus élevée et un voltage plus faible, a été freinée par l'augmentation excessive de la consommation d'énergie et du bruit. C'est ce qui a motivé les nombreux efforts de recherche sur les transistors nouvelle génération. Le transistor piézoélectronique (*piezoelectronic transistor* ou PET en anglais), basé sur l'effet piézoélectrique et la piézorésistivité, est l'une des solutions proposées pour relever ce défi. Dans ce travail de thèse, nous cherchons à contribuer à la miniaturisation de la technologie du niobate-magnésium de plomb – titanate de plomb xPb(Mg$_{1/3}$Nb$_{2/3}$)O$_3$-(1− x)PbTiO$_3$ (PMN-PT) pour les applications de PET.

Le premier défi consiste en le dépôt de films épitaxiaux de PMN-PT de haute qualité. Nous avons étudié deux films de composition différente, 60/40 et 67/33, qui sont chacune au niveau de la transition de phase morphotropique et légèrement tétragonales. Nous avons développé un procédé de dépôt par laser pulsé (*pulsed laser deposition* ou PLD) de couches épitaxiales de PMN-PT, texturées (100), sur des substrats de SrTiO$_3$ avec une couche tampon de SrRuO$_3$. Les paramètres de dépôt, tels que la température du subtrat, la pression d'oxygène, ou la composition de la cible, ont été ajustés afin d'obtenir des couches minces lisses et de phase purement perovskite.

Nous avons ensuite étudié le procédé de structuration pour réaliser des nanostructures sans défaut de PMN-PT. La structuration a été réalisée à l'aide du procédé de lithographie par faisceau d'électrons (*electron beam lithography* ou eBL) dans le but d'obtenir des structures de taille inférieure à 100nm. Nous avons développé une nouvelle technique de lift-off qui consiste en l'utilisation d'un masque à double couche : une couche de résine pour faisceau d'électrons, l'hydrogénosilsesquioxane (HSQ), superposée à une couche d'oxyde d'aluminium amorphe (AlO$_x$). Le masque double-couche forme un profil en surplomb et est thermiquement stable à la température élevée du procédé. Des hétérostructures épitaxiales de PMN-PT/SrRuO$_3$ ont été déposées dans le moule formé par l'AlO$_x$. Le lift-off a été réalisé dans une solution aqueuse de NaOH, qui n'attaque pas les nanostructures de PMN-

PT/SrRuO$_3$. Ces structures croissent en prenant la forme du moule dans lequel elles sont déposées, ce qui produit un angle obtus au bord des nanostructures. L'épaisseur des nanostructures varie avec la largeur des ouvertures et est inférieure à l'épaisseur nominale de la couche. Un modèle pour prédire l'épaisseur des nanostructures a été développé. La plus petite dimension latérale que nous avons pu réaliser par cette méthode est de 70nm. La cristallinité des nanostructures a été étudiée au microscope électronique à transmission (*transmission electron microscope* ou TEM).

L'imagerie au microscope à retour de force piézoélectrique (piezoresponse force microscope ou PFM) a révélé une claire bascule de polarisation au sein des nanostructures de 12nm à 15nm d'épaisseur de PMN-PT, avec une réponse piézoélectrique supérieure à ~10pm/V, et qui peut-être atteint les 150pm/V. De plus, des domaines ferroélectriques de petite dimension (10 à 20nm) apparaissent après la polarisation des nanostructures ferroélectriques, indiquant la coexistence de domaines tétragonaux de types *a* et *c*, mélangés avec un plus petit nombre de domaines rhomboédriques. La méthode de nanostructuration que nous avons présentée est un pas de plus vers la nanostructuration des matériaux ferroélectriques, pour le perfectionnement des applications de systèmes électromécaniques efficients.

Mots-clés

Acronyms

AC   Alternate Current

CMOS   Complementary Metal-Oxide-Semiconductor (CMOS)

DC   Direct Current

PET   Piezoelectronic Transistor

PFM   Piezoresponse Force Microscope

TEM   Transmission Electron Microscopy

SEM   Scanning Electron Microscope

PMN-PT Lead Magnesium Niobate-Lead Titanate

PLD   Pulsed Laser Deposition

PZT   Lead Ziconate Titanate

HSQ   Hydrogen silsesquioxane

eBL   electron Beam Lithography

STO   Strontium Titanate

MEMS   Micro Electro Mechanical System

RSM   Reciprocal space mapping

XRD   X-ray Diffraction

Contents

List of Figures

List of Tables

Chapter 1   Introduction

1.1   Background

Over the past three decades, the success of Complementary Metal-Oxide-Semiconductor (CMOS) field effect transistors (FETs) technology scaling has provided denser and faster integrated circuits and thus provided the primary driving force of microelectronics industry. Following roughly the predictions of Moore's law and Dennard scaling theory, the transistors shrank relentlessly, offering increased processing speed at lower power consumption at each miniaturization step [1], [2].

However, after decades of exponential increase of the clock frequency, the year 2003 marked a break when a further increase became impossible [3]. The cause lies in a breakdown of the simple constant-electric-field scaling rule that had guided the voltage scaling [2]. The 'leakage current' and the 'threshold voltage', which establish a base line of power per transistor, become crucial after 65 nm technology node since 2005 and cannot be neglected anymore. As is well known, the power consumption of CMOS chips can be modeled in a simplified way,

$$P = NfCV^2 + VI_{\text{leakage}} \tag{1.1}$$

N is the number of transistors, f is operation frequency, C is the capacitance of the gate, V is the core voltage, and I_{leakage} is the leakage current.

A minimum gate voltage swing is necessary to switch the device from an "OFF" (low-current) to an "ON" (high-current) state [3]. Supply voltages could not be further reduced but got stuck at about 1 V to avoid too small ON/Off current ratios [4]. The increase of frequency is not possible anymore since a while already, as the power consumption is linearly increasing with it if not compensated by a voltage decrease.

The FETs are rapidly approaching the ultimate physical limits, inducing the breakdown of Dennard's scaling rules. Further shrinking of transistor foot prints is facing ever more difficulties and becomes less rewarding.

Discovery of a fast, low power switching device, based on a different operation principle, is thus crucial to a continuing vigor of the information technology industry.

A number of alternative approaches are under current investigation, including tunnel transistors [5]–[7], spin-FET [8] and nano-electro-mechanical (NEM) switch [9], etc. However, none of these devices has so far demonstrated adequate ON/OFF ratio under low operating voltage combined with the requirements for competitive switching speed [10].
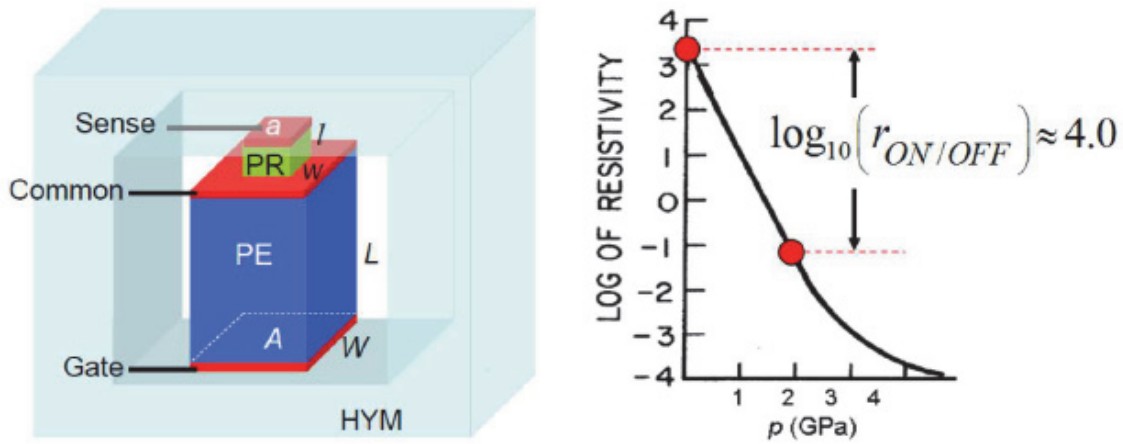
Figure 1.1- Left: The PiezoElectronic Transistor (PET), showing Piezoelectric (PE), Piezoresistor (PR), and Gate, Common and Sense contacts. The device is surrounded laterally by an air gap and above/below by a constraining yoke consisting of a high-yield strength material (HYM); Right: log10(resistivity) vs. pressure plot for a PR, SmSe. Figure taken from Reference [11].

Since 2012, a research group from IBM started to develop a disruptive transduction device, namely the piezoelectronic transistor (PET) [4], [10]–[13] as illustrated in Figure 1(a), to use piezoelectric force to control the resistivity of a piezo-resistive channel. The input voltage between "Gate" and common terminal is applied across a piezoelectric element (PE), which acts as an actuator, transducing the input voltage into an acoustic (or mechanical stress) pulse. The acoustic pulse gates a continuous insulator-to-metal (IMT) phase transition in the "channel" of the device, which consists of a

highly pressure-sensitive piezoresistive (PR) material, enabling the conductive path between the "Sense" and the common terminal. This chain of action is summarized in Figure 1.2 [4].
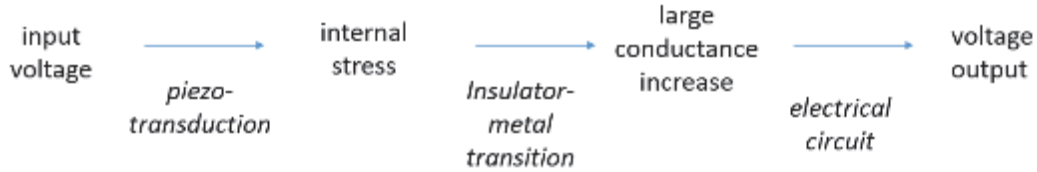
Figure 1.2 – The action procedure of a piezoelectronic transistor.

This novel type of electronic switch has been modelled to combine and realize all of the logic functions employed in CMOS circuits [10], [13].

From the materials aspects, a strong yoke of high yield strength medium (HYM; e.g. SiN) is needed to support the whole structure and compressing the PR layer sufficiently. Besides, PET devices require high performance PE and PR materials. The PR part requires a resistivity change of several orders of magnitude to fulfil adequate I_{ON}/I_{OFF} ratio at low applied pressure. According to the model, it was predicted that with a supply voltage of 0.1 V (V_{DD}), an ON/OFF ratio of 4 orders of magnitude could be reached for the resistance variation within 2 GPa stress, as shown in Figure 1(b). Possible IMT candidates are found in rare earth mono chalcogenides such as SmSe studied by IBM. Other group reported epitaxial films of the Mott insulator Sr_2IrO_4 as a viable oxide for piezoelectronics, showing a pressure-induced, fully reversible, orders of magnitude modulation of giant piezoresistance at room temperature [14].

As for the PE material, a high piezoelectric coefficient d_{33}, which must be stable at high strain levels, is required to yield the high stress applied onto the piezoresistor at a given applied electric field [15]. Notice that the contact area difference between PR and PE parts could also help on this matter, via an effect similar to the relationship between a hammer and a nail. As can be seen from the schematic view of the device, the contact area of PE is much larger than the PR part, to ensure amplifying the pressure applied on the PR.

The recent breakthrough of materials synthesis and structuration techniques make it possible to integrate piezoelectric materials into microsystems structures [16]–[19]. One of the most notably piezoelectric material is $Pb(Zr,Ti)O_3$ (PZT), in both thin-film and bulk ceramics form [18], [20], [21]. Despite that polycrystalline materials dominate thin-film forms, epitaxial films offer a number of advantages, such as the possibility of lower leakage due to the absence of grain boundaries and improved piezoelectric properties (see Figure 2) [22], [23].
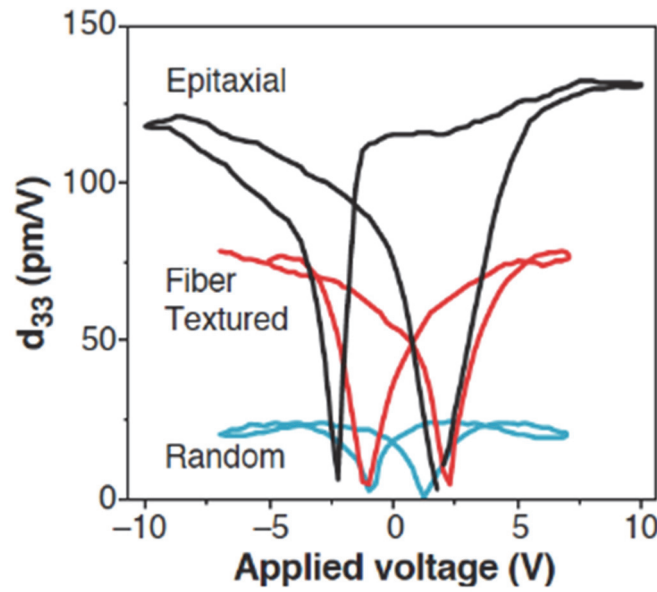
Figure 1.3 - Piezoelectric properties d_{33} taken from different forms of PZT film showing the importance of film orientation [22].

The proposed PE material for PET is $(1-x)[Pb(Mg_{1/3}Nb_{2/3})O_3]-x[PbTiO_3]$ (PMN-PT) owing to its giant piezoelectric properties. PMN-PT is a solid solution of relaxor (PMN) and normal ferroelectric (PT). It excels with particularly high dielectric and piezoelectric constants [24]. This is in part due to the compositional choice of $x = 0.32$ at a morphotropic phase boundary in (001) oriented PMN-PT with its shallower minima for the spontaneous polarization [19], [25] (see Figure 3), and in part due to the contribution of nano-polar regions (PNR) formed by the statistical disorder of Mg^{2+} and Nb^{5+} ions centering the oxygen octahedra [26]. The piezoelectric coefficient and giant strain levels (~1.7%) could be 5 to 10 times those of best textured PZT ceramics [19]. The larger piezoelectric response of PMN-PT for PE would enable further miniaturization. In fact, the PET devices need to scale down

the piezoelectric material to 20 nm or below. The challenges are not only the difficulties in the synthesis of high-quality epitaxial PMN-PT thin films, but also in fabricating small 3D structures.
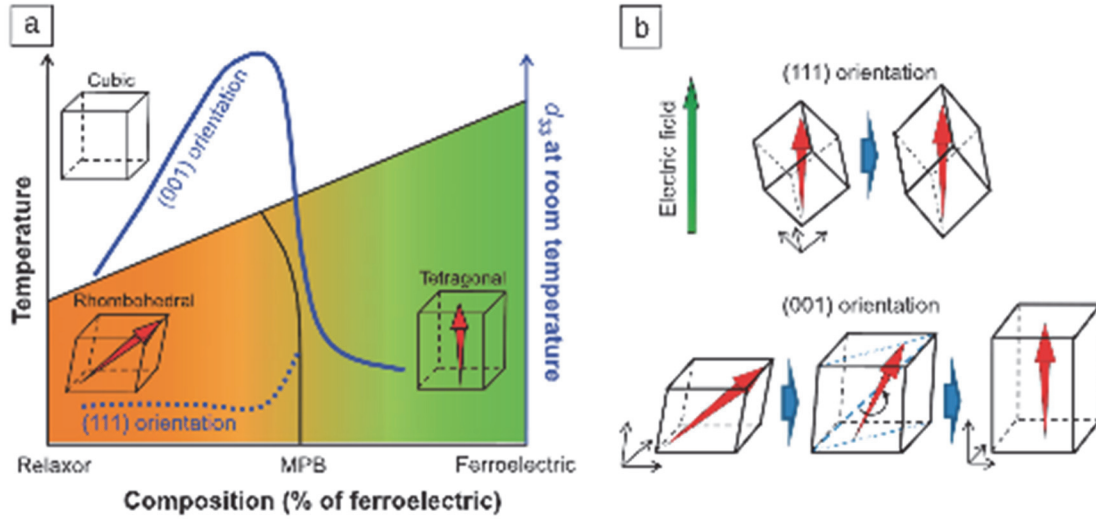
Figure 1.4 - (a) Schematic phase diagram of giant piezoelectric relaxor-ferroelectrics. The solid and dotted blue lines represent the longitudinal piezoelectric coefficients in (001) and (111) relaxor-ferroelectric single crystals, respectively. d_{33}, a longitudinal piezoelectric coefficient, is the mechanical displacement along the applied electric field direction. (b) Schematic illustration of electric-field induced phase transition via polarization rotation from rhombohedral to tetragonal structure as an origin of huge strain level ($\approx$1.7% in bulk single crystals). The red arrow represents the polarization direction. Figures are taken from Reference [19].

There are several conditions which must be satisfied for obtaining giant piezoelectric properties in PMN-PT [19].

First, the phase of PMN-PT should be pure perovskite phase. It is quite often the pyrochlore phase of $Pb_2Nb_2O_7$ that appears in PMN-PT thin film synthesis. This is because it is more stable than perovskite phase. The piezoelectric properties would be decreased with the non-piezoelectric second phase.

Second, as in other solid solution of piezoelectric materials, the piezoelectric response depends on composition and is largest near morphotropic phase boundary (MPB). In the temperature versus composition phase diagram, this phase boundary separates the rhombohedral (PMN-rich side) and tetragonal symmetry (PT-rich side). For bulk PMN-PT, the optimal concentration is 2/3 PMN and 1/3 PT. As shown in Figure 3, the piezoelectric response of PMN-PT is largest in the rhombohedral symmetry close to the MPB.

Third, PMN-PT should be a single crystalline and (001)-orientated. The giant piezoelectricity is normally explained by the polarization model. The large strain levels in bulk single crystals originate from the electric field induced phase transition. For PMN-PT with composition in the vicinity of the MPB, such polarization rotation toward [001] easily destabilizes the rhombohedral ground state, resulting in a phase transition to the tetragonal structure. When the tetragonal phase is driven by an electric field from the rhombohedral ground state, additional room for further strain is provided, increasing the maximum strain level, as shown in Figure 3b.

Finally, PMN-PT must be exact in the stoichiometry. Particularly at high growth temperature, lead oxide (PbO) is likely volatile and leads to off-stoichiometry film. This results in electrical leakage in thin film as well as formation of lead-deficient second phases and detrimental grain boundaries.

PMN-PT thin films can be grown by sputtering, pulsed laser deposition (PLD) and by chemical solution deposition technique, and are studied since a number of years. The main difficulty in the synthesis is the extreme sensitivity of thin film properties to the growth parameters. Among these deposition techniques, numerous features make PLD attractive including stoichiometric transfer of material from a multicomponent target regardless of the chemistry, generated energetic species and compatibility within a wide pressure range (high vacuum – 1 Torr chamber pressure) [27], [28].

The aim of the thesis is to study the downscaling of PMN-PT. Patterning PMN-PT nanostructures is important for both theoretical and applications aspects. Firstly, nanostructures of tens of nanometers would offer a platform to study the hypothesized PNRs thought to have a size of a few nanometers [16], [29]. Secondly, nanostructures and ultrathin films of PMN-PT might be of interest for nanoelectronic devices, such as PET, and nano-electromechanical systems (NEMS).

1.2   Outline of the thesis

The main techniques of processing and characterizations employed in the thesis are briefly discussed in Chapter 2. This background chapter also includes material property of PMN-PT.

The developed deposition process of high-quality epitaxial PMN-PT on (001) oriented $SrTiO_3$ substrate by PLD is discussed in Chapter 3.

Most often, the patterning of PMN-PT is realized with 'top down' approaches through wet etching with strong acids or plasma-based dry etching processes. However, both methods have been reported to induce defects and impurities at interfaces and at the side walls. [30], [31]. These defects critically degrade the piezoelectric and ferroelectric properties of thin films. In this work, we develop a process that employs a lift-off technique to pattern PMN-PT/$SrRuO_3$ heterostructures. A sacrificial layer of amorphous aluminum oxide (AlO_x) [31] and high-resolution electron beam resist of hydrogen silsesquioxane (HSQ) were utilized. After exposure, HSQ has an amorphous structure similar to SiO_2 and becomes relatively insoluble in alkaline hydroxide developers. AlO_x can be isotropically etched with alkaline solutions such as NaOH or TMAH. As a result, TMAH etches AlO_x through the openings in the developed HSQ. An undercut structure is formed, which is suitable for lift-off processes. After having formed the lift-off mask, an epitaxial PMN-PT/SRO layer stack was deposited by pulsed laser deposition at a temperature of 575°C and 625°C respectively. In this temperature range, AlO_x is stable. It does not crystallize and remains soluble in alkaline solutions. We neither observed a chemical reaction with PMN-PT. Chapter 4 of this thesis presents the fabrication process of patterned PMN-PT/$SrRuO_3$ heterostructures with down to 50 nm diameter features on (001) $SrTiO_3$ substrates.

The crystalline and microstructures of the heterostructures were characterized in detail with X-ray diffractions (XRD) and transmission electron microscope (TEM) techniques. The XRD results reveal the successful growth of $SrRuO_3$ and perovskite phase of PMN-PT in both the plane film sample and the patterned film sample. No traces of a pyrochlore phase of PMN-PT were found. Reciprocal space mapping (RSM) of the samples was carried out to characterize also the in-plane lattice constant[32] of the plain and the structured film. The film exhibited a tetragonal symmetry. The $SrRuO_3$ layers were found to have grown coherently on the $SrTiO_3$ substrate. A combination of TEM and energy dispersive spectroscopy (EDS) was used to analyze the heterostructure chemical composition and its spatial distribution. From one typical sample, the ratio of PMN and PT was about 64/36, which is slightly lower than the value of 67/33 of the target. The ratio between Pb and the total amount of Nb,

Ti and Mg was measured as 0.87, indicating a lead deficiency due to lead loss during deposition. The ratio between Nb and Mg was obtained as 2.11, which deviates only by 5 % from the expected value of 2. The obtained composition indicated that the film was in the tetragonal state. This confirms the XRD data.

Chapter 5 is designated to the ferroelectric properties of PMN-PT film and nanostructures studied using piezoresponse force microscopy (PFM). The patterned PMN-PT nano platelet exhibited good ferroelectric behavior, as the polarization could be defined by the tip, complete regions could be switched, and rewritten in films that are only 12 nm thick. The coercive voltage amounted to about 4.0 V.

Realizing the proposed PET device requires deeper understanding of the PMN-PT piezoelectric response, especially at the nano patterned structures. This thesis address process and fundamental question in scaling of ferroelectrics and contribute to the PET technology. Recommendations and outlook for processing and characterizations of ferroelectric thin films are presented in Chapter 6. The potential application of lift-off method in NEMS is also addressed.

Chapter 2 State of the art and experimental techniques

This chapter gives an introduction to ferroelectric materials, as well as to some experimental techniques. In section 2.1, a brief overview on ferroelectric materials, and on the evolution of ferroelectric technology are presented. Section 2.2 introduces the perovskite material PMN-PT, the ferroelectric of interest in this thesis. The review covers the perovskite structure, relaxor ferroelectrics, the phase diagram of PMN-PT, and explains why PMN-PT is the material of choice. Section 2.3 discusses epitaxial thin film nucleation and growth, followed by an introduction to PLD techniques in section 2.4. Section 2.5 presents the technique to prepare atomically flat $SrTiO_3$ substrates, which is essential for epitaxal growth. In this thesis, the grown thin films are structurally and chemically characterized by scanning electron microscopy (SEM), transmission electron microscopy (TEM), and energy dispersive X-ray spectroscopy (EDS). These techniques are briefly described in sections 2.6 and 2.7. The surface morphology is imaged by atomic force microscopy (AFM). An extension of this technique, the piezoelectric responsive AFM is used for functional characterization (section 2.8). Finally, the techniques and instruments employed for patterning, i.e. electron beam lithography are presented in section 2.9.

2.1 Thin-film ferroelectric materials: overview and their applications

Ferroelectricity was discovered at the (already known) piezoelectric crystal of Rochelle salt ($KNaC_4H_4O_6 \cdot 4H_2O$) by Valasek in 1920. He discovered, that there is a spontaneous, internal electric polarization that can be switched by applying an external electric field. The phenomenon is called ferroelectricity in analogy to the spontaneous magnetization in ferromagnetic materials. It is notable here that a ferroelectric does not need to contain iron, in spite of the prefix "ferro".

The modern era of ferroelectricity is closely related to the development of new piezoelectric and high dielectric constant (high-K) materials. Much progress was made during the Second World War, which

accelerated the development of functional materials for submarine detection (sonar sensors with Rochelle salt and later $BaTiO_3$), and $BaTiO_3$ as high-K ceramics for RF applications. $BaTiO_3$ was the first synthesized perovskite ferroelectric oxide. Initial studies of ferroelectric thin films were triggered to develop non-volatile memories already in the 1960s [33]. However, difficulties in the synthesis of high-quality films and their integration limited the attempts until the 1980s. The exploration for better piezoelectric and ferroelectric materials resulted in the discovery of lead zirconate titanate (PZT) in 1952. This compound is a solid solution of $PbTiO_3$ (PTO) and $PbZrO_3$ (PZO). It has outstanding piezoelectric properties and a relatively high Curie temperature (T_c), making it the most widely employed piezoelectric material to date. On the theoretical side, the physicists Landau, Ginzburg and Devonshire managed to describe the phase transitions in ferroelectric crystals in terms of the internal electrical polarization as order parameter in the 1950's.

In 1997, S. E. Park and T. R. Shrout reported relaxor based ferroelectric single crystals, such as $Pb(Zn_{1/3}Nb_{2/3})O_3$-$PbTiO_3$ and $Pb(Mg_{1/3}Nb_{2/3})O_3$-$PbTiO_3$ with ultrahigh strain up to 1.7% and a large electromechanical coupling coefficient of $k_{33} \approx 0.9$. These crystals show an order of magnitude larger piezoelectric response than PZT. This is in part due to the compositional choice of $x = 0.32$ at a morphotropic phase boundary with its shallower minima for the spontaneous polarization [25], and in part due to the contribution of nano-polar regions (PNR) formed by the more or less statistical disorder of Mg^{2+} and Nb^{5+} ions centering the oxygen octahedra [26]. In 2011, a very large transverse piezoelectric coefficient was also observed at epitaxial PMN-PT thin films integrated onto silicon cantilevers [34].

Nowadays, in thin film form, ferroelectrics are finding a wide spectrum of applications in non-volatile memories and radio frequency (RF) microwave devices. Components based on ferroelectric thin films are also being investigated for various sensor and actuator applications and for many other systems [35], [36].

2.2   PMN-PT and relaxor ferroelectrics

2.2.1   Ferroelectric materials and domains

Ferroelectricity is related to crystal symmetry. The characteristic properties of ferroelectric materials is firstly a non-zero spontaneous electric polarization, and secondly that the latter is switchable by an

external electric field [37]. The first condition means that the material is polar, i.e. it contains no symmetry element that would invert the polar axis, particularly no inversion center. This allows for the existence of a permanent electrical dipole moment. All these materials show a pyroelectric effect and are also piezoelectric for which the absence of an inversion center is a sufficient condition. The switching of polarization by an external electric field requires a displacement of ions, or groups of ions like the oxygen octahedra in perovskites. The crystalline structure must be such that there is not too much an obstruction when doing this displacement. Thus, all ferroelectric materials are both py-roelectric and piezoelectric. The relationship between ferro, pyro and piezoelectric materials is sche-matically shown in figure 2.1. For instance, PMN-PT possesses spontaneous polarization and is ferro-, pyro- and piezoelectric simultaneously.
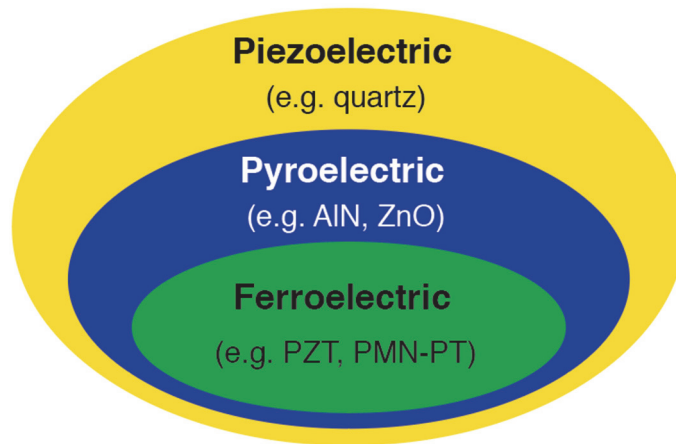
Figure 2.1 - The relationship between piezo-, pyro- and ferroelectric materials, with some representa-tive materials presented for each class.

Most ferroelectric materials exhibit a structural phase transition from a high-temperature non-ferro-lectric phase into a low-temperature ferroelectric phase, necessarily requiring a lowering of crystal-line symmetry. In perovskites, the high-symmetry phase is usually cubic, and the lower symmetry in the ferroelectric phase may form a tetragonal (one 4-fold axis remains) or rhombohedral (one three-fold axis remains) structure. Figure 2.2 gives as example the perovskite structure $PbTiO_3$. The critical temperature of the phase transition is called the Curie temperature, T_C. As the ferroelectric material

is cooled through the structural phase transition, the onset of the spontaneous polarization at T_C leads to the formation of surface charges. The depolarizing field, as produced by surface charges, exhibits an orientation opposite to the spontaneous polarization. In order to minimize the electrostatic energy, a ferroelectric crystal may split into various regions with uniform spontaneous polarization orientation. These regions are called ferroelectric domains, and the region between two distinctive domains is called domain wall. In case of mechanical stress on a ferroelectric material, multi-domain state can also exist to minimize the elastic energy (due to spontaneous strain) [38]. In the *tetragonal* cell, the spontaneous polarization has the same chance to arise along six directions (including positive and negative directions along the three possible a_c axes). The developed polarization direction will rely on the electrical and mechanical boundary conditions applied on the ferroelectric crystal. The regions with uniform direction of polarization are called domains (fig 2.3). In absence of constraints and electrical fields, all 6 domain types will be realized and the macroscopic polarization of the crystal can be zero. In order to reach a maximal macroscopic polarization, the ferroelectric material must be poled, i.e. a relatively large electric field (larger than the coercive field) is applied, often at higher temperature (as e.g. 150 °C) in order to allow as well for the migration of charged defects.
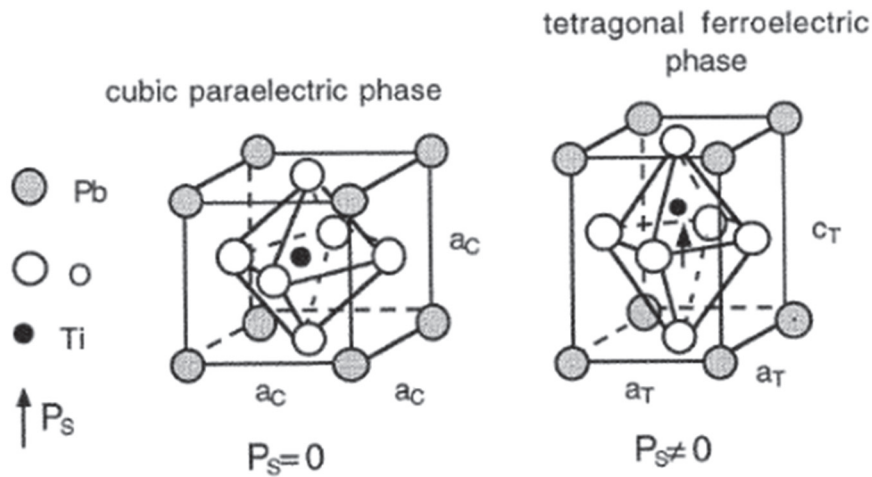
Figure 2.2 - The perovskite structure ABO_3 with atom locations, shown here for $PbTiO_3$, which has a cubic structure in the paraelectric phase and tetragonal structure in the ferroelectric phase. Image taken from Ref. [38].
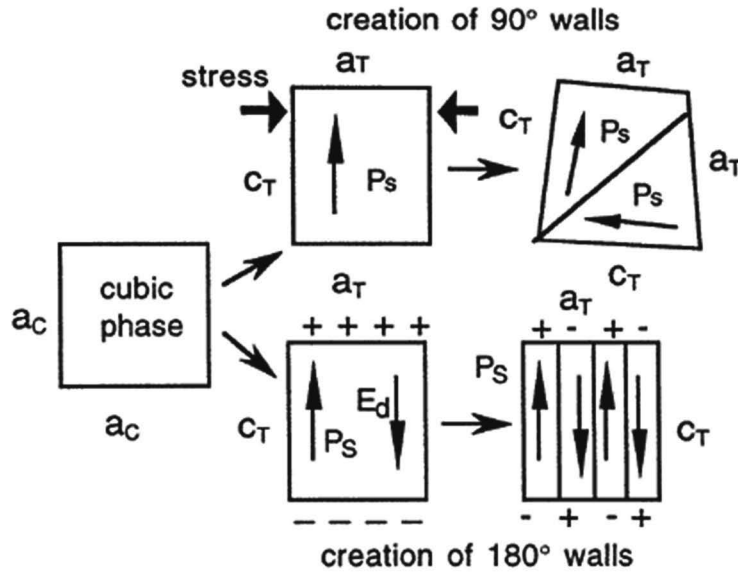
Figure 2.3 - Schematic formation of 90° and 180° (where the separated domains have perpendicular and opposite polarizations) ferroelectric domain walls in a tetragonal perovskite ferroelectric, such as PMN-PT. Image taken from Ref. [38].

2.2.2   PMN-PT

Lead magnesium niobate - Lead titanate (PMN-PT) studied in this thesis is a solid solution of the disordered, relaxor type lead magnesium niobate (PMN) and the ordered ferroelectric lead titanate (PT). The Lead magnesium niobate ($Pb(Mg_{1/3}Nb_{2/3})O_3$), or PMN, is a classical relaxor with a macroscopic pseudocubic structure at room temperature. It shows appealing functional properties such as a very large dielectric constants, huge electrostrictive coefficients and an ultrahigh electrocaloric effect [39].

When mixing PMN with PT to form a solid solution $PMN(1-x)PT(x)$, a longer-range order becomes dominating, leading to a spontaneous polarization and thus to ferroelectricity. For $x = 0.1$ to 0.33 the symmetry is rhombohedral, and from about 0.35 to 1.0, the symmetry is tetragonal. Close to this morphotropic phase transition, a monoclinic phase was observed. Single crystals of PMN-PT are known for their giant piezoelectric properties. They are on one hand due to the compositional choice

of $x = 0.32$ at a morphotropic phase boundary on the rhombohedral side (P//<111}>) with its shallower minima for the spontaneous polarization [19], [25]. Polarization rotation toward [001] easily destabilizes the rhombohedral ground state, resulting in a phase transition to the tetragonal structure. When the tetragonal phase is driven by an electric field from the rhombohedral ground state, additional room for further strain is provided, increasing the maximum strain level. With the recent progress on understanding the origins of high piezoelectric response in MPB systems, the experimental results and ensuing findings of first principle proves that a monoclinic (*M*) phase forms in MPB region. This narrow monoclinic phase serves as 'structural bridge' between rhombohedral (*R*) and tetragonal (*T*) phases [40]. In PMN-PT, monoclinic phase exists in the PT composition range of around 0.3 - 0.36 prior to the tetragonal phase [41], as shown in the PMN-PT phase diagram of Figure 2.4. Polarization in monoclinic structures lies within a mirror plane, allowing easy rotation of polarization, which has a direct impact on large electromechanical properties [40].
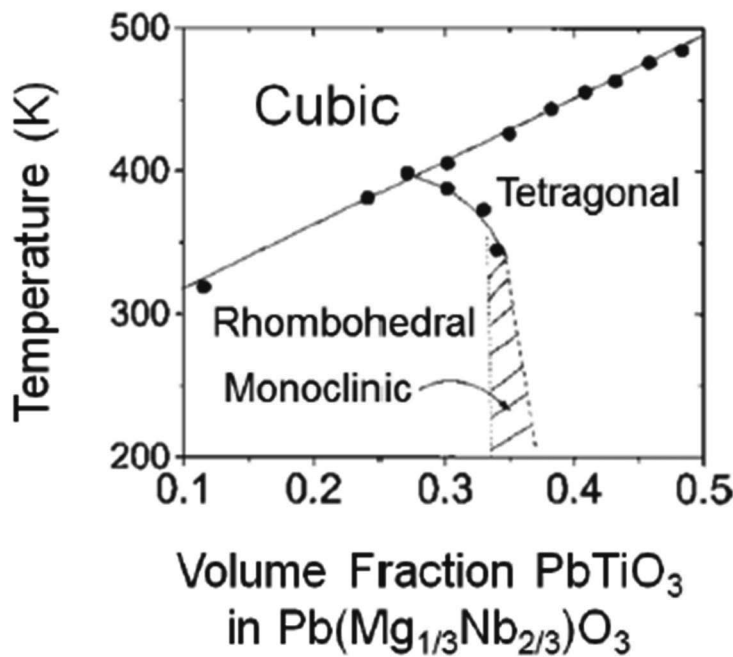
Figure 2.4 - $(1-x)$Pb(Mg$_{1/3}$Nb$_{2/3}$)O$_3$-xPbTiO$_3$ phase diagram. From Ref. [15]

14

Ferroelectric compositions near an MPB provide considerably superior functional properties. One of the well-known example is PZT system where $Pb(Zr_{0.52}Ti_{0.48})O_3$ (or PZT 52/48) is utilized for enhanced piezoelectric properties. The measured piezoelectric coefficient d_{33} as a function of $PbTiO_3$ composition fraction in PZT and PMN-PT systems is present in Figure 2-5. For PMN-PT system, the d_{33} shows two local peaks near the MPB region arising from the $R \rightarrow M$ and $M \rightarrow T$ phase transitions. Notice that the second transition of $M \rightarrow T$ yields a lower d_{33} maxima [42].
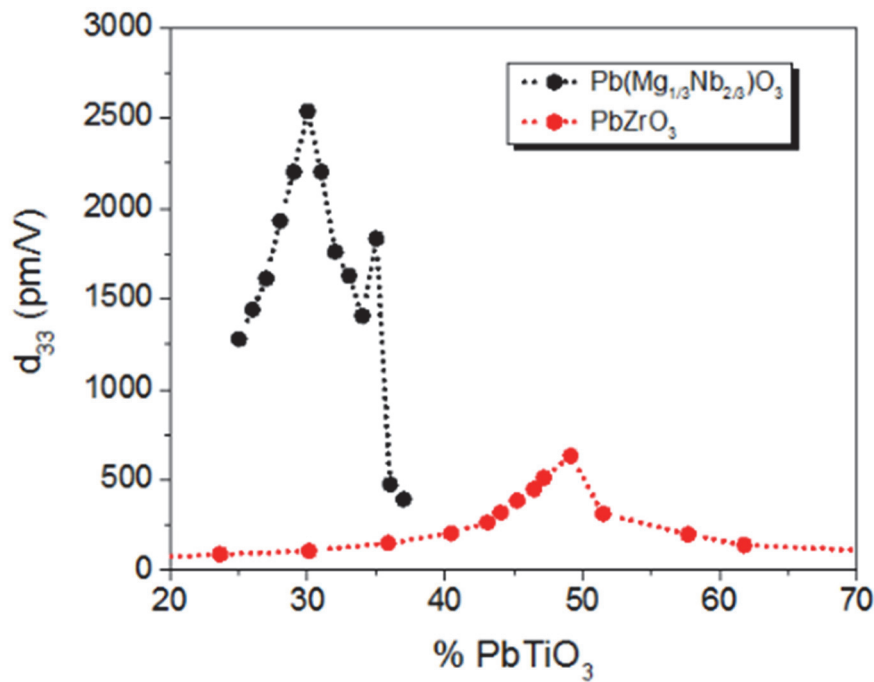
Figure 2.5 - Piezoelectric coefficient d_{33} as a function of $PbTiO_3$ composition fraction in PZT and PMN-PT systems. From Ref. [15]

Another reason for enhanced piezoelectricity is due to the contribution of polar nanoregions (PNRs), a feature formed in the relaxor PMN. In normal perovskite solutions, such as in PZT systems, the B sites are taken by Zr^{4+} and Ti^{4+} ions, which have the same valence states. However, Mg^{2+} and Nb^{5+} ions centering the oxygen ocatahedra in PMN are characteristically non-isovalent, and thus lead a certain charge disorder. These PNRs are of nanometers in size and are developed upon cooling through the Burns temperature, T_B, which is ~347°C for pure PMN [43]. The relatively large difference in valence of B site cations results local charge fluctuations. The large polarizability of the PMN

lattice is ascribed to growing and shrinking of PNRs, contributing essentially to the anomalously high dielectric permittivity and electrostrictive response [44]. Relaxors typically exhibit a frequency-dependent dielectric permittivity with a broad maximum [45].

2.3   Nucleation and growth of epitaxial thin films

The term epitaxy is derived from two Greek words epi (placed or resting upon) and taxis (an ordered manner). In many thin film growth processes, it is desired that the deposited material forms a mono-crystalline film with defined orientation with respect to substrate topmost crystalline layer.

Depending on the substrate template material and the deposited film, epitaxy can be divided into homoepitaxy and heteroepitaxy. In homoepitaxy, film and template layer are of the same material. Homoepitaxy is widely used in semiconductor industry, particularly to grow a silicon thin film on top of a single crystal silicon wafer. In contrast, heteroepitaxy refers to the situation where the deposited film is a different material from the template layer. In this work, we work on PMN-PT and/or $SrRuO_3$ depositions on $SrTiO_3$ single crystal substrate, which are of heteroepitaxial growth. Heteroepitaxial growth is very much applied in III/V technology for photonic and opto-electronic devices.
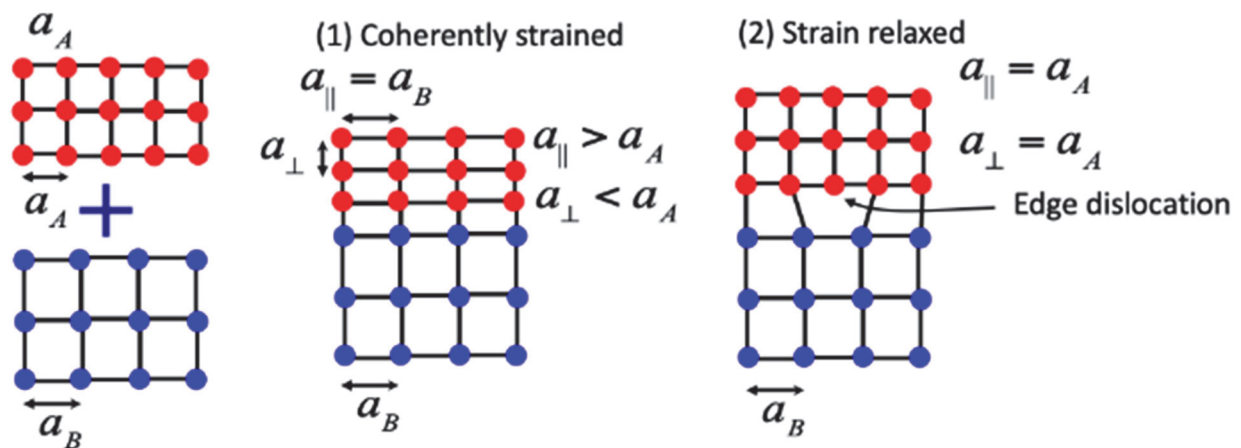
Figure 2.6 - Schematic view of the two extreme cases of heteroepitaxy structure (1) coherently strained to (2) fully relaxed.

In homoepitaxy, there is a perfect lattice match between the film and substrate, i.e there is no misfit strain at the interface (provided that the process does not create defects). As for heteroepitaxy, the lattice parameters between the heterojunction constituent materials are not the same and the differences in the lattice constants is referred to as lattice mismatch. The mismatch with respect to the substrate is thus defined as in equation 2.1,

$$f = \frac{a_f - a_s}{a_f} \tag{2.1}$$

where a_f and a_s are the unstrained lattice constants of film and substrate. This mismatch must be accommodated by (i) tensile/compressive strain, (ii) formation of structural defects (edge dislocation), or (iii) a combination of both [46], [47]. As the mismatch gets larger, the film material may get strained to accommodate the lattice structure of the substrate. This happens during the early stages of film formation (pseudomorphic growth) and between materials of the same lattice structure. In case that strain accommodation is not possible, then dislocation defects at the interface may form leading to fully relaxed epitaxy and the film returns to its original lattice structure above the interface. A schematic view of the two extremes of coherently strained and fully relaxed films is presented in Figure 2.6. Note that the difference in thermal expansion coefficients and film-substrate chemistry have significant influence on the interface as well.
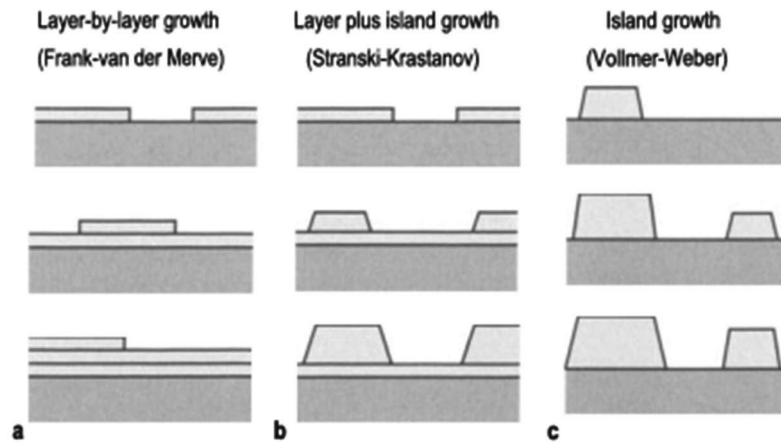
Figure 2.7 - Schematic view of the three main growth modes: (a) layer-by-layer (Frank-van der Merve, FM) growth mode; (b) layer-plus-island (Stranski-Krastanov, SK) growth mode; (e) Island (Vollmer-Weber, VW) growth mode. From Ref [48].

Crystalline thin films deposited on a substrate with a growth process must first nucleate the crystalline phase, if it is not yet as phase of the substrate [49]. At the initial stage of growth, adatoms play an important role. These are atoms (or molecules such as PbO) that have arrived from the vapor, but are not yet strongly bound to the solid, and migrate easily. They may combine with one another to form clusters as a result of attraction. After reaching a certain critical size, the clusters become stable. The process of the stable cluster formation is called nucleation, and extremely important in case of heteroepitaxy at higher temperatures where thermodynamic phenomena dominate (capillarity theory). As the growth proceeds, more and more clusters (nuclei) are nucleated. The stable clusters grow, coalesce and form a continuous film on the substrate surface. Three principal modes of film growth, also named after their original investigators, are typically distinguished (Figure 2.7) as follows:

- Layer-by-layer, or Frank-van der Merve (FM) mode. In this mode the film atoms are bound more strongly to the substrate than to each other. Small stable cluster coalesce in two dimensions only to form planar sheets. As a result, the subsequent layer only starts growing after previous layer is fully completed. In other words, two-dimensional growth takes place. This is typically the case in homo-epitaxy, and heteroepitaxy with small lattice mismatch.

- Island, or Vollmer- Weber (VW) mode corresponds to the case where small clusters nucleate in the form of three-dimensional islands on the substrate surface. In this case, film atoms are more strongly bound to each other as compared to the substrate. In terms of the capillarity

theory, the condensate/vapor and condensate/substrate interface energies are too high in comparison the vapor/substrate interface energy.

- The Stranski-Krastanov (SK) mode refers to an intermediate situation between FM and VW modes. The film grows first in a layer-by-layer mode, followed by the growth of three-dimensional islands. Originally explained by a strong adatom-substrate bond, this mode is now often described as a consequence of epitaxial strain (e.g. Ge/Si). After reaching a certain number of layers, the strain energy (compressive only) in the film starts to be released by modulating the height of the following layers, combined with a voidening of the atomic positions in the depressions where the interatomic distances would shrink. This then leads as well to an island morphology.

2.4 Pulsed laser deposition

2.4.1 Principle of PLD

Pulsed laser deposition (PLD) is a physical vapor deposition technique. The principle of PLD is presented in Figure 2.8. It utilizes short, high power laser pulses to evaporate (ablate) material from a target surface and eject it in the form of a luminous plume, or 'ablation plume'. Atoms, ions, and molecules from the plume condensate on a substrate, where thin film is grown [27], [50], [51].
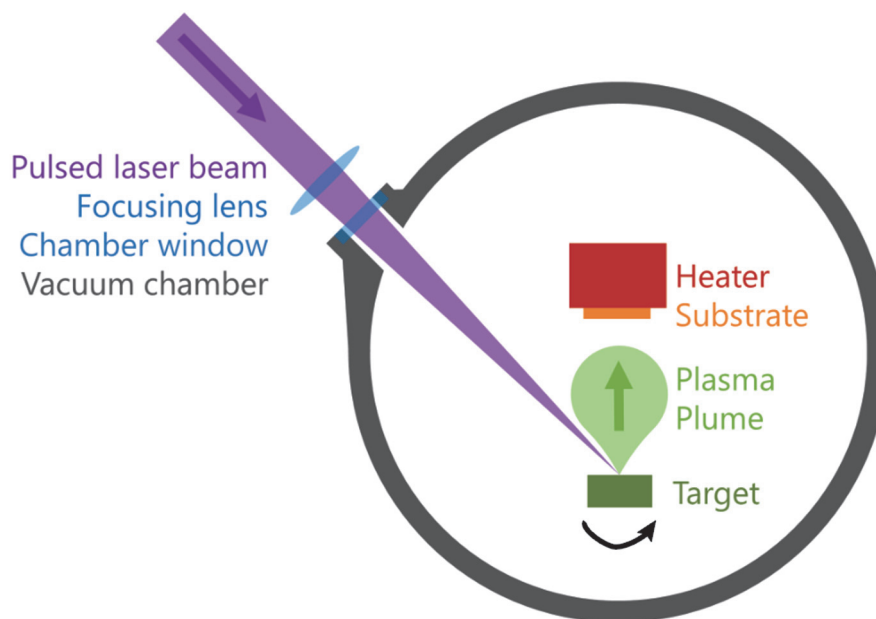
Figure 2.8 - A schematic of the principle of PLD.

2.4.2 PLD system

For this work, a PLD system from "SURFACE systems + technology" (Figure 2.9) was employed for the fabrication of PMN-PT/SrRuO$_3$ heterostructures on SrTiO$_3$ substrates. The deposition system consists of a KrF Excimer laser (Lambda Physics) with a wavelength of 248nm. The maximum energy per pulse and repetition rate of the laser from the source can be tuned. Typical values are 400 mJ for the pulse energy and 2 – 3 Hz for the repetition rate (maximal 5 Hz). The laser then passes through rectangular slit to cut off the beam border region, and to let pass the central part with uniform energy density. Afterwards, the laser pulses are directed to the chamber with two mirrors (in our case), pass a focusing lens, and enter into the chamber. Inside the high vacuum chamber, the beam hits a rotating target. The substrate is facing the target in a distance of some cm's. The substrate is heated from the backside with an IR laser diode to a given deposition temperature. The threshold power density needed for ablation (plume formation) depends on the target material, the morphology and laser pulse diameter, energy, and wavelength. After laser radiation is absorbed, the electromagnetic energy of the laser pulses is immediately converted into electronic excitation and bond breaking, and afterwards into thermal, mechanical and chemical energy which result into formation of supersonic jet of plume. The ablation plume may contain not only atoms, molecules, electrons, ions, stable clusters, but also micro-sized solid particles and molten globules. The physics behind the processes of

PLD is rather complex and interrelated, and strongly related to the properties of target materials and laser pulse characteristics. These are explained in depth in some review literatures [27], [50].
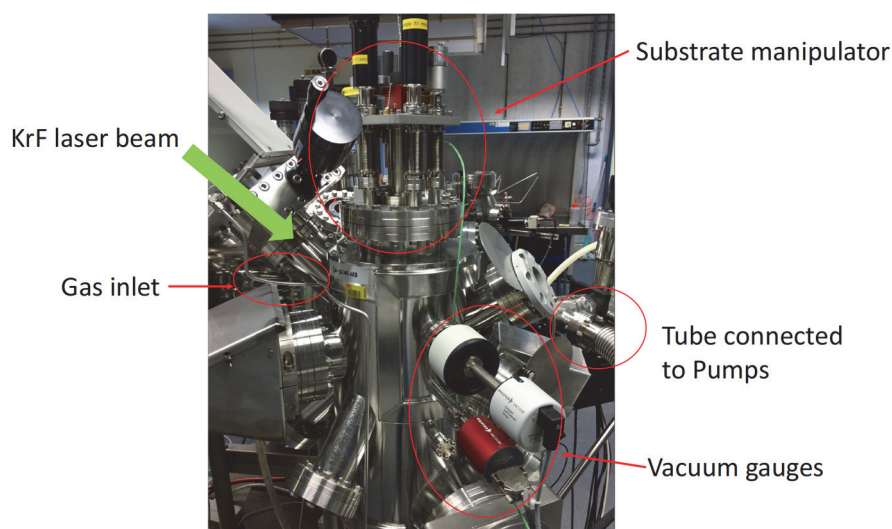
Figure 2.9 - A photo of the deposition chamber of employed PLD system.

2.4.3   General features of PLD

There are many advantages of the PLD technique making it attractive [27][50], such as: (i) wide selection of target materials as almost all condensed materials can be ablated; (ii) high flexibility in terms of target materials use and geometrical arrangements in the setup since the energy source is outside the deposition chamber; (iii) high flexibility to control growth rates over big range due to pulsed nature of the laser beam; (iv) after the deposition conditions are optimized, the stochiometric transfer of the elemental components from the bulk to the film can be preserved, even for chemically complex systems; (v) the target material is only ablated in the region to which the laser beam is focused; (vi) the kinetic energy of the atomic and ionic species is smaller than 1 eV, which is not enough to damage the growing film. It is clear that high energy atoms and ions have much less energy than in the case of sputter deposition, where negative oxygen ions may reach several 100 eV of kinetic energy.

On the other hand, PLD also has technical and fundamental disadvantages, for instance (i) impurities in the target material; (ii) ablated plume flux is inhomogeneous and has an angular energy distributions; (iii) particle formation during the ablation process, risking to ruin the film; (iv) high maintenance effort due to coatings on the UV glass window for the laser beam, and recharging of the laser with the Kr-F gas mixture.

2.5   SrTiO$_3$ substrate preparation

The usage of atomically flat single terminated oxide substrates is one of the critical requirements for high quality epitaxial film deposition [52]–[55]. The growth of overlying film and the achieved structure and properties are determined by the atomic arrangements and the chemical reactions of the top surface of substrate layer. After proper surface treatment procedures, the surface should have the desired structural flatness and chemical termination. The former one is revealed by AFM, as shown by the example given in Fig. 2.10: The surface of as received ABO$_3$ substrate (001) surface is not atomically flat (Figure 2.10 b), while after the treatment, the sample surface presents a step-terraces profile (Figure 2.10 d) and the step height is identical to the out-of-plane lattice constant c. The atomic structures models of as-received and treated ABO$_3$ samples are illustrated in Figure 2.10 a and 2.10 c respectively. After treatment of the ABO$_3$ (001) substrates, the surface layer would be either AO or BO$_2$ terminated [53]. In case of Sr^{2+}Ti^{4+}O$_3$, both planes are neutral, which facilitates atomic flatness (in contrast to LaAlO$_3$, where both planes are charged).
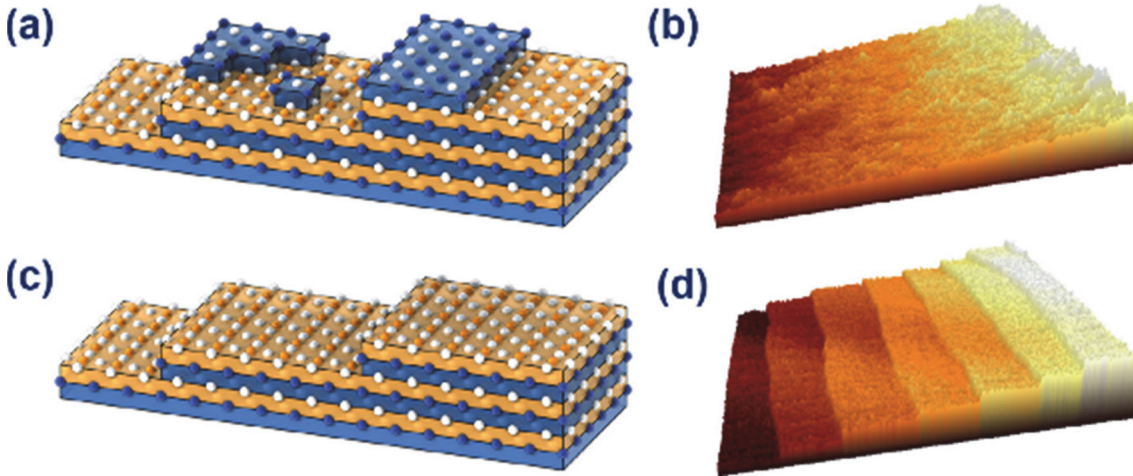
Figure 2.10 - Modeled ABO_3 (001) atomic structure and corresponding AFM topography image of: (a)-(b) an as-received surface and (c)-(d) an atomically flat single surface. From Ref [53].

Strontium titanate ($SrTiO_3$) single crystals are by far the most widely used substrates in complex-oxide research. The as-received polished SrTiO3 samples exhibit (100)-oriented surfaces with both SrO and TiO_2 terminated regions. SrO makes up around 25% of the area. For epitaxial depositions of PMN-PT and $SrRuO_3$, TiO_2 terminated surfaces are required. Atomically flat single terminated surfaces are typically achieved by employing an acid based etching and thermal-annealing process. For example, the method based on buffered-hydrofluoric acid (BHF) etching, which is the same chemical etching procedure used in silicon semiconductor research and industry for removing SiO_2, resulted in atomically flat $SrTiO_3$ substrates. The technique is based on the recipe firstly published by Kawasaki et al [52] that was developed to remove any SrO termination.

2.6   Electron microscopy

Electron microscopy techniques exploit high energy electron beams, exhibiting much shorter wavelengths than visible light, and is able to image small size structures with much higher resolution than optical microscopes [56], [57]. Electron microscopy is divided into two types of techniques, namely Scanning Electron Microscopy (SEM) and Transmission electron microscopy (TEM).
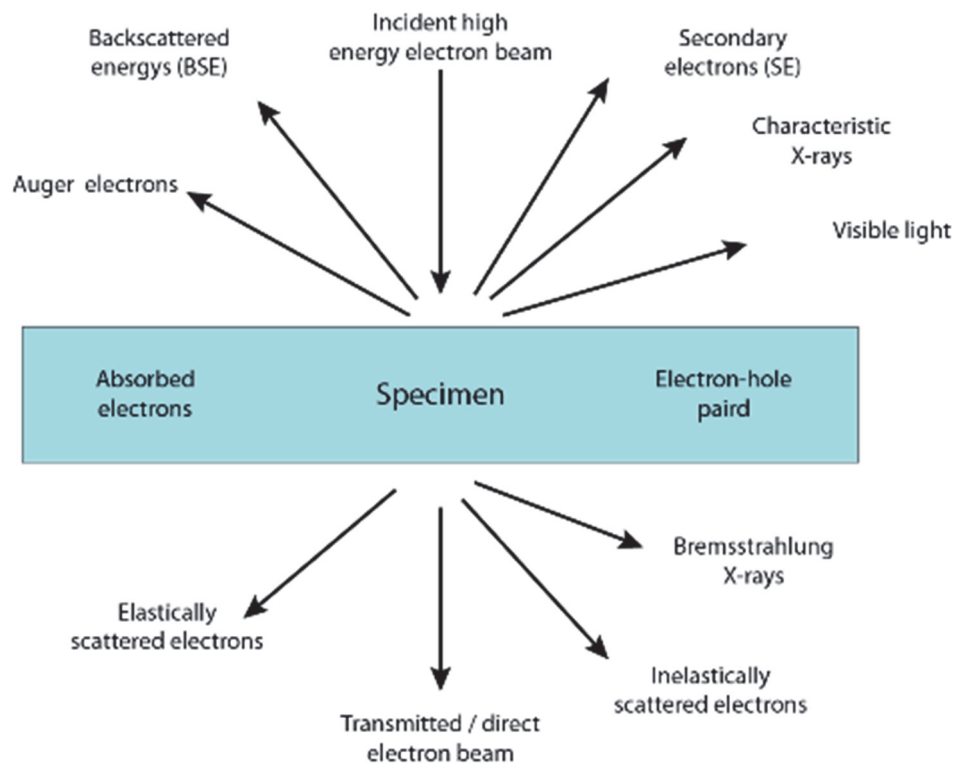
Figure 2.11 - Generated electrons and photons in forward and backward direction when a high-energy beam of electrons interacts with a thin specimen. From Ref. [58].

When the sample interacts with a high energy electron beam in high vacuum, a number of signals can be captured. The SEM collects secondary electrons of a few eV emitted from the atoms when hit by high energy electrons. The detector might also be reached by backscattered primary electrons resulting from mainly inelastic scattering. The SEM is a fast, flexible and non-destructive approach used to study surface morphology, film thickness (by examining a cross section), and also the morphology of a film cross-section. The chemical composition can be measured by Energy Dispersive Spectroscopy (EDS) of the ejected X-ray photons generated by a collision of (mainly) primary electrons with the atoms of the specimen. These photons have very characteristic energies for each atom, corresponding to the energy difference of electron states on the atom.

A thin specimen called TEM lamella is prepared by focused ion beam (FIB) milling prior TEM observations. The lamella region is first positioned precisely to the object of interest by means of the

SEM imaging capability of the FIB tool. The region of the cut is covered by a protecting material (carbon and/or platinum), the lamella is finally separated from the sample by milling holes on both sides of the lamella. The lamella is then lifted out by a manipulator, and eventually thinned further afterwards.
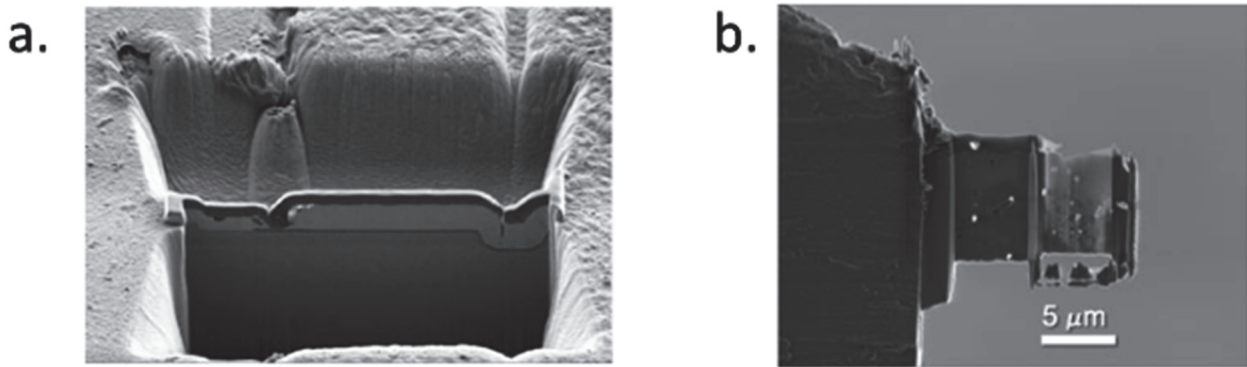
Figure 2.12 - TEM lamella preparation. (a). FIB milling from a sample. Lamella region covered by a protecting material. (b). Lamella after thinning. Adapted from Ref. [58].

The lamella is irradiated with electron beam at energy ranging from 100-300 keV, and the transmitted electrons are studied (fig. 2.11). Different TEM imaging modes are available: bright field, dark field or high-resolution transmission microscopy (HRTEM), depending on the selection of objective aperture. In bright field imaging mode, the aperture selects unscattered and non-diffracted, thus directly transmitted electrons and blocks the other ones. The most valuable feature for the investigation of crystals is the possibility to observe diffracted electrons. This allows to analyze the crystalline phases present in the sample, and their orientation with respect to the beam and sample, as for instance the texture of a polycrystalline film. In the dark field mode, the imaging is made with diffracted electrons of a defined crystalline plane meeting Bragg's law. This technique highlights regions with identical orientation of the same crystalline phase. In the bright field mode, crystalline regions appear somewhat darker as the direct beam lost diffracted electrons. Amorphous regions will appear in consequence more brightly. In HRTEM, an interference pattern is formed by the interference of several diffracted beams both with each other and the transmitted beam, which is selected by a large objective aperture. Overall, TEM can be used to study the crystal lattice, lattice defects, dislocations, domain patterns, interfacial defects as well as film thickness.

In either SEM and TEM, an electron beam is focused on the sample and generates characteristic X-rays, which correspond to the energy differences of deeper lying electronic states of the present atoms. As these transition energies are very specific for a given atom, the X-rays can thus be used to analyze the chemical composition of the sample, usually applying a technique called Energy Dispersive Spectroscopy. The spectrum giving the photon counts of the detector against their energy allows the elements to be identified, while the corresponding peak intensities allow the concentrations of the elements to be quantified. For PMN-PT thin film composition analysis, care must be taken to select suitable peaks not overlapping with others. Since certain elements (e.g. Pb, Nb) have quite close characteristics, their x-rays peaks from the M-shell are difficult to separate. A high energy level (~18 keV) is needed to excite the *L*-shell characteristic x-rays to distinguish elements. This approach works well for TEM-EDS, but not so well for SEM-EDS. The reason is that high energy electrons penetrate deeper into the $SrTiO_3$ substrate, and consequently a large part of the signal of Sr and Ti is from the substrate and not from the PMN-PT film or SRO film.

2.7   X-ray diffractions

X-ray diffraction (XRD) is a non-destructive analytical technique for the characterization of the crystalline structure. The versatile technique is widely used to study structural properties of crystals, such as lattice parameters, strain level, grain size, epitaxial mismatch, preferred orientation, percentage of phase composition, and thermal expansion [59]–[61], etc. The structural investigations described in this thesis are performed on Bruker D8 Discover XRD. The X-rays are generated from Cu- Kα emission source and have a wavelength of 1.54056 Å.

The XRD technique is based on interference of the scattered X-rays from the atomic planes. Constructive interference at equidistant, parallel planes produce diffraction peaks at the condition described by Bragg's law:

$$n\lambda = 2d \sin \theta \tag{2.2}$$

where d is plane spacing, λ is the x-ray wavelength, θ is the incident angle and n is an integer defining the order of diffraction.

The diffracted X-ray intensity is typically recorded as a function of 2θ values, which is the angle between diffracted X-ray beam and the incident beam. This is also usually called θ-2θ scans. These

out-of-plane measurements offer much information, such as out-of-plane lattice constants (d-spacing), phases purity, strain (shifting of peak positions) and out-of-plane crystallographic orientation.

Reciprocal Space Maps (RSMs) are mapping a two-dimensional region of the reciprocal space [62]. These maps around reciprocal lattice spots provide additional information beyond that obtained from single line scans such as high-resolution rocking curves. RSMs are typically used to aid the interpretation of peak displacement, peak broadening or peak overlap. The procedure of RSM is carried out by performing an Omega scan for a given length of the scattering angle and then employing a 2theta-Omega mode to change the length of the scattering vector by small amount and repeating the process. Both in-plane and out-of-plane lattice parameters can be extracted from RSM results and thus strain between thin film layers is then deduced. Overall, RSM provides detailed information about the film growth, domain structure, film orientations, rotations, tilting and defects.

2.8 Electron beam lithography

Electron beam lithography (abbreviated as e-beam lithography or EBL) is a lithography technique by using a focused electron beam to directly write nano patterns on resists [63]. The process allows patterning of very small dimensional features, usually in submicrometric size down to a few nanometers. A thin layer of EBL resist is exposed by scanning a precisely controlled electron beam.

Figure 2.13 - Vistec EBPG 5000+ ES electron beam lithography system at center of micro nano technology (CMi), EPFL.

After development, the patterns will appear. Like photo lithography, depending on positive or negative tone of the resist, the desired pattern can be either the same as the area of exposed resist or opposite to it. The exposed structure is used either to create a mask for etching, or for template thin-film deposition (masking the deposition). Because of the much shorter wavelength of accelerated electrons (e.g., 0.005 nm at 50 keV) compared to that of ultraviolet (UV) light used in traditional photolithography, EBL has the obvious advantage that it is not limited by diffraction as the photo lithography. In fact, the resolution is limited by the phenomena depicted in Fig. 2.11: electron backscattering and other secondary electron and X-ray emission. On the other hand, EBL is hampered by slow speed, low throughput due to direct writing of patterns. Nevertheless, EBL is widely used for preparing direct writing of small-area, low-volume nano-size features for research purposes, and mask fabrication for optical lithography.

The EBL tool employed for this thesis is the one of the center for micro and nanotechnology at EPFL, shown in Figure 2.13, a model Vistec EBPG 5000+ ES. The system features a 100keV thermal field emission gun, Gaussian beam geometry, and a 50MHz pattern generator.
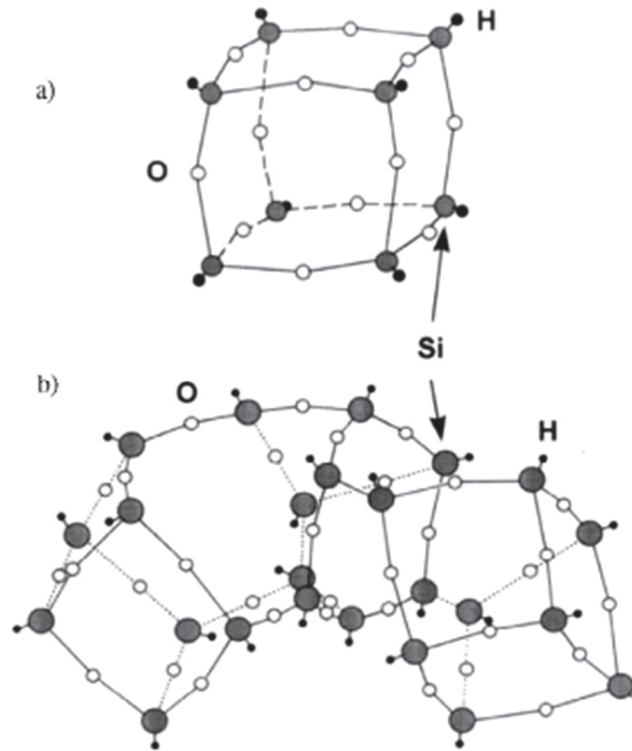
Figure 2.14 - Schematic view of the molecular structure of HSQ: (a) cage structure (b) random-size structure of the resist solution. From Ref [64].

The ultimately desired PMN-PT nanostructure for PET device has a feature size about 20 nm. EBL process to achieve patterns in sub-20 nm range is inevitable sensitive to a lot of factors, starting from the choice of resist material, together with resist exposure and development process, and the density of heavy ions in the substrate. Although, very fine features (as small as 3 nm) have been obtained with standard EBL resist PMMA [65] on silicon substrate, the difficulties of low etching resistance and instability of this polymer resist are encountered. Hydrogen silsesquioxane (HSQ), as a relatively new EBL resist, shows clear advantages in the sub-20 nm range applications [64], [66]. HSQ is an attractive negative-tone electron resist that allows direct writing of etch-resistant silicon oxide nanostructures with low line-edge roughness. The cage-like structure of HSQ is shown in Figure 2.13 (a). Various number of the cages could bound together in HSQ solution (see Figure 2.13 (b).). Without

exposure, the resist solution has the general formula $(HSiO_{3/2})_{2n}$. During exposure to a high-energetic electron beam, Si-H groups of HSQ are cracked, inducing crosslinking and leading to an amorphous microstructure similar to glassy SiO_2. In this state, it is relatively insoluble in alkaline hydroxide developers, which attack well the Si-H groups of the undeveloped resist.

2.9   Piezoresponse force microscopy

First introduced in 1992, piezoresponse force microscopy (PFM) was used to investigate local coupling between an electrically biased probe and a consequent mechanical sample deformation in a ferroelectric polymer film by Günther and Dransfeld [67]. It has become a key instrument to advance understanding and to optimize ferroelectric materials over the last 2 decades. PFM is the instrument that detects the local piezoelectric deformation by applying an electric field to a sample. Due to the capabilities of measuring deformations in the picometre scale and mapping ferroelectric domain patterns with a lateral resolution of several nanometres, PFM has become the main technique for exploring ferroelectric domain patterns [68]. Moreover, PFM has the merits of versatility, convenience of handling, non-invasive characteristic and the need of relatively simple sample preparation procedure.

In PFM, a conductive AFM tip is contacted with the surface of a sample, and an additional oscillating voltage is applied to the tip,

$$V_{\text{tip}} = V_{\text{dc}} + V_{\text{ac}} \cdot \cos(\omega t) \qquad (2.3)$$

where ω is the modulation frequency, V_{dc} is an optional dc offset and V_{ac} is the "small" signal excitation provoking an ac deformation at the surface of a piezoelectric material. The resulting vibration of the sample surface will be detected by the motion of the AFM cantilever or probe. This motion is monitored by the oscillating reflection spot of a reflected laser beam produced on a photo diode array and then demodulated via a lock-in amplifier. In this way, topography (low frequency response) and piezoelectric response (ac) can be imaged at the same time. The outstanding contribution of this technique is to visualize ferroelectric domains on the nano scale, particularly at thin films. The schematic view of PFM working principle is shown in Figure 2.15.
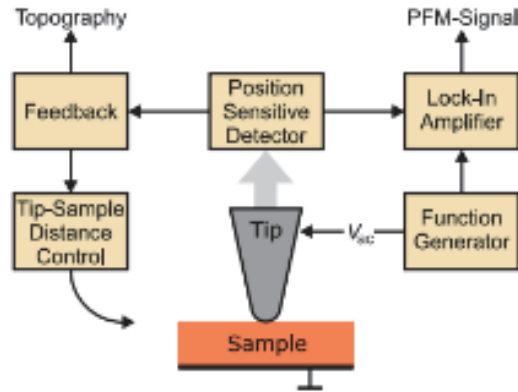
Figure 2.15 - A schematic view for piezoelectric force microscopy setup [68].

Driving the tip at the resonance frequency of the AFM probe has the benefit of amplifying the response by the factor of 10 to 100. However, due to the fact that the resonance frequency strongly depends on the local environment of tip-sample interactive region, the orientation of polarization and the topography features, the resonance encounters a frequency drift and thus maintaining frequency is not straightforward. To mitigate this problem, Asylum Research Corporation developed the Dual AC Resonance Tracking (DART) method [69]. Except for tracking the resonant frequency, this technique enables the additional model parameters such as the tip-sample dissipation to be measured [70]. The principle behind DART is illustrated schematically in Figure 2.16. Rather than driving the tip with the peak resonance frequency, two frequencies with a fixed distance—one slightly above and the other slightly below the highest frequency, are employed. The resulting cantilever movement is digitized and separately sent to two lock-in amplifiers (Figure 2.16 (a)), which allows to calculate the corresponding amplitudes and phases. When there is a change in the contact stiffness, a frequency shift is also expected, as referring to Figure 2.16 (b). The corresponding amplitudes also changed (saying $A_1 \rightarrow A'_1$, $A_2 \rightarrow A'_2$) and then difference is sent to the system as feedback signal to maintain the two drive frequencies bracketing the resonance frequency. The technique measures a valid vibration amplitude as a good measure of the surface amplitude on the sample. In this way, the measurement can be done at considerable speed with enhanced signal. The DART overcomes the limitations of strongly position dependent phase response. The PFM amplitude signal in DART mode remains free of topographic effects.
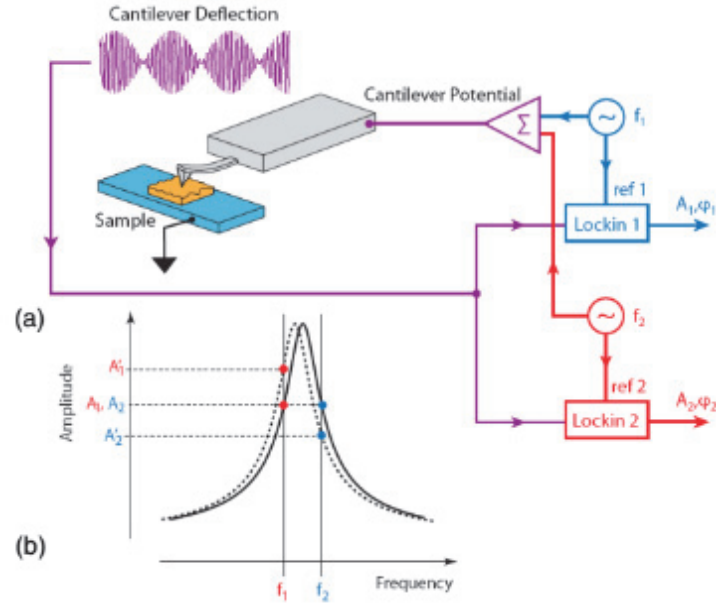
Figure 2.16 - (a) Schematic view for PFM DART mode working principle. (b) The dual-frequency excitation based resonant-amplitude tracking. From Ref. [69].

In this thesis, we mostly use the technique Dual AC Resonance Tracking (DART) [69] to investigate the domain patterns. A superimposed DC field was used to locally pole and to measure the ferroelectric hysteresis.

The technique is available on Cypher PFM from Asylum research, as shown in Figure 2.17.
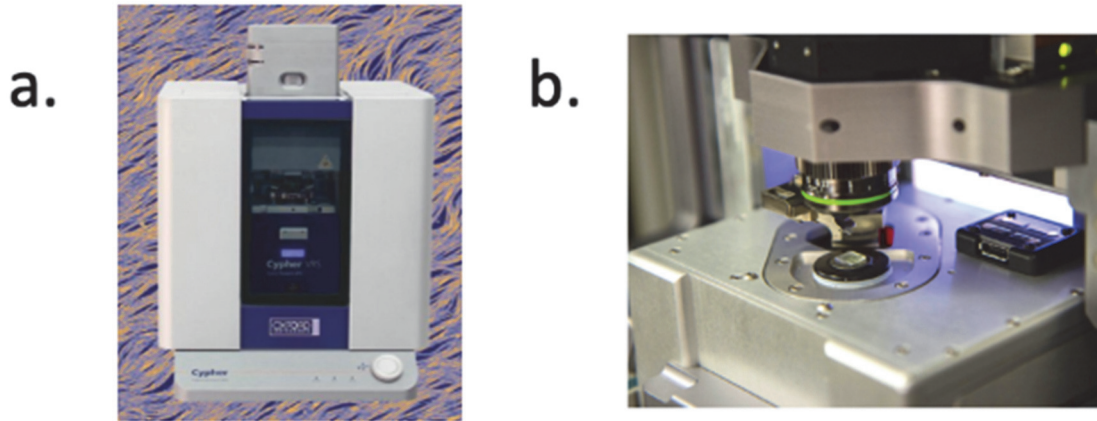
Figure 2.17 - (a) Cypher PFM from Asylum Research. (b). A photo of the PFM stage with a sample loaded.

Chapter 3   Deposition of PMN-PT, SrRuO$_3$ and LaNiO$_3$

The growth process of the material of interest, i.e. lead magnesium niobate – lead titanate (PMN-PT) thin films by a pulsed laser deposition (PLD) technique was optimized. Epitaxial PMN-PT/SrRuO$_3$ films were grown on SrTiO$_3$(001) single crystals. This includes preparing atomically flat substrates with step-terrace profile, optimizing the deposition conditions (temperature, laser energy and repetition rate, target-substrate distance, bottom electrode, O$_2$ pressure, etc.). Highly (100)-oriented, phase pure, crystalline PMN-PT films with a composition near the morphotropic phase boundary (MPB) were successfully grown. The films exhibit an extremely low surface roughness, which is beneficial for piezo-response force microscopy (PFM) studies.

Alternatively, PMN-PT film was planned to be deposited by sputtering. In the first step, we have deposited high quality metallic oxide LaNiO$_3$ (LNO) electrode by sputtering on 4-inch (100) silicon wafer. The deposition of PMN-PT was abandoned due to a long-time breakdown of the sputtering tool. To test nevertheless the LNO thin film as seeding layer for PZT, we applied a sol-gel route for Pb(Zr$_{0.52}$Ti$_{0.48}$)O$_3$ (PZT) growth. The results confirmed that the LNO texture was passed to PZT film.

3.1   Introduction

Over the past three decades, the development of microelectromechanical systems (MEMS) has been advanced and is now widely used in a range of devices and applications, e.g. inkjet printers, accelerometers, RF filters, energy harvesting and ultrasonic transducers etc. It is also foreseen that MEMS and sensors will be essential components for the ongoing Internet of Things (IoT) technology. As the field of MEMS advanced, the driving force for the integration functional materials other than silicon-based compounds into micro systems has emerged.

Piezoelectric materials are of great interest for MEMS applications due to their intrinsic electro-mechanical coupling. Piezoelectricity implements a change of polarization under mechanical stress and

vice versa. By shrinking the sizes, piezoelectric micro- nano- devices require much lower working voltages while providing weaker force and higher resonance frequencies. Piezoelectric materials exhibit high energy density and can be scaled favorably with miniaturization. Extensive research work has been done on many piezoelectric materials and has led to industry applications. Among them, PZT and AlN are the most widely used ones. Alternatively, relaxor ferroelectrics like PMN-PT demonstrated dramatically superior piezoelectric response over PZT, and thus has the promising potential for further miniaturization in next generation of MEMS sensors and actuators or novel nano devices, such as PET [10], [13].

As known in many ferroelectric solid solutions of two compounds, large piezoelectric coefficients appear around a compositional phase boundary between rhombohedral and tetragonal phases. For PMN-PT, this morphotropic phase boundary (MPB) is around 33% PT concentration. Since PMN-PT solid solutions contains multicomponent systems of PbO-MgO-Nb$_2$O$_5$-TiO$_2$, exhibiting complex pathways when get crystallized upon cooling from melt or solution, the growth of single crystal and high-quality thin films is the primary challenge [71]. One of the problems is the widely-observed formation of pyrochlore impurities in both the bulk and thin films of the PMN-PT system. The perovskite phase has a relatively poor thermodynamic thermal stability at off-stoichiometric conditions, as compared to prominent, stable pyrochlore phases. Some common pyrochlore phases include cubic Pb$_3$Nb$_4$O$_{13}$, rhombohedral Pb$_2$Nb$_2$O$_2$ and tetragonal Pb$_3$Nb$_2$O$_8$ [72], etc. Such non-piezoelectric phases result in significant degradation of the functional properties of grown films [73], [74]. Furthermore, all the five elements stoichiometry influence the properties of PMN-PT. On one hand, off stoichiometry degrades the film properties. On the other hand, it is also responsible for the formation of impurity phases (pyrochlore phases). The main cause for off- stoichiometry is lead loss because of the high volatility of Pb and PbO when films are deposited at high temperature. Lead loss may not only promote the formation of lead deficient pyrochlore phases, but also lead to higher leakage current. A further problem is the magnesium loss. It is found that a correct concentration ratio of the two B site elements, i.e. [Mg]/[Nb], is essential for growth of perovskite phase pure PMN-PT films [73].

In literature, the breakthrough of deposition high quality epitaxial PMN-PT films have been realized with several different techniques, such as metal-organic chemical vapor deposition, PLD and sputtering [75]–[77]. The first successfully deposited epitaxial PMN-PT (70/ 30) thin films was reported in 1998. The film was grown with pulsed laser deposition (PLD) on LaAlO₃ substrates with carefully controlled process conditions [75].

Therefore, a set of optimal processing conditions must be found to obtain phase-pure perovskite, (001)-oriented PMN-PT thin films. In our work, pulsed laser deposition (PLD) was employed. The PMN-PT thin films were grown on $SrRuO_3$ buffered (001) $SrTiO_3$ (either intrinsic or doped with 0.7 wt.% Nb) substrates. A further development goal was a low surface roughness, which is necessary for PFM studies.

Table 3.1 - In-plane lattice constant *a* or pseudocubic lattice constant *a* of substrate and films.

Layer	**Crystal structure**	**Lattice constant *a* / c (Å)**	**Mismatch with previous layer (%)**	**TCE ($\times 10^{-6}$ K^{-1})**
$SrTiO_3$ substrate	Cubic	3.905	-	11
$SrRuO_3$	orthorhombic	3.93	-0.64%	10.3 [78]
PMN-PT 67/33	Rhombohedral	4.02 [79]	-2.22%	~10
PMN-PT 64/36	Tetragonal	3.99/4.046 [32]	-1.5 % (*a*), -2,9 % (*c*)	~10

The thin films were deposited on (001)-oriented $SrTiO_3$ single crystalline substrates. $SrTiO_3$ has a cubic perovskite unit cell with a lattice parameter of 3.905 Å, which matches well with commonly used perovskite oxide electrodes, such as $LaNiO_3$, $SrRuO_3$, $La_xSr(1-x)CoO_3$, $La_xSr_{(1-x)}MnO_3$, etc [39], [80]. Baek *et al* demonstrated when PMN-PT (67-33) film is integrated directly on silicon, a thin layer of STO film is capable as template for incorporating such oxide films [80]. The buffer layer $SrRuO_3$ we use here is endowed with remarkable features. First, it is a good conductive oxide that can be used as bottom electrode; second, as its lattice constant is falling between $SrTiO_3$ and PMN-PT, the epitaxial growth of PMN-PT is improved [81] due to a lower lattice mismatch, which reduces the dislocation formation. The literature values of the lattice constants are given in Table I.

It is noticed here, the thermal expansion coefficients of STO, SRO and PMN-PT are all close to 1.05×10^{-5} K^{-1}. This small margin is in favour of relatively small thermal strains mismatching when the devices are cooled down from deposition temperature to room temperature.

In this chapter we describe the conditions of the growth of high quality epitaxial PMN-PT thin films on SRO buffered STO substrates by varying the PLD parameters and present a very narrow process window for phase-pure (001)-oriented film growth.

We also planned to deposit PMN-PT film by RF magnetron sputtering. In this case, film can be grown on a large size substrate, i.e. usually 4-inch or 6-inch Si wafer in lab. Pt or Pt-based metal films are often used as electrodes for ferroelectric thin-film devices [17]. However, they have the problems of week adhesion to the Si substrates, deterioration of ferroelectric properties by the interdiffusion from the interposed adhesion layers of Ti, and unsatisfactory performance against fatigue _. In recent years, metallic oxides having been investigated as promising alternatives for solving the above problems because they have a better crystallographic compatibility with the ferroelectric layer as compared to the Pt electrode. Among them, pseudo-cubic perovskite lanthanum nickel oxide, $LaNiO_3$ (LNO), with a lattice parameter of 3.84 Å, is a very good candidate. It exhibits a good metallic conductivity in a wide temperature range, and its composition is relatively simple to control [82], [84]–[92]. The LNO film resistivity at room temperature is typically in the 0.3 to 2 mΩ·cm range. It has been reported that properties of ferroelectric oxides are significantly improved with the use of lattice-matched LNO bottom electrodes [86], [89]–[93].

We first successfully developed high-quality metallic $LaNiO_3$ by a sputtering tool in Center of MicroNanoTechnology (CMi) on silicon wafer. We have another sputtering tool from industry partner in our lab, which was used to develop PZT deposition. After a failure, their tool could not be repaired anymore in due time, and we were not able to continue the process. Instead, we tested the LNO as a seed layer for sol-gel $Pb(Zr_{0.52}Ti_{0.48})O_3$ (PZT) growth. The results confirmed that bottom electrode LNO texture was passed to PZT film.

3.2   Experiments and results of PLD PMN-PT and SRO

All films of PMN-PT and $SrRuO_3$ have been deposited with PLD using a KrF excimer laser operating at 248 nm wavelength, using commercial targets on pre-heated $SrTiO_3$ substrates. The deposition parameters are given in table 3.2. For each sample, the deposition time of $SrRuO_3$ was 20 minutes, yielding 20 nm thick film. PMN-PT films were deposited subsequently at different conditions to avoid any undesired contaminations, without breaking the vacuum of the chamber. After deposition the

films, the samples were cooled down at a rate of 15 °C/min to room temperature under high O_2 pressure. The latter serves to avoid a too high oxygen vacancy concentration. A detailed list of deposition parameters for SRO and PMN-PT are given in Table 3.2.

Table 3.2 - PLD process conditions of SRO and PMN-PT films growth on (001) STO substrates. (values in brackets are the optimized ones)

Parameter	SRO	PMN-PT
Base Vaccum (mbar)	2.0×10^{-8}	2.0×10^{-8}
Oxygen flow (sccm)	8.0	30 and 70 (70)
Oxygen pressure (mbar)	0.15	0.25 and 0.50 (0.50)
Substrate temperature (°C)	625	$550 - 650$ (575)
Laser fluence (J/cm²)	1.0	1.0
Laser pulse rate (Hz)	2	3
Target-substrate distance (mm)	65	60
Deposition rate (nm/min)	1.0	1.2 (at 575°C, 0.50mbar)
Deposition time (min)	20	20 - 90

3.2.1   Substrate preparation

High quality, (001)-oriented strontium titanate (SrTiO$_3$) substrates were purchased from Crystec Gmbh and SHINKOSHA CO., LTD. Besides the intrinsic non-conductive SrTiO$_3$ substrates, 0.7 wt. % niobium doped SrTiO$_3$ substrates with a conductivity roughly 0.30 $\Omega \cdot$cm were used. The STO substrates were pretreated to TiO$_2$ termination using a method which employs etching followed by annealing, as first reported by Kawasaki *et al* [52]. The etchant is buffered HF, comprising a 7:1 volume ratio of 40% NH$_4$F to 49% HF in water. The method was optimized to treat the as-received STO substrates. The influence of etching time, annealing temperature and time on the substrate surface profile were compared. The AFM images of the substrates surface treated under different conditions are shown in Figure 3.1. The results clearly reveal that substrates annealed at 1100 °C favors a more step-like profile. Moreover, annealing at 1100 °C for 3 hours provides much lower roughness than annealing for only 1 hour, as can be seen from the table 3.2. Overall, the substrates etched for 30 sec and annealed at 1100 °C for 3 hours exhibit an atomically flat, step-terrace profile. The step height was found to be about 0.4 nm, close to the unit cell height of STO lattice.
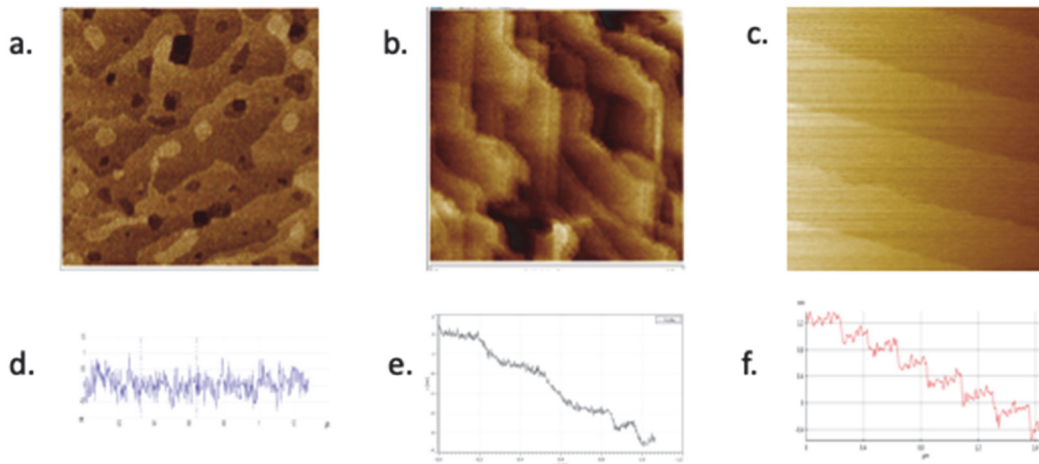
Figure 3.1 - AFM images (1 × 1 μm^2 square) and corresponding to representative line profiles on different SrTiO$_3$ substrate surfaces after treated at different conditions: (a) and (d) BHF etch 15 sec and anneal at 900 °C for 1h; (b) and (e) BHF etch 30 sec and anneal at 1100 °C for 1h; (c) and (f) BHF etch 30 sec and anneal at 1100 °C for 3h;

Table 3.3 - Average roughness of SrTiO₃ substrates treated under different conditions.

	Sample 1	Sample 2	Sample 3
BHF etch time (sec)	15	30	30
Annealing T (°C)	900	1100	1100
Annealing Time (h)	1	1	3
R_a	0.295 nm	0.276 nm	0.094 nm

Furthermore, it was found that the SRO and PMN-PT thin film microstructures did not depend on the Nb doping of the STO substrates.

3.2.2 Targets and ablation

We investigated the PMN-PT system with two compositions of nominally 0.67PMN-0.33PT and 0.60PMN-0.40PT. Two stoichiometric targets and two additional targets with 5 mol.% PbO excess were purchased from the Fraunhofer Institute for Ceramic Technologies and Systems. Together with PMN-PT targets, a stoichiometric SrRuO₃ target was mounted on the same target carousel. The carousel has 5 target positions, which can be automatically rotated to the ablation position. Additionally, the carousel can be switched to special position between two targets, letting pass the laser beam to the opposite chamber wall where an energy sensor is mounted, measuring the total energy of the laser pulse. Knowing the area of the laser spot on the target, the energy density of the 248 nm UV laser beam can be determined. For the ablation of targets, we used a laser focus with an energy density of 1.0 J/cm², consistent with the typically used values found in literature for growth of PMN-PT and PZT films [72], [94]–[96].

The target surface after deposition was controlled by SEM. Droplets of PbO and cones were found to cover the target surface after ablation. From the EDS analysis, the laser-target interaction sites had a about 10% lower concentration of lead than that of untreated sites. Therefore, a polishing step is necessary before each deposition in order to grow the film from a fresh target surface. Additionally, a preablation step at pulse rate of 5 Hz for 2 minutes was performed prior to each deposition.

3.2.3   SRO film on STO substrate

Figure 3.2 shows a SEM image of a 40 nm thick $SuRuO_3$ film grown on a $SrTiO_3$ substrate. The surface of $SrRuO_3$ has a very uniform and smooth appearance. The TiO_2 termination on the flat (100) surface leads to wetting conditions that are suitable for layer-by-layer growth. The only visible features are the steps of the STO substrate. It is reported that wetting at the steps is less good because Sr is terminating the side wall [81], leading to a kind of trench along the step line. However, our SEM images do not give a clear evidence for this.

Figure 3.2 – SEM image of 40 nm SRO film on STO substrate.
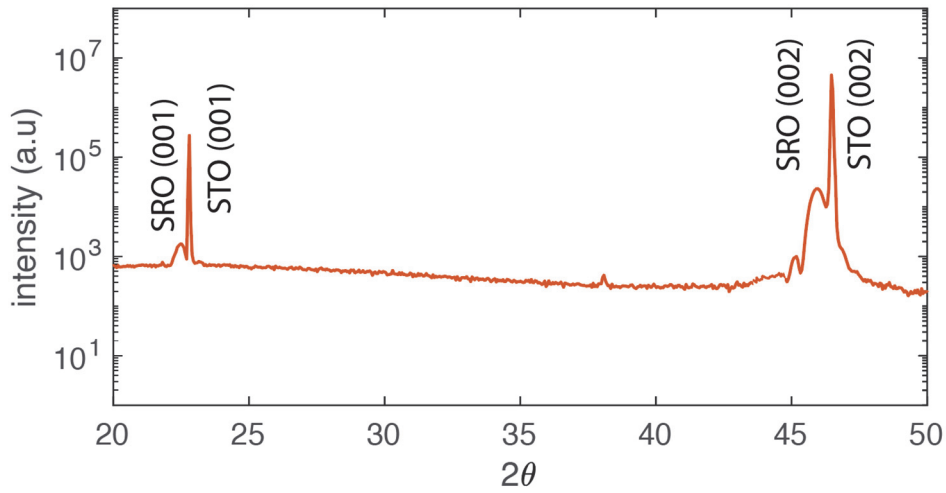
Figure 3.3–XRD theta-2theta scan of 40 nm SRO film sample on STO substrate.

In Figure 3.3, a theta-2theta scan for a 40 nm thick SRO film grown on STO(100) is shown. It clearly showed a pure (00l) orientation. The close matching of lattice constants between $SrTiO_3$ and $SrRuO_3$ promotes coherent growth of $SrRuO_3$. In addition, the scan reveals the very high degree of crystallinity of the SRO by the existence of periodic fringes. The out-of-plane lattice parameter was found to be 3.94 Å.

3.2.4   Substrate temperature influence on crystalline phase formation

The substrate temperature is one of the most important parameters influencing the phase composition of the grown films. The first parameter exploration started with a wide range of sample temperatures between 550°C and 650°C, in combination with a stoichiometric PMN-PT (67/33) target and a fixed O_2 pressure of 0.25 mbar. XRD θ-2θ scans of PMN-PT films are shown in Figure 3.4. For comparison, scan results of an uncoated STO substrate, and an SRO/STO sample are also included in this figure. We observe that the PMN-PT film deposited at 550°C is not crystallized. The films deposited at 575°C and 600°C show a single phase pattern with only (00l) PMN-PT reflections. At an even higher temperature of 650°C, a significant amount of the pyrochlore phase $Pb_3Nb_4O_{13}$ was formed. The high diffraction peak at around 34.3° is attributed to the {400} family of planes, and a small peak at approximately 28° can be identified as the (222) diffraction peak of the same pyrochlore phase $Pb_3Nb_4O_{13}$.

We then focus on the (002) diffraction peaks of PMN-PT (67/33). A closer look of XRD $\theta - 2\theta$ scans of films grown at different temperatures is given in Figure 3.5. The position of (002) peaks of PMN-PT is observed to decrease monotonically with increasing temperature. For film deposited at 575°C, the (002) PMN-PT diffraction peak corresponds to an out-of-plane lattice c = 4.028 Å. This is very close to the literature value of the pseudo-cubic lattice constant of PMN-PT with a = 4.022 Å. The other values of calculated out-of-plane lattice constants are given in Table 3.4. The film deposited at 600°C has a lattice c = 4.040 Å, while the broad shoulder at the left side of (002) peak indicates that a part of the film is compressively strained in the plane of the film. This local maximum of the shoulder resulting from the strained layer reveals c = 4.081 Å.
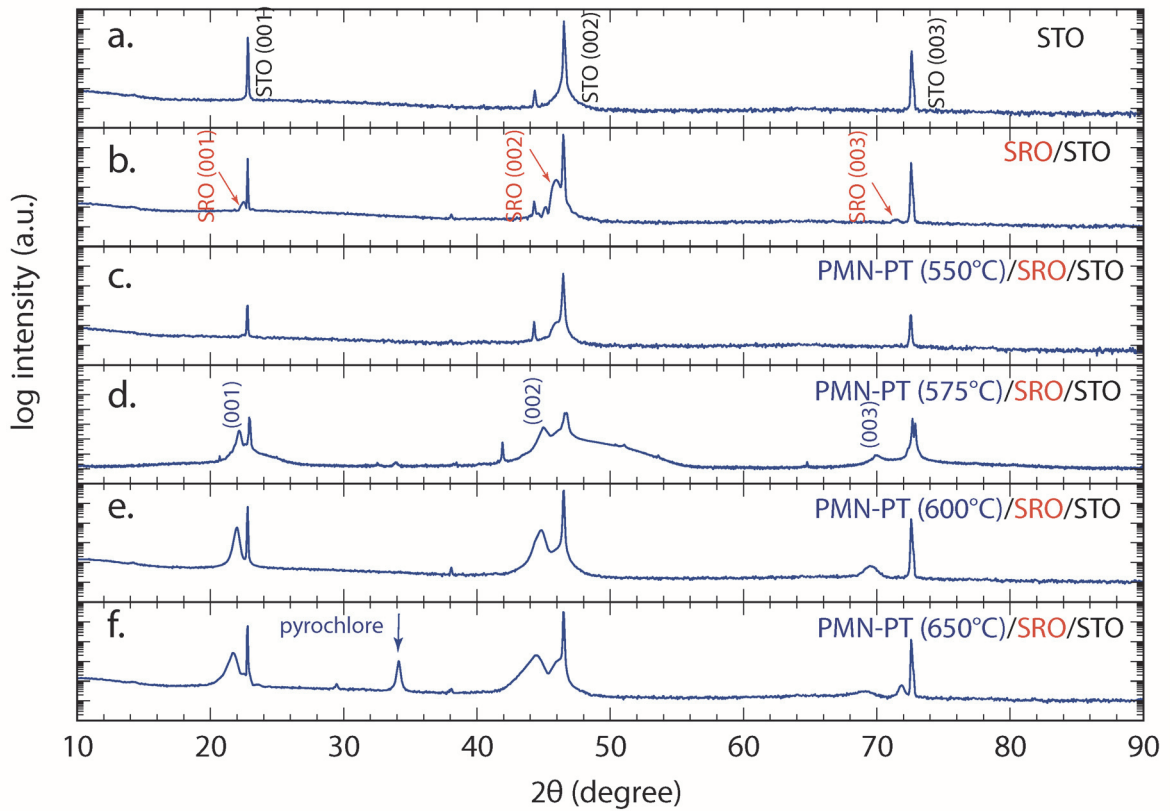
Figure 3.4 - XRD theta-2theta scans of different samples. (a). STO substrate; (b) SRO film on STO; from (c) to (f): PMN-PT (67/33) deposited at 550°C, 575°C, 600°C, 650°C with SRO film on STO substrate. Layer thickness for all the samples: PMN-PT 40 nm and SrRuO₃ 20 nm.
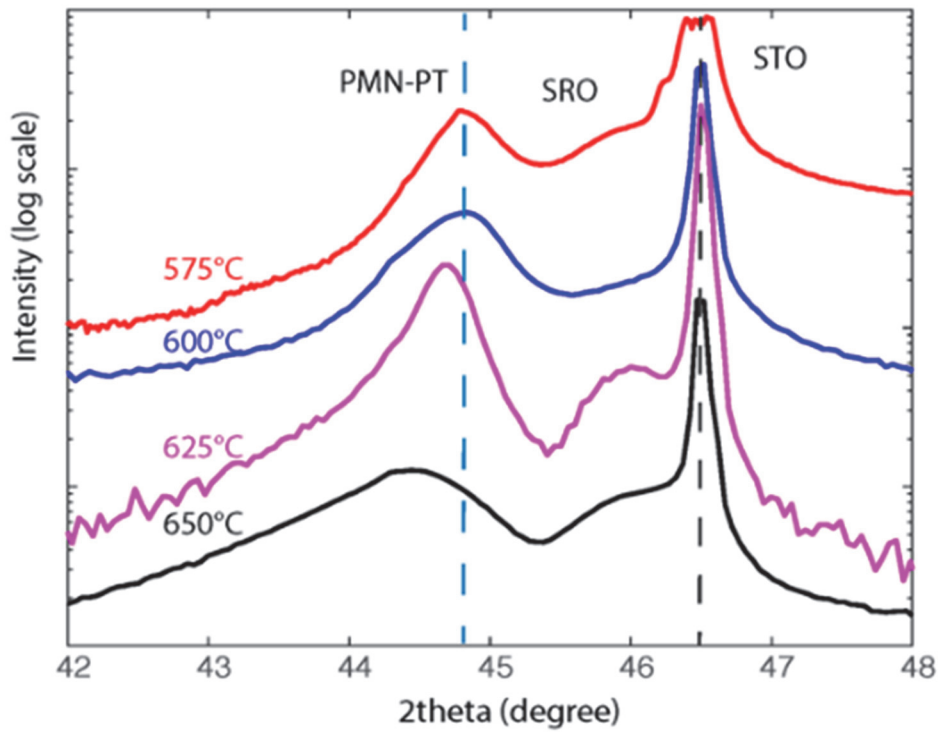
Figure 3.5 - XRD theta-2theta scans of different samples showing (002) diffraction peaks of different layers. From top to down: PMN-PT (67/33) films deposited at 575°C, 600°C, 625°C, 650°C respectively with SRO film on STO substrate. Layer thickness for all the samples: PMN-PT 40 nm and SrRuO₃ 20 nm.

Table 3.4 - Summary of deposition conditions of PMN-PT (67/33) films (with 20 nm SRO buffer layer) and out-of-plane lattice constants.

Sample	Deposition T (°C)	O$_2$ pressure (mbar)	Thickness (nm)	Roughness (RMS.) (nm)	c (Å)
s1	575	0.50	40	0.072	4.028
s2	600	0.25	40	1.532	4.040
s3	625	0.25	40	1.439	4.050
s4	650	0.25	40	1.653	4.074

3.2.5   O$_2$ pressure

The optimization of the substrate temperature resulted in a high-quality, phase pure perovskite thin film growth with (001) orientation. The surface morphology, especially the surface roughness is a further parameter to consider. SEM images of some samples are shown in Figure 3.6. For films deposited with an O$_2$ pressure of 0.25 mbar, in Figure 3.6(a), (b) and (d), the samples exhibit rough surfaces with many small sized grains. The root mean square (RSM) roughness measured by AFM, as shown in Table 3.4, has a typical value of 1 to 2 nm. Such rough surface would be difficult for PFM measurements, due to too much crosstalk between piezoresponse and topography information.

As can be imagined, one solution for improving surface smoothness is to increase the process pressure. At higher pressure, the species from the plume will have lower velocities due to increased scattering. As a consequence, the incoming particles arriving at the substrate surface would have reduced energies, diffuse less far as adatoms, and form a smoother film.
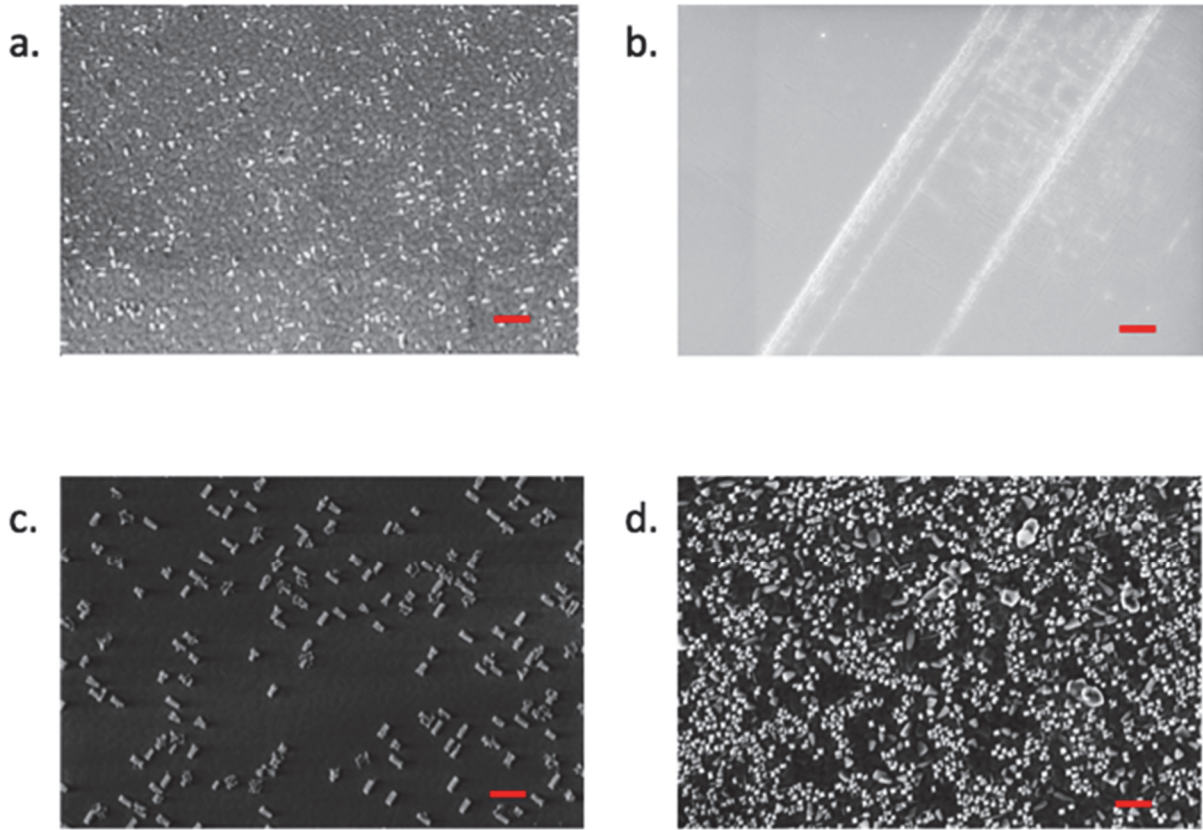
Figure 3.6 - SEM images of surface morphology of PMN-PT/SRO films on STO substrates. Depositions temperatures are: (a) at 550°C; (b) at 575°C; (c) 600°C; (d) 650 °C. Other conditions identical, except for (b) for which an O_2 partial pressure of 0.50 mbar was used, and not the 0.25 mbar as for the other samples (a), (c) and (d). All scale bars are 200 nm.

We only tested the depositions at another pressure of 0.50 mbar with 70 sccm O_2 flow. The perovskite phase pure (001) oriented film state was maintained. The SEM image of one representative sample (Figure 3.6 (b)) revealed that this film had a smooth surface. The root mean square roughness was only around 70 pm, which is ideal for PFM measurements.

Figure 3.7 presents the XRD theta-2theta patterns of two PMN-PT 67/33 samples deposited at 0.25 mbar and 0.50 mbar. Both samples are 40 nm thick with 20 nm SRO on STO substrate. Compared with PMN-PT film deposited at 0.50 mbar, the film deposited at 0.25 mbar exhibit a broader peak, likely due to the small crystals on the surface (similar with the surface as shown in Figure 3.4). The

lattice constant of PMN-PT also slightly reduced from 4.04 Å to 4.03 Å when the deposition pressure changed from 0.25 mbar to 0.50 mbar.
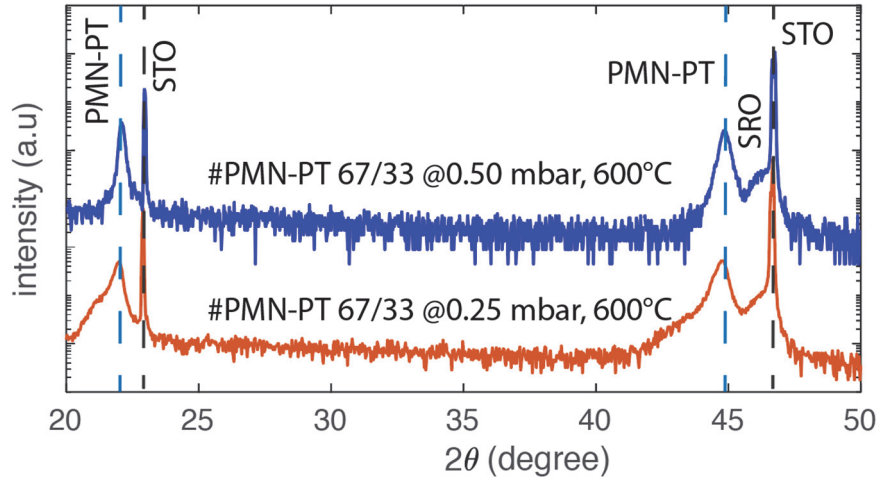
Figure 3.7 – Two XRD scans of 40 nm PMN-PT 67/33 film deposited at 0.25 mbar and 0.50 mbar.

The influence of the O_2 pressure on PMN-PT microstructure appears to be rather complex. In ref. [96] the process pressure was varied between 0.07 mbar and 0.27 mbar. At a rather low pressure of 0.07 mbar, a large amount of pyrochlore was observed. Upon increasing the pressure to 0.13 mbar, the pyrochlore phase disappeared, while the splitting of the (00l) diffraction peaks became evident in the XRD patterns. Increasing the pressure further to 0.27 mbar, the splitting of peaks disappeared. Scattering in the gas has different effects on atoms with different masses. Possibly too much Pb was lost at low pressure – leading to pyrochlore – and too much Ti was lost at higher pressure, leading to a transition from tetragonal to rhombohedral PMN-PT. Besides, the energies of arriving species was reduced by a higher pressure.

3.2.6 Target compositions

It is widely observed that lead is usually deficient in PMN-PT films deposited from a stoichiometric target. As described in section 3.2.2 for target ablation, we observed lead deficiency at the laser-target interaction sites, indicating lead is quite easy to evaporate. To compensate this loss, PMN-PT targets of 5 mol.% excess of PbO were used later for both 67/33, and 60/40 composition. Keeping all the

other conditions the same (575 °C, 0.5 mbar) we compared two samples deposited with a stoichiometric PMN-PT target (67/33) and a target with 5 mol.% lead excess. The SEM EDS analysis results indicate the ratio of Pb/Nb was increased by 6.25% by using the lead excess target. In contrast, the XRD spectra did not show any difference.

3.2.7   Other conditions

Being a versatile technique, the PLD offers also other process parameters than temperature and oxygen pressure to be adjusted for optimal results: the laser energy per pulse, the pulse repetition rate, the substrate-target distance, and in principle also the substrate inclination. The substrate-target distance affects deposition rate, uniformity, and the energy of the deposited species. The species in the plume have a mean free path of the order of a millimeter and start from the target with energies of around 1 eV. The oxygen gas is much colder, as kT is only around 50 meV. Multiple scattering during the flight causes the energy loss. A longer distance will thus reduce the energy of the incoming species. This will reduce the diffusion distance of adatoms, and reduce the faceting of films. Often a smoother surface is obtained with less energetic species.

To summarize this section, phase pure, (001)-oriented perovskite PMN-PT (67/33) and PMN-PT (60/40) thin films, having a low roughness, were deposited at optimized process conditions: O₂ pressure 0.50 mbar, temperature at 575°C, and a laser fluence of 1 J/cm².

3.2.8   Example of one film sample and crystal structure analysis with HRXRD

A sample of PMN-PT (60/40) deposited with a 5 mol.% PbO excess target was studied with high-resolution XRD (HRXRD). According to the deposition rate and time, the layers thickness is expected as 50 nm for PMN-PT and 20 nm for SRO. The Theta-2theta scans including (001) and (002) diffraction peaks are shown in Figure 3.8. The additional satellite peaks, called 'thickness or Kiessig fringes', appear around the PMN-PT (001) peak. The fringes are from constructive interference from X-rays reflected from the top and bottom of the film. Such thickness fringes can only be observed from very homogenous film, indicating the excellent flatness of the film interfaces [59], [60]. More importantly, the periodicity of the fringes can be used to determine the thickness of the layer t in an equation given as follows [60],

$$t = \frac{\lambda}{2(\sin\theta_1 - \sin\theta_2)} \tag{3.1}$$

where, t is the thickness, λ is the incident X-ray wavelength, θ_1 and θ_2 are the Bragg angles for the consecutive interference fringes maxima/minima respectively.

By substituting the corresponding values to equation 3.1, the thickness is calculated as 48 nm, which is consistent with the expected value of 50 nm.
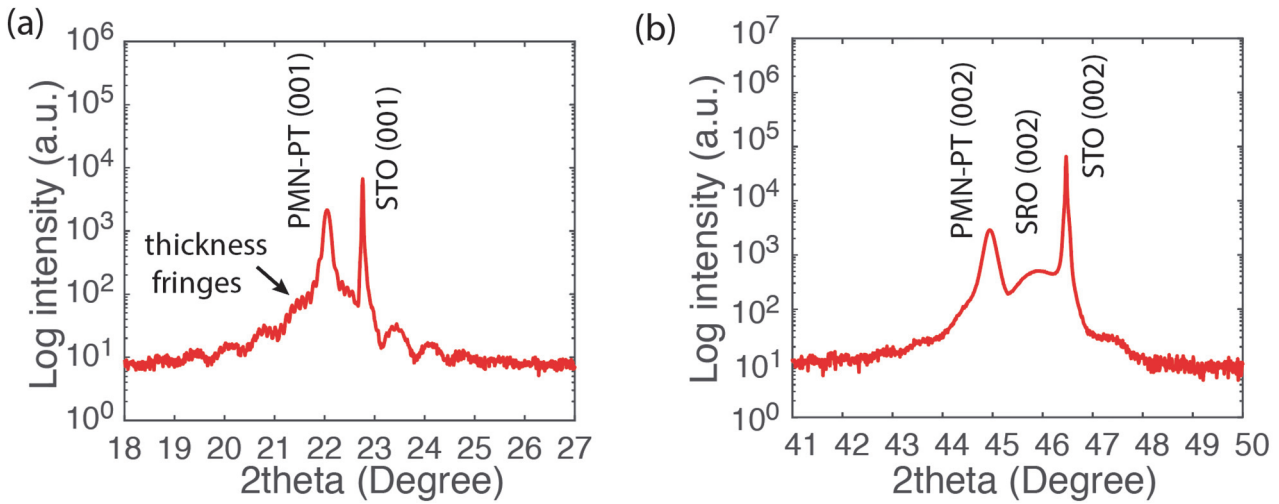
Figure 3.8 - XRD theta-2theta scans of a PMN-PT (60/40) film sample showing (001), (002) diffraction peaks of different layers. Sample layers: 0.60PMN-0.40PT (52 nm)/SRO (20 nm)/(001) STO.

To reveal the structure and strain states of the grown films, the reciprocal space maps (RSMs) results around STO (002) and ($\bar{1}$03) reflections are presented in Figure 3.9. The RSMs results are shown in contour plots of intensity with respect to Q. In reciprocal lattice unit (r.l.u) Q is given as

$$Q = \frac{1}{a} \tag{3.2}$$

From asymmetrical RSM on ($\bar{1}$03) reflections, we find that the SrRuO₃ bottom electrode has grown coherently on the (001) STO substrate. Its Q_x value is the same as the one of STO, and the Q_z value

is slightly increased as compared to the theoretical value, indicating a compression in the plane that is expected in this case. PMN-PT (60/40) film was found to be structurally relaxed (at about 50 nm thick). Both the in-plane a and out-of-plane lattice constants c can be calculated from equation 3.2, by extracting the corresponding Q_x and Q_z from the peaks. The calculation accuracy can be improved by calibrating from the lattice parameter of SrTiO₃, which has a cubic phase with $a = c = 3.905$ Å. Thus, the lattice constants of PMN-PT (60/40) film are found to be $a = 4.001$ Å and $c = 4.031$ Å. The a corresponds quite exactly to the expected a constant of the tetragonal structure with 35 % PT (4.000 Å in [32]), whereas the c is somewhat shorter than the expected c constant for the same composition (4.044 Å in [32]).
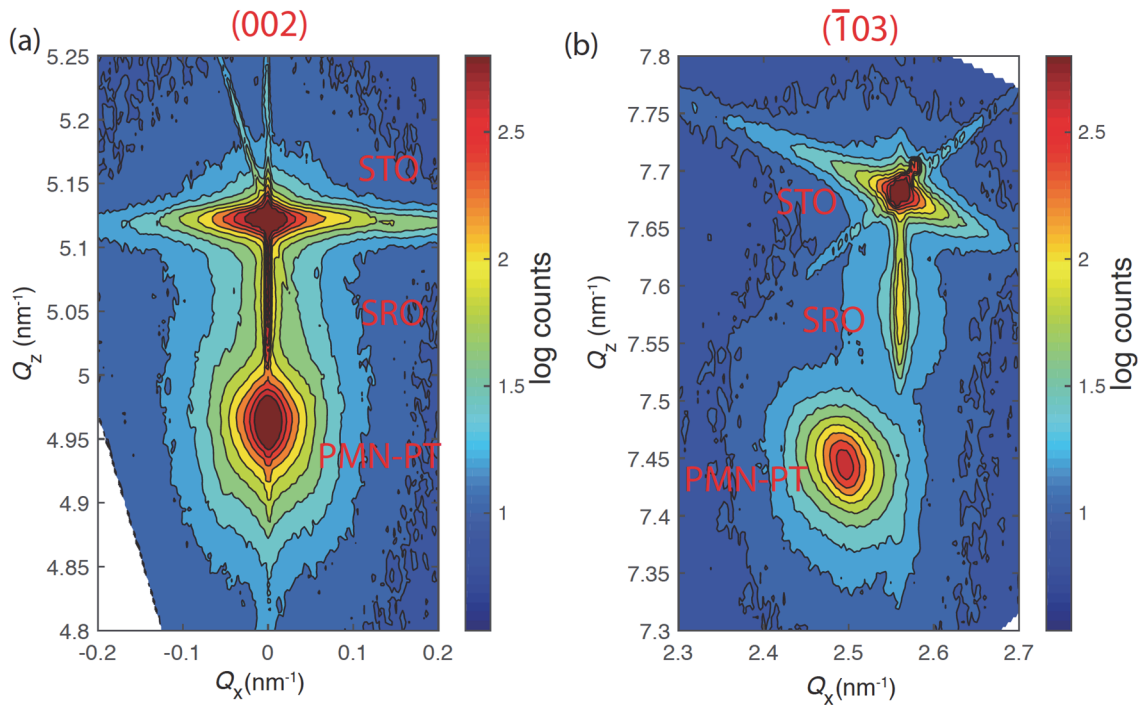
Figure 3.9 - Reciprocal-space maps results around the (a) (002) and (b) ($\bar{1}$03) STO reflections of sample 0.60PMN-0.40PT (52 nm)/SRO (20 nm)/(001) STO. The red color in the scale bar corresponds to highest intensity, while blue color corresponds to lowest intensity. The scale was adapted from logarithmic scale (base 20) to show maximum contrast between different level of intensities.

Figure 3.10 presents the extracted lattice constants of PMN-PT film compared with bulk material constants from Ref. [32]. The values of PMN-PT (67/33) film come from a patterned sample, presented in detail in Chapter 4.
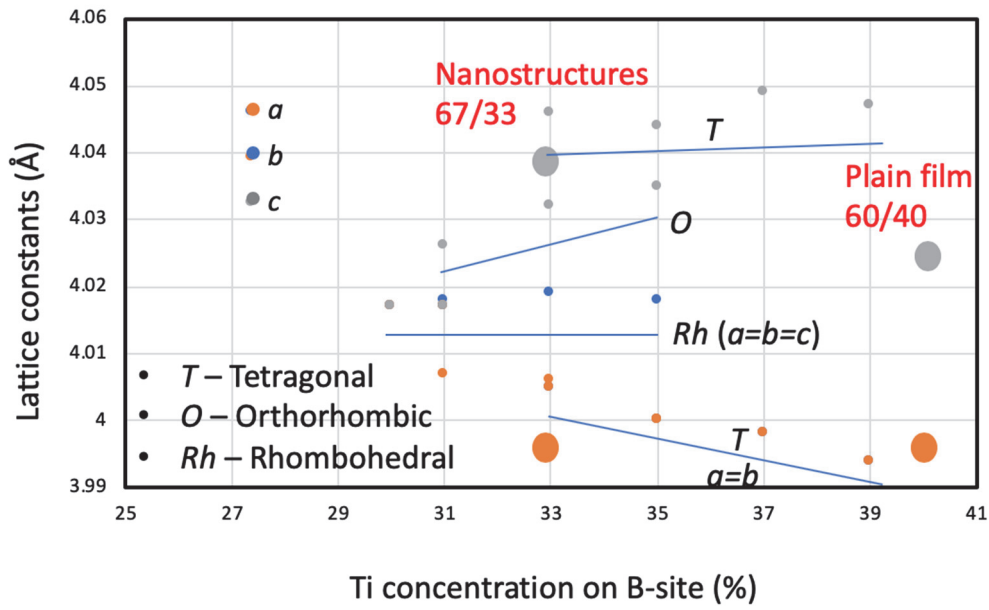
Figure 3.10 – Comparison of lattice constants of PMN-PT. Measured data (in big dots) is extracted from XRDs of 50 nm PMN-PT(60/40) film sample and a PMN-PT (67/33) nanostructured sample. Bulk material data (in small dots) from Ref. [32].

3.3 Experiments and results of sputtering LNO

This section is adapted from a conference proceedings [97] with permission of the publisher:

- Xiao Di, Paul Muralt, Highly (100)-oriented metallic LaNiO3grown by RF magnetron sputtering, 2017 Joint IEEE International Symposium on the Applications of Ferroelectric (ISAF)/International Workshop on Acoustic Transduction Materials and Devices (IWATMD)/Piezoresponse Force Microscopy (PFM), May 2017. © 2017 IEEE.

LNO films have been grown on many materials by various methods, i.e. RF sputtering [98], pulsed laser deposition [99], chemical solution deposition [100]. RF sputtering has the advantage to produce low resistivity, dense films on large area substrates. Sputtering atmosphere and temperature are important parameters for the process. LNO films are almost amorphous when deposited below 150 °C. Above this temperature, the film grows in crystalline form, often with (100)-oriented or textured microstructure. A critical issue is Ni evaporation above 300 °C, leading to Nickel deficiency, and the formation of a parasitic phase of La₂NiO₄ [84], [98].

3.3.1 LNO and PZT film deposition and characterization methods

The LNO films were deposited by RF magnetron sputtering (Balzers BAS 450 PM). The composition of the 5×10 inch ceramics target was the stoichiometric one with a purity of 99.9%. Sputtering was carried out at a power of 1.5 kW (density 4.6 W/cm^2) with a high purity gas composed of 100 sccm Ar and different O_2 flows (5, 15, 33, 67, 100 sccm). Two different substrates on 4-inch Silicon wafers were used: SiO_2(500 nm)/Si and Pt(100 nm)/Ti(2 nm)/SiO_2/Si. The sputtering system base pressure was maintained at ~2.3×10^{-6} mbar before the introduction of sputtering gas. The detailed process parameters are summarized in Table 3.5.

After film deposition, the film resistivity was measured at room temperature (RT) by a four-point probe sheet resistivity measurement system (KLA-Tencor OmniMap® RS-75). Film microstructure and thickness were assessed in a Zeiss Merlin Field Emission Scanning Electron Microscope (SEM). Quantification of compositions were analyzed by Energy-dispersive X-ray (EDX) spectroscopy in the same instrument (Oxford instruments Xmax 150 EDX). Phase identification was performed by x-ray diffraction (XRD) using a Bruker D8 Discover diffractometer (Cu-Ka = 1.5406 Å). Some samples were annealed in a rapid thermal annealing (RTA) tool at 700 °C in 1 atm. Next, 250 nm Pb(Zr$_{0.52}$Ti$_{0.48}$)O$_3$ (PZT) films were grown by sol-gel following the route as explained in [16] including a rapid thermal annealing at 650 °C in oxygen during 1 minute.

Table 3.5 - Summary of deposition and annealing parameters.

Parameters	Values
Background pressure (mbar)	2.3×10^{-6}
Working pressure (mTorr)	6; 6.4; 7.5; 10; 12
Atmosphere Ar (sccm)	100
Atmosphere O_2 (sccm)	5; 15; 33; 67; 100
Substrate temperature (°C)	300
Power density (W/cm^2)	4.6
Process time (minute)	180
Annealing conditions	700 °C for 1 minute in 100 sccm O_2

3.3.2 Crystallinity and microstructure development
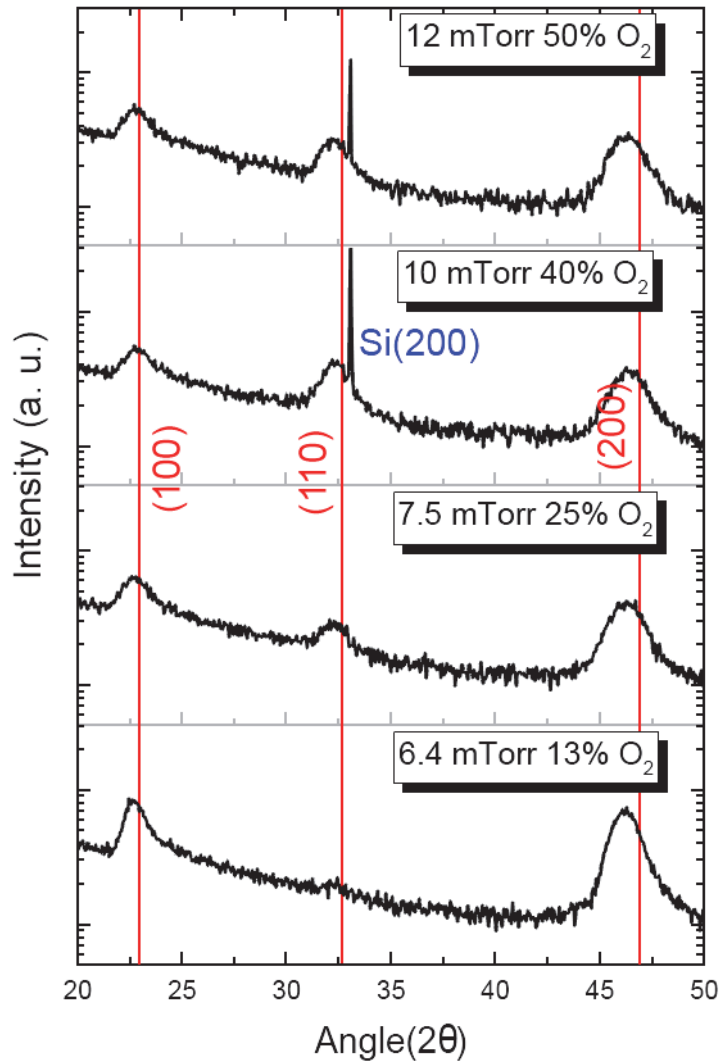
Figure 3.11 - X-ray diffraction patterns of LaNiO₃ films deposited on SiO2/Si(100) substrates at various total and O₂ partial pressures as indicated in the figure. The red lines show the single crystal positions of LNO (100), (110) and (200) Bragg peaks.

Figure 3.11 depicts θ-2θ scans of XRD for a series of LNO films deposited on SiO₂/Si substrates at different O₂ partial pressures. The (100), (200) and (110) peaks of LNO were observed. When deposited at 6.4 mTorr with 13% O₂ atmosphere, the film was almost purely (100)-oriented. At higher total and oxygen partial pressures, a mixed film texture was obtained which included the (110) orientation. At a low O₂ or pure Ar environment, the as-deposit film showed quite weak diffraction peaks, indicating that it was not crystallized (Fig. 3.12). By annealing, the peaks became stronger, sharper and shifted to higher diffraction angles, indicating better crystallization and smaller lattice

parameters. The lattice parameter after annealing, as calculated from (100) peak, is close to the LNO bulk lattice parameter of 3.84 Å. Apparently, tensile strain of the as-deposit LNO film was relaxed during annealing.
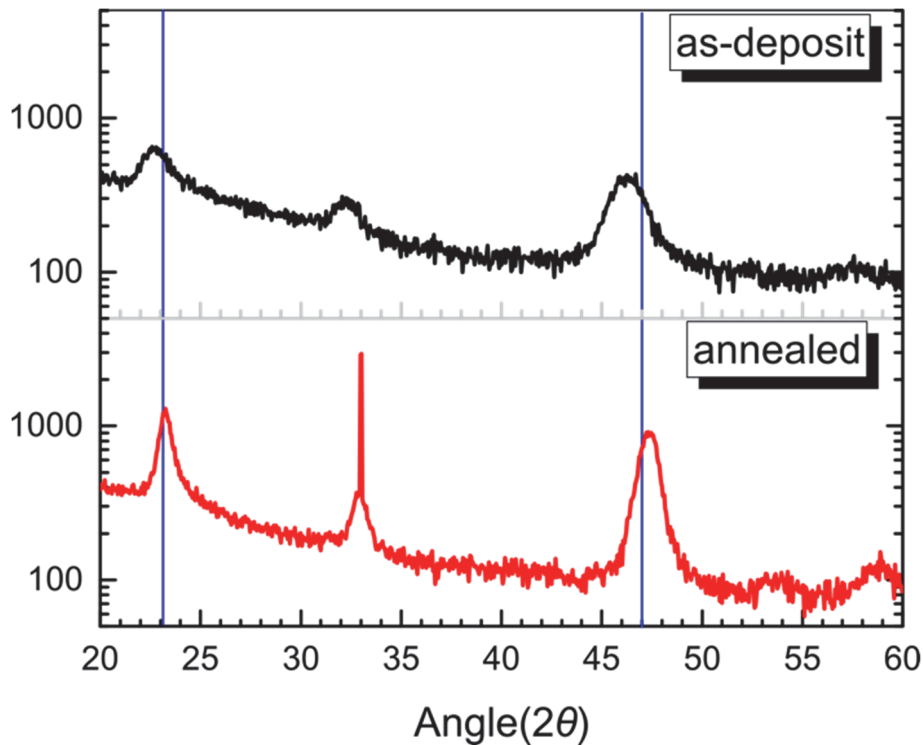
Figure 3.12 - X-ray diffraction patterns of LNO film on SiO₂/Si substrate grown at 25% O₂, 7.5 mTorr working pressure: as-deposit (upper) and annealed (lower curve). The blue lines show the single crystal positions of LNO (100) and (200) Bragg peaks.

The LNO films exhibited smooth surfaces as revealed by SEM images (Fig. 3.13). The microstructure is dense and uniform without cracks. The average LNO grain size was measured as 40±10 nm on the surface. The LNO film displays a columnar microstructure with corresponding thickness of 310 nm. The deposition rate was determined as 0.29 Å /s.
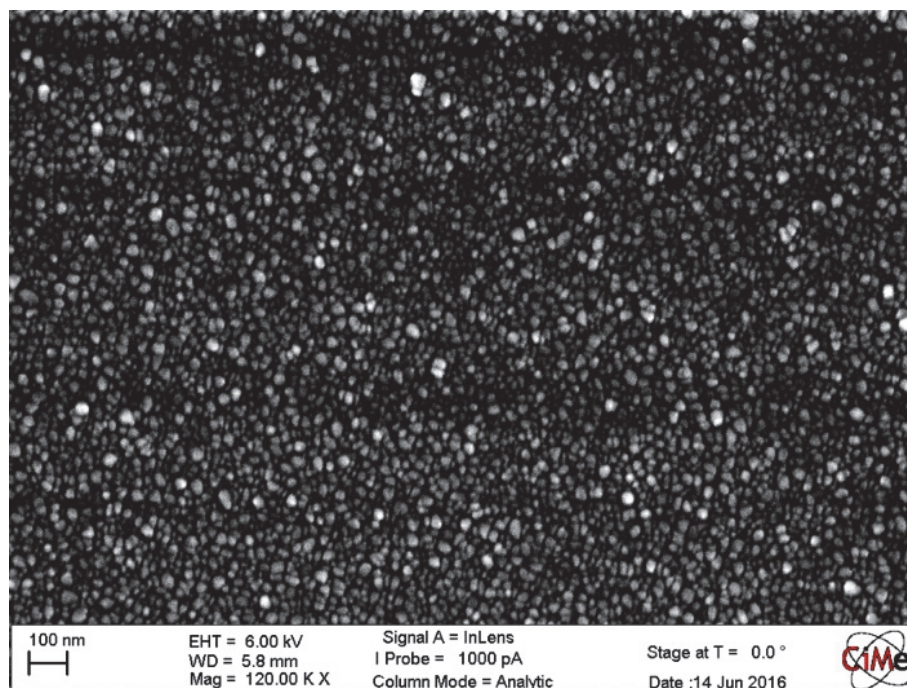
Figure 3.13 - SEM surface image of LNO thin film on SiO_2/Si substrate obtained at 7.5 mtorr in 100 sccm Ar and 33 sccm O_2.

Compositional analysis of the same film was checked using EDX spectroscopy. Two different sites in the center of the sample were investigated. The results are summarized in Table 3.6. In both sites the ratios of La/Ni of the film were almost 50:50, which proved that a stoichiometric $LaNiO_3$ film was realized.

Table 3.6 - Ratio of La/Ni in LNO film at two sites in the center of the sample.

Element	Atomic weight	Site 1		Site 2	
		Weight %	Atomic %	Weight %	Atomic %
Ni	58.6934	30.12	50.49	29.87	50.19
La	138.9055	69.88	49.51	70.13	49.81
Total	-	100	100	100	100

3.3.3   Electrical characterization of LNO thin films

The electrical sheet resistance of the LNO thin films on SiO_2/Si substrates was mapped over the whole wafer area at room temperature (Fig. 3.14). The LNO film had a low and uniform sheet resistance of around 88.7 Ω/square. Knowing the film thickness of 310 nm, a resistivity of 2.75 mΩ·cm is derived. All the measured resistivity results are shown in Table 3. The relatively much higher resistivity of LNO film deposited at 5 sccm O_2 atmosphere indicated that the film was not crystallized, which was confirmed by XRD results. Deposited at 15 sccm O_2 atmosphere, LNO film had the lowest resistivity of 1.92 mΩ·cm. After rapid thermal annealing at 600 °C for 1 minute in 100 sccm O_2, the resistivity became 0.41 mΩ·cm. These resistivity values are consistent with those reported by other authors [82], [84], [85], [98]. The higher resistivity values of obtained with higher oxygen pressures (33, 67, 100 sccm) can be ascribed to the presence of (110)-orientated grains. Annealing at high temperatures lead to significantly higher conductivities, showing that crystallinity is enhanced and oxygen stoichiometry is improved.
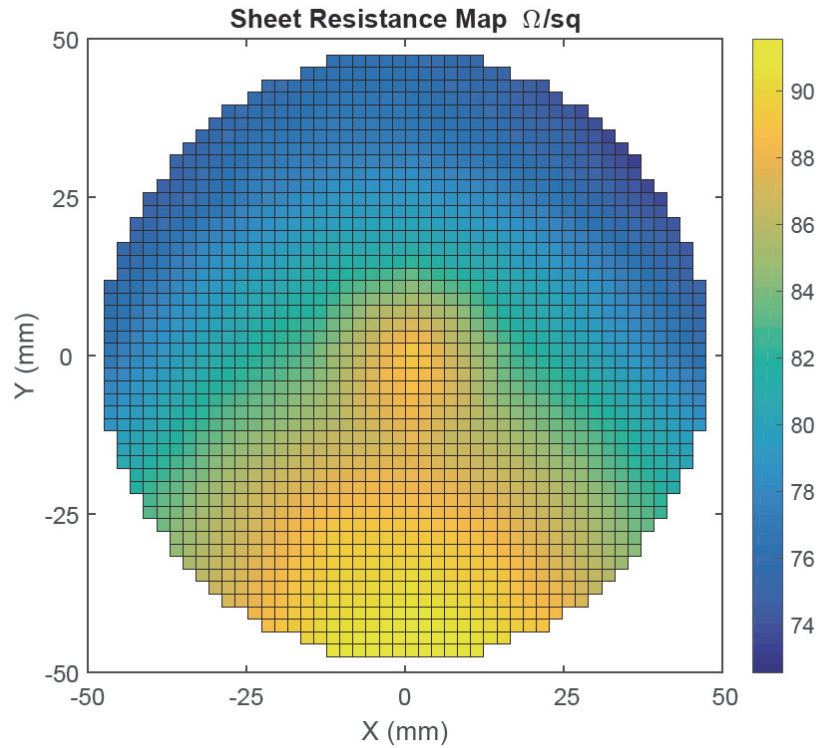
Figure 3.14 - Sheet resistance map of as-deposit LNO film (7.5 mTorr, Ar/O$_2$ 100/33 sccm) on a 4-inch wafer. Mean value 88.7 Ω/square and standard deviation 6.7 Ω/square.

3.3.4 LNO as a seed layer for sol-gel PZT

The same LNO deposition processes were employed to test LNO as seed layer for PZT when using Pt(111) bottom electrodes. The XRD patterns of PZT on LNO-coated Pt/Ti/SiO$_2$/Si and SiO$_2$/Si substrates are shown in Fig. 3.15. Both LNO films were deposited at 33 sccm O$_2$ atmosphere (7.5 mtorr total pressure). The chosen process showed the same mixture of orientations on both substrates. It is not clear whether a pure (100) texture is possible on Pt(111). The PZT 52/48 thin films grown on LNO showed a mixed orientation of 36 % {100}, 48 % {110}, and 16 % {111}. The LNO film had a mixture of 54 % (100) and 46 % (110). This could mean that the mixed LNO orientation seeded about the same mixture for the PZT growth. The {111} orientation of PZT, however, seems to nucleate independently of the LNO seed layer. TEM investigations show at least punctually that grain orientations are passed from LNO to PZT.
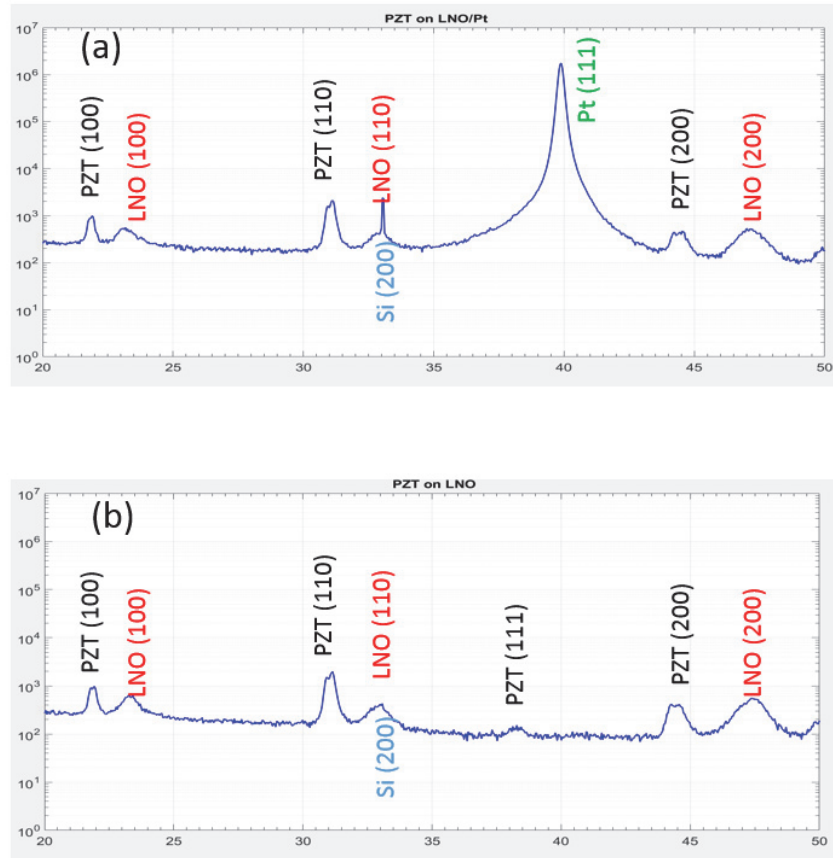
Figure 3.15 - Sol-gel PZT on LNO coated Pt/Ti/SiO$_2$/Si and SiO$_2$/Si substrates (LNO process of 7.5 mtorr).

3.4   Conclusions

In PLD technique, the growth of PMN-PT (67/33) and PMN-PT (60/40) thin films on STO (001) substrates with 20nm-thick SRO bottom electrodes was optimized. The main objective was to obtain a pure perovskite phase and a low roughness. This goal was accomplished by a treatment of substrate surface and optimization of the deposition conditions, most importantly process temperature, and oxygen partial pressure. A sample with a PMN-PT (60/40) film was characterized with HRXRD. The film of 50 nm thickness seems structurally relaxed.

In sputtering technique, LNO film were grown on Pt/Ti/SiO$_2$/Si and SiO$_2$/Si substrates at 300 °C by RF magnetron sputtering. The preferred (100)-orientation could be obtained on SiO$_2$ at relatively low O$_2$ partial pressure. This film exhibited the lowest specific resistivity of 1.92 before, and 0.41 mΩ·cm

after annealing in oxygen. A thin film of $Pb(Zr_{0.52}Ti_{0.48})O_3$ (PZT) was subsequently grown by a sol-gel method on some of the LNO-coated substrates of both types. The XRD patterns of the various samples show that the film textures of the derived PZT films are to a large extent predetermined by the seeding function of the LNO films because of local epitaxy. The crystallized LNO will serve not only as a bottom electrode but also as a seed layer for the growth of highly textured ferroelectric thin films, i.e. PZT [82], [97], [98] and also PMN-PT [101].

Chapter 4 Fabrication of PMN-PT/SRO nanoscale heterostructures

The integration of high performance piezoelectric materials into micro- nanosystems needs to be developed. The patterning technique must be able to create precise structures. The most employed technique for patterning perovskite piezoelectric materials like PZT or PMN-PT is either based on wet or on dry etching [105]–[107]. However, both methods have been reported to induce defects and impurities at interfaces and at the side walls, which critically degrade the piezoelectric and ferroelectric properties of the structures. In this chapter, we demonstrate a lift-off technique to pattern PMN-PT/SrRuO$_3$ heterostructures. The lift-off mask consists of a bilayer of amorphous aluminum oxide (AlO$_x$) and hydrogen silsesquioxane (HSQ). AlO$_x$ serves as the sacrificial layer and mold. HSQ is a high resolution, negative tone electron beam resist. After precise nanoscale patterns are defined by electron beam lithography, HSQ is kept on the surface to form the top mask layer of the HSQ/AlO$_x$ lift-off mask. HSQ is mechanically stable at the high PMN-PT growth temperatures. AlOx does not react with PMN-PT. Tetramethylammonium hydroxide (TMAH) solution used as developer for HSQ, and etches in the same process step the AlO$_x$ layer isotropically. As a result, HSQ/AlO$_x$ bilayer forms an undercut profile, which is a good feature for the lift-off technique. The lift-off mask was then used as a mold for PMN-PT/SrRuO$_3$ local growth. The lift-off step, i.e. the removal of the mask was performed in one step in a NaOH solution. PMN-PT as well as SrRuO$_3$ were grown by PLD at roughly 600 °C. The patterned heterostructures have a minimal lateral dimension of 70 nm. The thickness of the heterostructures grown inside the opening is related to the width of the opening and is less than the plain film thickness. The epitaxial growth of the PMN-PT nanostructures and their crystalline were then verified by TEM and HRXRD studies.

4.1 Introduction

The technique to fabricate well-defined structures on the surface of substrates is essential for device processing. Integrated circuits, MEMS and NEMS devices depend on the perfection of such techniques. Miniaturization of piezo/ferroelectric devices requires patterning of piezoelectric thin films into features on the scale of micro or nanometers. One of the key challenges is to maintain or recover large piezoelectric properties or good ferroelectric switching characteristics of the functional materials like PZT and PMN-PT during or after the patterning process. Over the past decades, a lot of efforts have been made on processing of PZT thin film devices and has lead to successful applications in numerous electromechanical devices. Most often, the patterning of PZT is realized with subtractive approaches through wet etching or dry etching processes, i.e., the unwanted parts are removed be dry or wet etching while the parts that should remain are protected by a mask, which is often a photoresist. The wet etching process typically uses mixtures of strong acids including hydrochloric acid (HCl), nitric acid (HNO$_3$) and a buffered solution of hydrofluoric acid (HF) [31], [102]–[104], [108]. Plasma based dry etching techniques can be either pure physical ion-beam etching (IBE) [109] or reactive ion etching (RIE) [110], [111]. However, both processes suffer some drawbacks. For wet etching with aggressive acid solutions, problems like formation of lead-rich residues, large under-etching and heavy edge damages are encountered. Dry etching has a low etch rate of PZT and poor selectivity between PZT and masking materials. Often hard masks must be applied as photoresists do not withstand the temperature increase during sputtering. In addition, the hydrogen produced during etching reduces PZT and causes oxygen vacancies and formation of OH-groups inside the perovskite. A high-temperature anneal in oxygen is needed to cure this problem, i.e., to recover ferroelectric switching. A schematic view of etching process is shown in Figure 4.1(a).
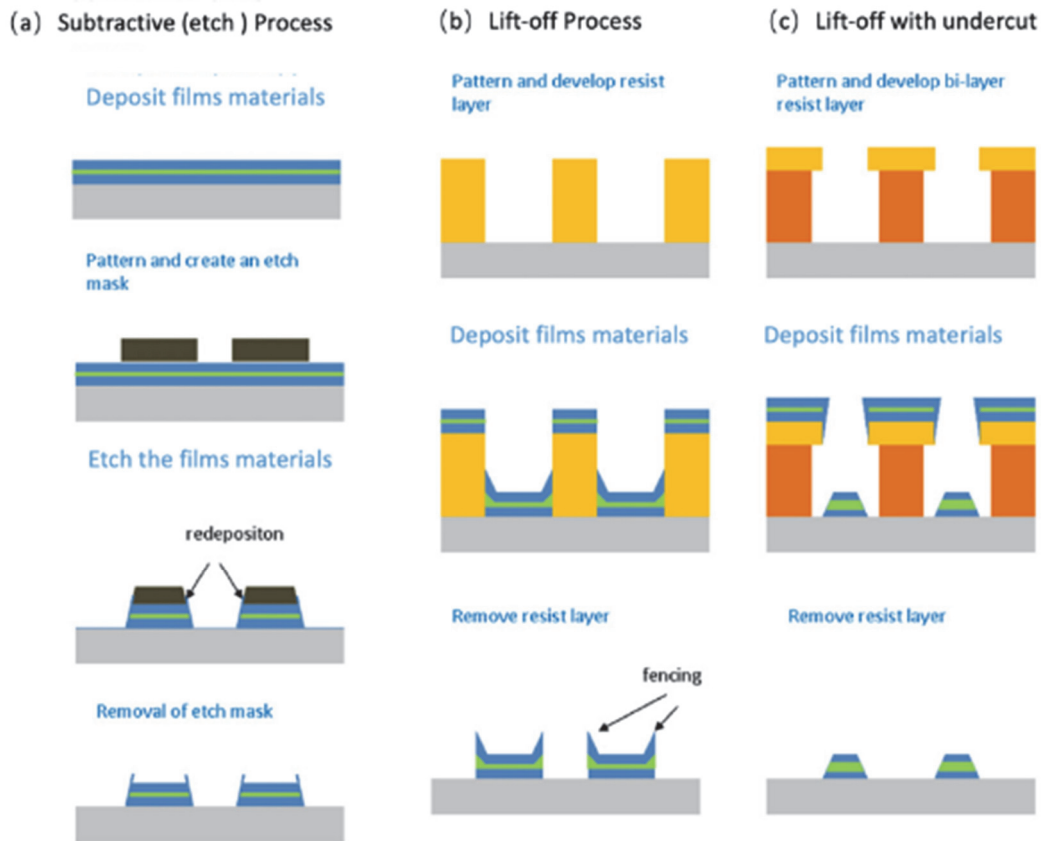
Figure 4.1 - Schematic view of different types of patterning processes: (a) subtractive (etch) process with dry etching; (b) classical Lift-off process and (c) Lift-off with undercut (usually with so-called lift-off resist (LOR). (Adapted from Ref. [112])

The newer material PMN-PT, relaxor-based ferroelectric, has attracted considerable interest due to superior piezoelectric properties. Micromachining techniques for PMN-PT films and bulk single crystals are not fully studied yet. A lot can be learnt from patterning PZT, due to the similarities in their crystalline structures and chemical properties. Peng at al reported firstly the wet etching of PMN-PT single crystals with 10 HCl:10 H2O: (1-x) HF mixture solutions [113]. At various concentration of HF with x ranging from 1 to 5, etch rates were found to be 400 to 800 nm/min. the reactive ion etching (RIE) of PMN-PT uses gas mixtures of Cl_2 and CF_4 or BCl_3 [30], [114]. Etch rate for PMN-PT thin films was reported to be 180 nm/min with BCl_3/Cl_2 gas mixture [114]. A hard mask, such as Ni, is required during reactive ion etching. After etching, the Ni mask was removed and the films were annealed to recover degradations in properties from processing [30]. The etched structures have side-walls with angle of 70°~80°. However, as in dry etching of PZT, the stichometry deviation caused by

etch-byproduct, poor etch selectivity between piezoelectric oxide and resist mask, reductions of films properties due to bombardment caused local stress and redepositions at sidewalls remain challenging for miniaturization PMN-PT. The desire to achieve a high etch rate, vertical sidewalls and a high selectivity of PMN-PT with respect to resist or electrode material is still not accomplished.

Alternatively, focused ion beam etching was used to pattern ferroelectric film into discrete nano islands [115], [116]. Such a 'subtractive' method does not need a pre-defined mask. The PZT nano islands were directly delineated by removing the surrounding region of an island by a Ga^+ focused ion beam with beam size 5-10 nm. Since the ion beam had an energy as high as 50 keV, severe ion damage induced loss of lead and oxygen, and accumulation of gallium impurity [115]. A significant modification of elements stichometry was observed at the ion damage layer. Although precise in submicron size, this method has an extremely low productivity.

Another possibility of patterning is offered by the lift-off technique. The material is deposited in a sacrificial mold, masking the sites where the film should not be deposited [31], [117]. In microelectronics, this technique was very much used in the past employing photoresist as masking or mold material. As the mask has to be stable during the subsequent film deposition at high temperature, polymer masks cannot be used in our case. Lee et al. [117] utilized high-temperature stable self-ordered nano-porous ultrathin anodic aluminum oxide (AAO) membranes as masks during growth of PZT. The discrete PZT nano islands were found to exhibit a high piezoelectric response and were proposed for high-density storage components [117]. However, the lateral size of the achieved ferroelectric nano islands and the pitch are solely defined by the self-ordered AAO and cannot be aligned to a following mask. Recently, Banerjee et al. reported a method using a single layer of AlO_x as high temperature oxide hard mask for the lift-off method. The mask pattern was defined by e-beam lithography with the positive resist PMMA [31], [118], followed by removal of AlOx in an alkaline solution. The PMMA resist layer was subsequently removed in a solvent before the high temperature film growth step, just leaving the AlOx mask. Since films were also deposited on sidewalls of mask during PLD, the lift-off step was hampered by difficulties inherent to the one-layer mask. This simple technique leads also often to fence-like structures at edges [112].

To enable efficient lift-off, undercut profile of the mask layer is desirable. For example, in double layer lift-off or bilayer lift-off method, Lift-off Resist (LOR) 5A is used beneath the top imaging resist [119]. LOR 5A, as sacrificial material, is underetched with standard photoresist developer and

undercut resist profile is obtained. The differences between lift-off process with and without undercut is shown in Figure 4.1(b) and (c) respectively.

Inspired by the bilayer lift-off method, we developed a novel technique by creating an inorganic HSQ/AlO$_x$ bilayer hard mask. Here, HSQ is a high resolution negative-tone e-beam resist [120]. HSQ enables precise patterning of nano-features with the potential to reach dimensions below 10 nm [121]. After exposure, HSQ turns to an amorphous structure similar to SiO$_2$, which is relatively insoluble in the alkaline hydroxide developers, such as TMAH, applied to HSQ (negative resist). Since AlO$_x$ is soluble in TMAH, an undercut profile is achievable in the HSQ/AlO$_x$ bilayer mask, which is favorable for lift-off. It is noticed here, the development of HSQ and etching of AlO$_x$ can be finished in the same step by just adding the process time, without any additional fabrication step. Another benefit of using lift-off is the patterning of electrode and ferroelectric films can be finished in one step when oxide electrodes are used. With this technique we have successfully patterned the epitaxially grown PMN-PT thin films with oxide electrode down to 70 nm diameter features. To examine the crystalline of heterostructures PMN-PT/SrRuO$_3$, we characterized in detail with X-ray diffractions (XRD) and transmission electron microscope (TEM) techniques. The obtained high-quality crystalline form of epitaxial nanostructures proved that the bilayer HSQ/AlO$_x$ mask is capable for patterning ferroelectric film into nanoscale features.
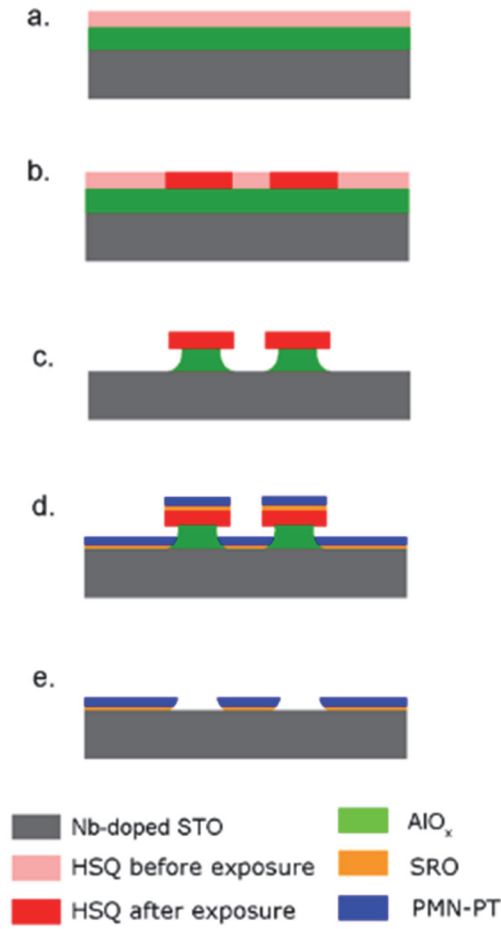
Figure 4.2 - Schematic process flow. a. Growth of AlO_x and spin coating of HSQ; b. HSQ exposure; c. HSQ development and AlO_x etching; d. growth of PMN-PT/SRO by PLD; e. lift-off in NaOH.

4.2   Experiments

4.2.1   Nano Fabrication

Figure 4.2 presents a schematic view of the process flow. PMN-PT and SRO are deposited on Nb-doped $SrTiO_3$ substrates at a temperature of 625°C and 575°C respectively. Heterostructures of PMN-PT/SRO were patterned using the bilayer mask HSQ/AlO_x, which remains stable at deposition temperatures. Following the preparation of atomically flat $SrTiO_3$ substrates with step-terraces profile, a thin layer of AlO_x was grown by atomic layer deposition (ALD) in a Beneq TFS200 system on substrate surface. The AlO_x film deposition is performed by repeating an elementary process loop, which consists four steps. In the first step, precursor 1Tri-Methyl Aluminum (TMA) is pulsed into the reactor and reacts with the hydroxylated surface of the sample, forming a chemisorbed monolayer of O-

Al-$(CH_3)_2$; Next, the chamber is pulsed with nitrogen, removing the excess of TMA and CH_3 byproduct; Then the second precursor H_2O is pulsed into the reactor and reacts at the substrate surface with already existing TMA. The reaction produces monolayer of AlO_x with a byproduct. Finally, the byproduct and excess of H_2O are purged with nitrogen. The two self-limiting surface reactions yielding Al_2O_3 are given as follows: [122]

(1) Al-OH* + Al$(CH_3)_3$ → Al-O-Al$(CH_3)_2$* + CH_4

(2) Al-$(CH3)_2$* + H_2O → Al-OH* + 2CH_4
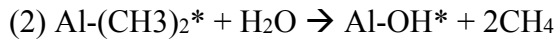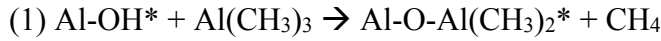
where the asterisks denote the species stayed at substrate surface. The deposition rate is 1.22 Å/cycle. The required thickness is achievable by setting the counts of loops. The deposition temperature was 200°C and 30 nm AlO_x was grown.

In the next step, a 30 nm-thick HSQ resist (XR-1541-002) from Dow Corning was spun on a spin coater at 4'000 to 5'000 rpm. Small features ranging from 20 nm to 1000 nm were written by electron beam lithography system (Raith EBPG5000+) with an e-beam energy of 100 keV at a dose of approximately 1000 $\mu C/cm^2$. After exposure, HSQ was developed for 2 minutes in 25% TMAH. The AlO_x was etched afterwards for additional 16 minutes in the same developer. The pattern on HSQ resist layer is then transferred to the AlO_x layer and the selective area on the substrate is exposed with smooth surface, where the perovskite films can be grown at high temperature. All the procedures for fabrication bilayer HSQ/AlO_x mask on Nb-doped $SrTiO_3$ substrates were performed in class 100 cleanroom at Center of MicroNanotechnoly (CMi), EPFL to minimize contaminations.

The Nb-doped $SrTiO_3$ substrates with patterned bilayer HSQ/AlO_x were subsequently transferred to the PLD chamber for growth of PMN-PT/$SrRuO_3$ heterostructures. The deposition conditions are the same as deposited on plane $SrTiO_3$ substrates, which are discussed in details in Chapter 3. The exposed region, having the same quality of surface, promoted epitaxial growth of PMN-PT and $SrRuO_3$ films. After the high temperature growth and cooling down to room temperature, the samples were put in 6M NaOH aqueous solution in combination with an ultrasonic bath for the lift-off step. The solution attacked the sacrificial layer starting from the undercut. The amorphous solid AlO_x dissolved in the solution and removed the HSQ mask together with the polycrystalline material grown from the PMN-PT vapor that was formed on HSQ. As a result, patterned PMN-PT/$SrRuO_3$ heterostructures were obtained.

The process can be adapted to a design with a $SrRuO_3$ bottom electrode layer covering the complete substrate, if SRO is grown prior the deposition of AlO_x. In this case, the bottom electrode layer $SrRuO_3$ is not involved in lift-off process, thus has not been patterned. This is useful when intrinsic $SrTiO_3$ substrates were used, when a continuous bottom electrode is needed for electrical grounding. All the other steps were kept the same as before. With this process, we ended up with patterned PMN-PT structures on a plane $SrRuO_3$ bottom electrode layer grown on $SrTiO_3$ substrates.

The usage of Nb-doped $SrTiO_3$ substrates is favorable for high resolution electron beam lithography process due to their electrical conductance. For intrinsic $SrTiO_3$ substrates, one problem encountered during the process is the accumulation of electrons on the ebeam resist (HSQ) layer, as the electrons cannot pass to the insulating substrate. To avoid the effect on resolution limits, we used a thin copper foil to connect one corner of the $SrRuO_3$ layer (grown on $SrTiO_3$ substrate) and the eBL tool holder, providing a conduction path for electrons.

4.2.2   Characterization methods

The structures of the samples during the lift-off process are characterized with SEM (Zeiss Gemini and Merlin) and AFM (Asylum Cypher).

For TEM investigations, a thin lamella was taken from a region with patterned squares and lines PMN-PT structures, and prepared by focus ion beam (FIB) milling in a ZEISS NVision 40 system. The selected region was covered by a protective coating composed of carbon and platinum. TEM investigations were carried in a FEI Tecnai Osiris microscope at 200 kV. Scanning TEM (STEM) and energy dispersive spectroscopy (EDS) was used to map the spatially resolved chemical composition.

X-ray diffraction (XRD) theta-2theta scans were performed with a Bruker D8 Discover diffractometer Cu-Kα radiation. The determination of in-plane lattice parameters was done by recording reciprocal space maps (RSMs) in a different Bruker D8 Discover diffractometer equipped with a thin film optics using a Goebel mirror in the primary beam and narrow Soller slits on the detector side.

4.3 Results and discussions

4.3.1 HSQ/AlO$_x$ bilayer mask

The optimal dose of electron beam lithography at 100keV for 30 nm HSQ on Nb-SrTiO3 substrates was found to be 950 to 1050 μC/cm^2. At this dose level, fine features as small as 40 nm were produced uniformly with sharp edges. Although 20 nm-wide features were also observed, the patterns were not uniform and not always reproducible. Figure 4.3 presents the SEM image 40 nm wide openings in a HSQ/AlO$_x$ bilayer mask after etching of AlO$_x$.
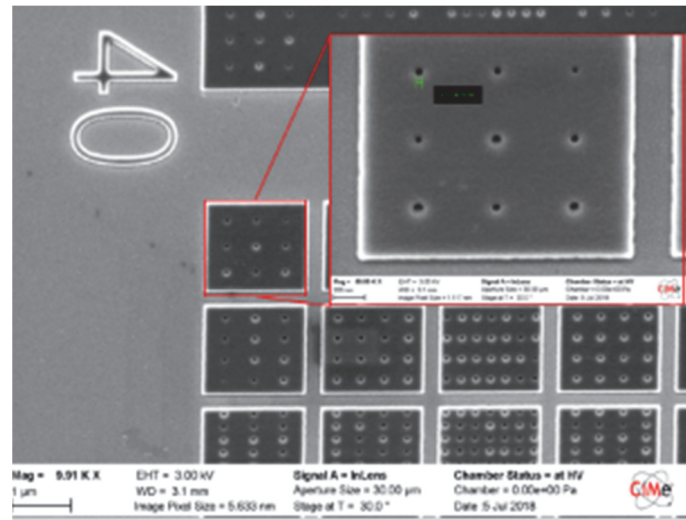
Figure 4.3 - SEM image of features with 40 nm wide openings on HSQ/AlO$_x$ bilayer mask after etching of AlO$_x$.
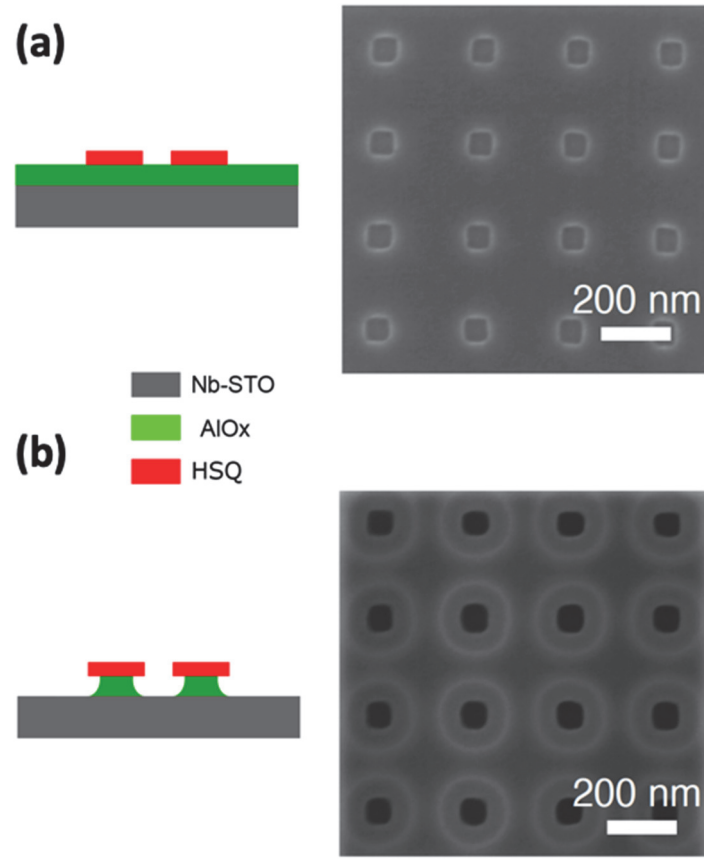
Figure 4.4 - Hard mask fabrication. (a) SEM image of developed HSQ patterns forming 100 nm square openings on AlO_x. (b) SEM image of the same pattern after additional etching in AlO_x, leaving the HSQ unchanged.

Figure 4.4 shows SEM images of the patterns after the development of HSQ only (a) and after etching of HSQ/AlO_x bilayer (b). The corresponding schematic views of the cross-section of the layers are shown in the insets. The circular, brighter rings around the HSQ openings in Figure 4.4(b) show the under-etched profile of AlO_x underneath the HSQ mask. This is attributed to the isotropic etching of AlO_x with TMAH.

To study the dimensions of lateral undercut, a group of SEM images of HSQ/AlO_x openings with different widths were captured, as presented in Figure 4.5. The group of squares have a width $D = 60$, 100, 150 nm respectively. A line profile along a square in each group is plot, as shown in Figure 4.5(d). The plots indicated that the underetching into AlO_x layer of about $u = 35$ nm and seems not depended on the square width. The underetching depth is close to the thickness of AlO_x layer. This can be explained by the fact that the etching rate of AlO_x in TMAH is about the same in the vertical

direction as in the lateral direction. If the etching time of AlO$_x$ is increased, larger lateral underetching is expected.
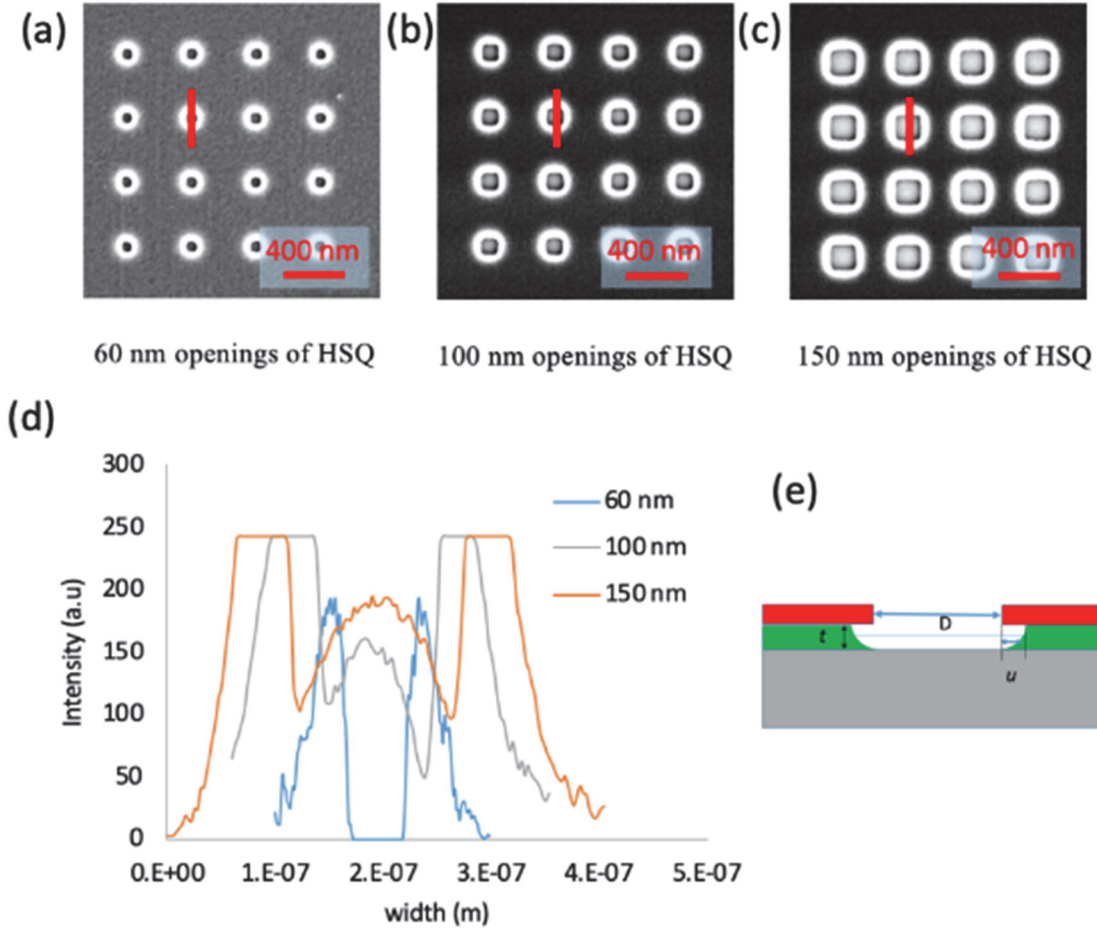
Figure 4.5 - SEM image of fabricated HSQ/AlO$_x$ patterns with square openings of size (a) 60 nm, (b) 100 nm and (c) 150 nm. (d) Line profile along the opening showing the width of the opening, the size of underetch in AlO$_x$. The *y* value does not correspond to the height, but rather the brightness to give a clue of measuring the sizes of the structure. (e) A schematic view of the cross-section of one hole. HSQ is in red, AlO$_x$ is in green and STO is grey.

Figure 4.6 shows AFM images of the patterned HSQ/AlO$_x$ mask on a Nb-doped STO substrate, after etching of AlO$_x$. Figure 4.6(a) is the 3D reconstruction of the mask from the AFM image. The walls with near vertical edges were used to pattern an array of line structures, each line having a width of 1 μm. The height profile in Figure 4.6(b) reveals a total thickness of HSQ/AlO$_x$ bilayer of 55 nm. As we know that the initial thickness of AlO$_x$ and HSQ are 30 nm each, and since AlO$_x$ is more stable than HSQ, the shrinkage in size is likely from HSQ due to the crosslinking during exposure [66].
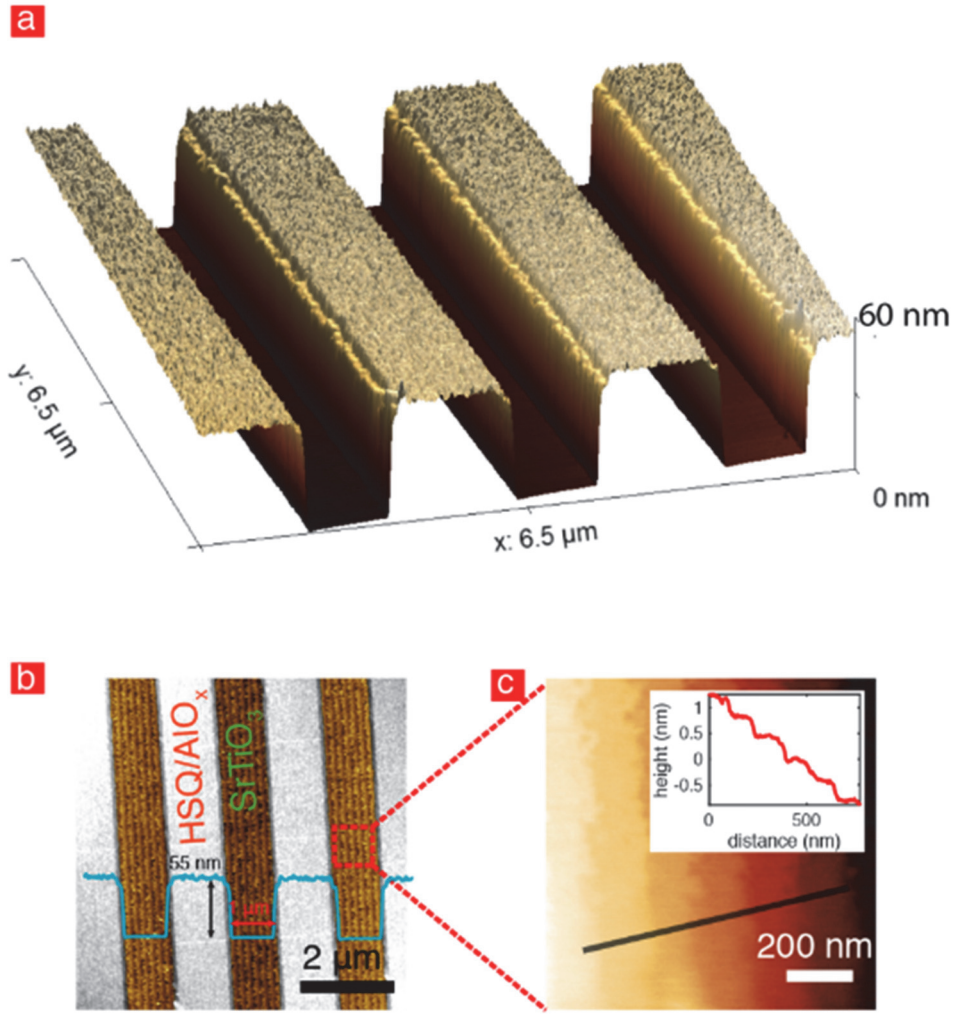
Figure 4.6 - Hard mask fabrication. (a) 3D AFM image of HSQ/AlO$_x$ bilayer mask for fabrication of 1-μm-wide lines. (b) AFM image of the HSQ/AlO$_x$ bilayer mask with the substrates surface exposed in the trenches. (c) Zoom-in view of the SrTiO$_3$ substrate of high quality, having TiO$_2$-termination.

The surface quality of the opening area between the walls was characterized and a representative AFM image is shown in Figure 4.6(c). The substrate surface is smooth and presents vicinal terraces. The inset plotted a line profile confirmed the atomically flat surface with terraces. Thus, the smooth substrate surface with TiO$_2$-termination is of the same quality as before deposition of the HSQ/AlO$_x$ bilayer mask.

4.3.2 PMN-PT/SrRuO₃ heterostructures

Figure 4.7 presents the SEM images of the sample after 40 nm PMN-PT (60/40) and 20 nm SrRuO₃ films deposited on substrates with HSQ/AlOₓ sacrificial mask. From the images, we clearly see that the PMN-PT films showed two distinct kinds of surface morphology. One part of the PMN-PT/SrRuO₃ films, which were grown on HSQ/AlOₓ sacrificial mask layer, showed polycrystalline film with large surface roughness. This is due to the fact that HSQ, as amorphous silica, does not seed an epitaxial growth, and had relatively high roughness (see Figure 4.6 (a)), and possibly reacted with PMN-PT. The other part of the films, either in the widely open region or inside the openings of mask, presented epitaxial PMN-PT/SrRuO₃ films with smooth surface. At least from the SEM images, the film grown on the small exposed area of substrate showed an identical surface quality as on regions that were free of mask layers. Some small-size pyramid like grains, which were observed on plain films, rarely showed up on the films grown inside the small openings of the mask.
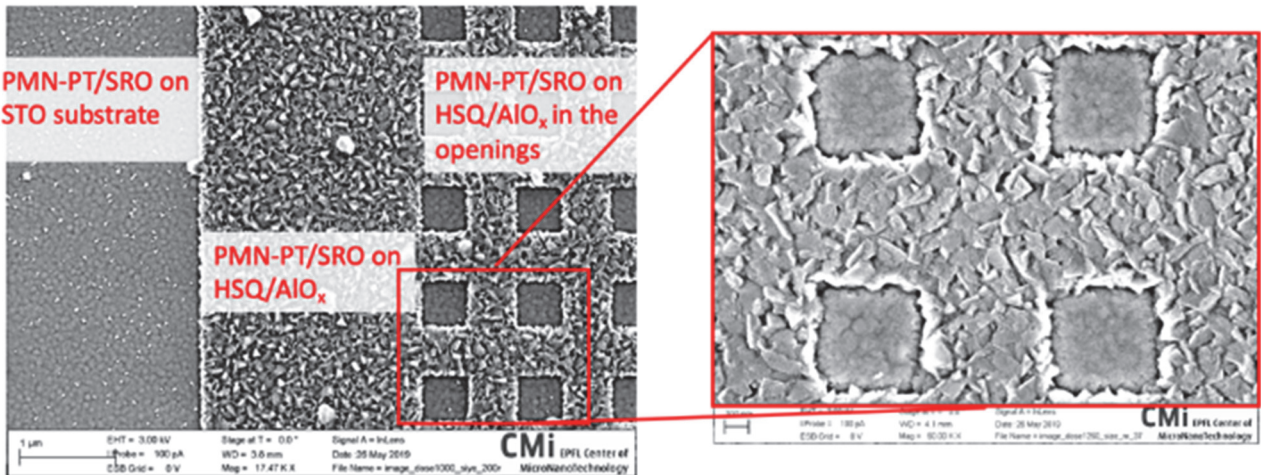
Figure 4.7 - 40 nm PMN-PT (60/40) and 20 nm SrRuO₃ grown on Nb-doped SrTiO₃ substrate with HSQ/AlOₓ sacrificial mask. The left image shows the film grow directly on substrates for comparison. The middle part shows a film section grown on the surface of HSQ/AlOₓ mask. The right part (with a zoom-in view shown in the inset) presents PMN-PT/SrRuO₃ heterostructures grown inside the square openings of the mask.
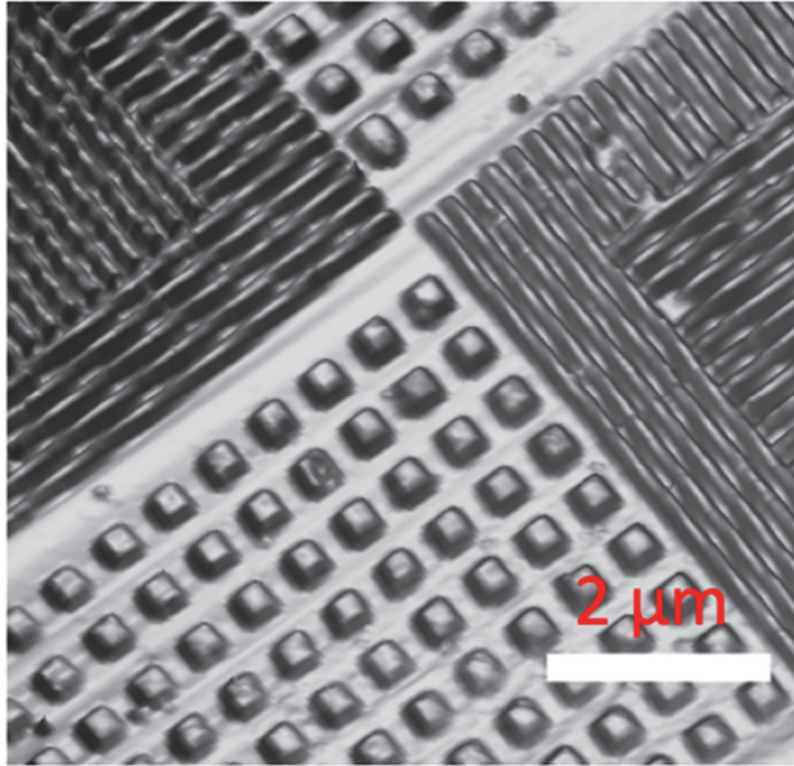
Figure 4.8 - AFM image of PMN-PT/SrRuO$_3$ nanostructures grown on Nb-doped SrTiO$_3$ substrate after removal of the HSQ/AlO$_x$ sacrificial mask.

In the lift-off process, the AlO$_x$ dissolved in basic solutions, removing HSQ and amorphous oxides on top of it, leaving only the pattered PMN-PT/SrRuO$_3$ heterostructures. A large area of the such islands and lines structures was scanned by AFM and the 3D topography is shown in Figure 4.8. It can be noticed that the nano-structures were uniform and clean, well separated from neighboring ones. By a closer look at the surface where the substrate was covered by the mask layers, step-terraces were observed on the AFM images, meaning that the HSQ/AlO$_x$ sacrificial mask was removed completely without some surface modification or residual traces. The film surface was found to have a root mean square (RMS) roughness typically 200 ~ 350 pm.

Figure 4.9 presents AFM images of a group of representative lines and islands structures grown from squares openings with $D = 200$ nm. The structures have widths of about 270 ~ 290 nm and heights of 18 ~ 22 nm. The lateral size extension means that the outer ~ 35 nm of the islands were grown underneath the HSQ mask. In addition to the structures shown here, several other structures with sizes

ranging from 70 nm to micron size were successfully grown as well. The lateral dimensions were always expanded to the limit of the sacrificial mask. This suggested high surface mobility of adatoms and strong lateral growth, as if the matter was poured into the mold. A schematic view of the growth is shown in Figure 4.10(a). The volume of the PMN-PT inside the mold is approximately the missing part of the film above the opening of the square, marked with grid line. The thicknesses of the obtained structures were measured with AFM and plotted as a function of the widths of openings in Figure 4.10(b). The thickness of the nanostructures t_{nano} started at only ~8 nm and increased to a saturation value ~38 nm, the same as the thickness of the unpatterned film t_f. We developed a simple model to explain the thickness variation. First we consider that the volume of the nanostructure is the same as the discontinuous part of the film above it, which is

$$V = D^2 t_{\mathrm{f}} = (D + 2u)^2 t_{\mathrm{nano}} \tag{4.1}$$

where D is the width of the opening, u is the underetching, t_{f} and t_{nano} are the thicknesses of the unpatterned films and nanostructures respectively.
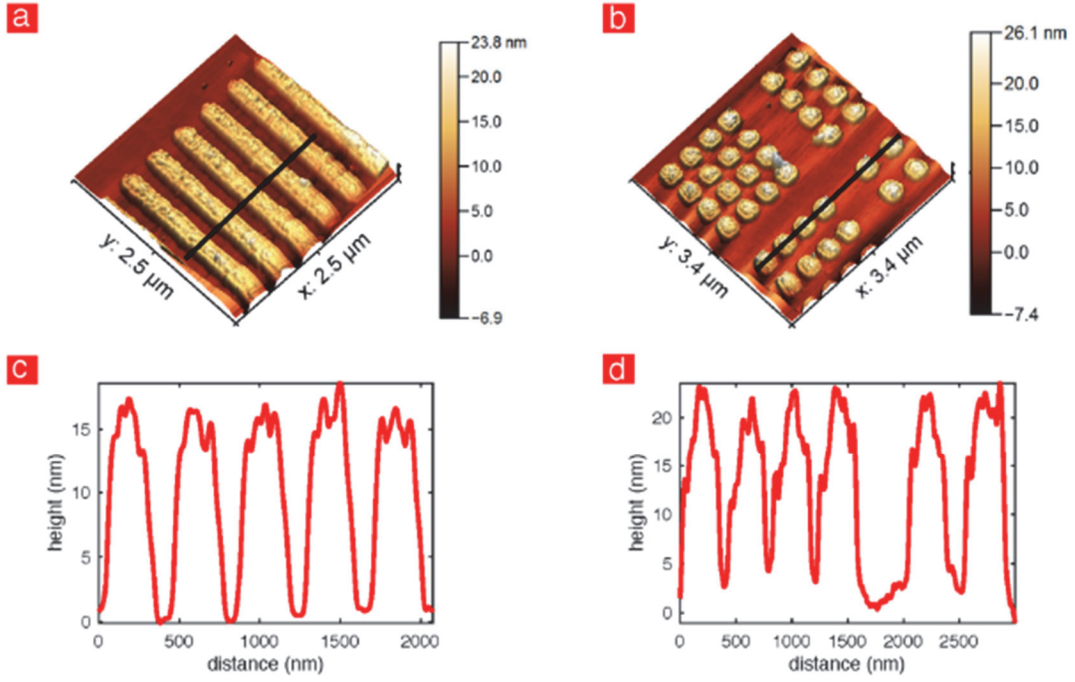
Figure 4.9 - AFM topography images and line scan of nano-fabricated 200 nm wide PMN-PT lines (a) and dots (b) as obtained after PMN-PT deposition and lift-off. Profiles along the indicated lines are shown in (c) and (d), respectively.

We can then easily have

$$t_{\text{nano}} = \left(\frac{D}{D+2u}\right)^2 t_{\text{f}} \tag{4.2}$$

The prediction results of thickness based on this model is plotted in Figure 4.10(b), in relatively good agreement with the measured data. The remaining difference can be ascribed to the deviation from directional impingement of the atomic flux.
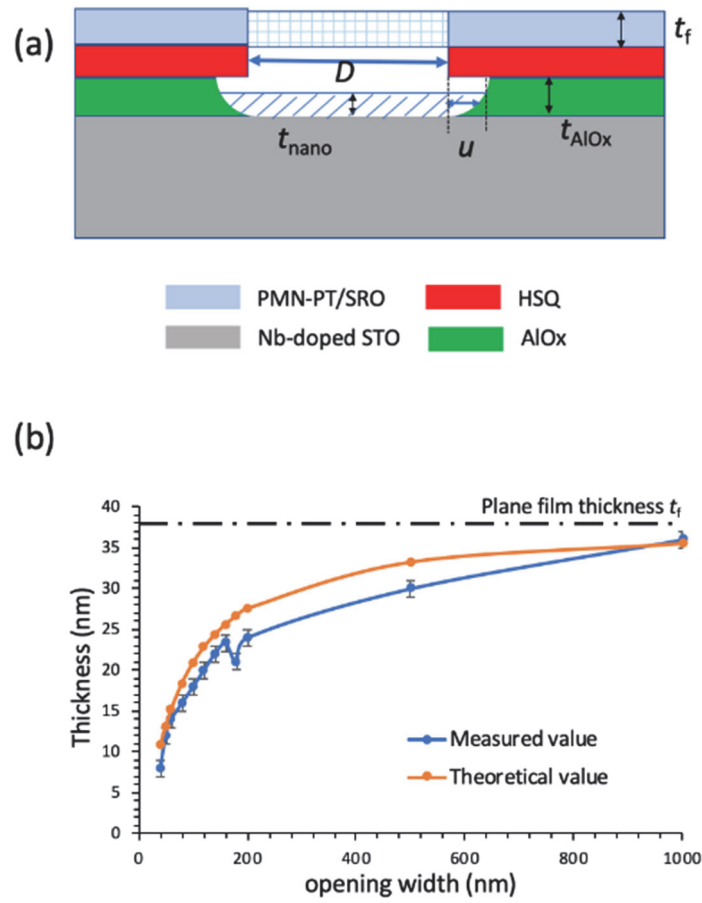
Figure 4.10 - (a) A schematic view of the PMN-PT/SrRuO₃ nanostructures grown on Nb-doped SrTiO₃ substrate with HSQ/AlOₓ sacrificial mask. (b) Measured data (in blue) and predicted value (in orange) of the thickness of the nanostructures.

4.3.3 X-ray diffractions results after lift-off

Figure 4.11 shows representative X-ray diffraction spectra of 40 nm PMN-PT with 20 nm SrRuO₃ sample with patterned nanostructures on Nb-doped SrTiO₃ substrate. The PMN-PT film was grown with a stoichiometric target with composition PMN-PT (67/33). Due to the limited resolution of the X-ray beam in our diffractometer, the measurements were performed inevitably at an area containing both patterned structures and unstructured film. The XRD results, nevertheless, reveal structural information from both parts. As can be seen, the PMN-PT/SrRuO₃ oxides are pure perovskite phase

with (00l) orientation. The intensities of the diffraction peaks of PMN-PT/SrRuO$_3$ from nanostructured films, are much lower than those from plain films of PMN-PT/SrRuO$_3$ sample. This is due to the much smaller volume of PMN-PT/SrRuO$_3$ material on the patterned area relative to the plain film.
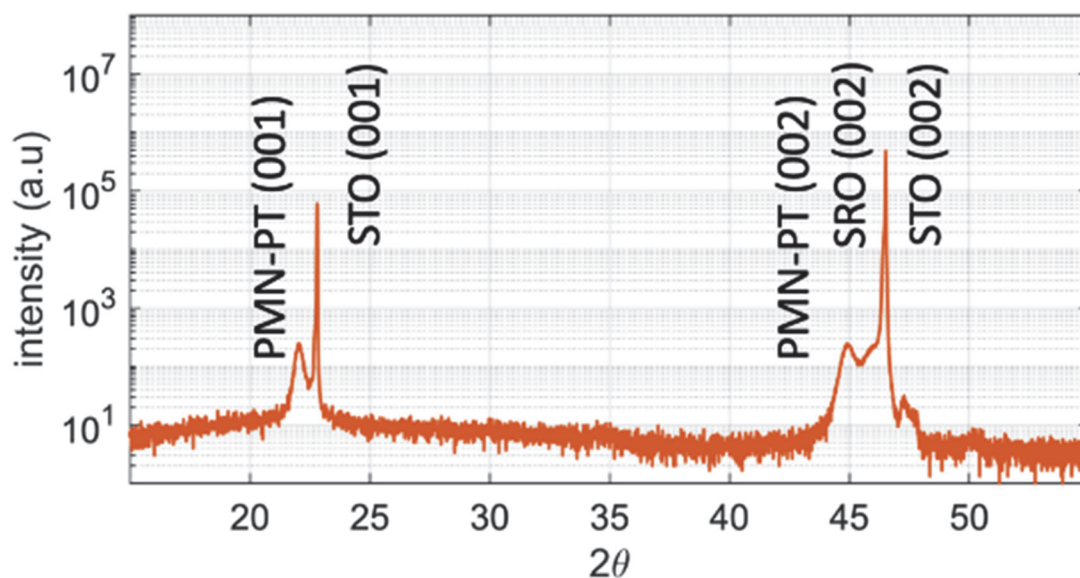
Figure 4.11 - X-ray diffraction spectrum of a sample containing 0.64PMN-0.36PT (52 nm)/SRO (20 nm) films with patterned nanostructures.

Reciprocal space maps (RSMs) measurements were performed for the same sample. The results around STO (002) and ($\bar{1}$03) reflections are shown in Figure 4.12. It can be seen that SrRuO$_3$ is grown coherently on the substrate, which is a result of a small lattice mismatch of SRO to STO (-0.64%), the true layer-by-layer growth, and the small film thickness (20 nm). With its intermediate lattice constant, SRO is in principle an ideal buffer layer between STO and PMN-PT, which exhibits a mismatch of -2.1% between the tetragonal a-axis and STO. As the SRO picks up the lattice constant from STO, PMN-PT, must nevertheless assume the complete mismatch. This relatively large mismatch certainly contributes to the rougher morphology of PMN-PT, which appears to be rather following an island growth mode, or eventually a Stransky-Krastanaov scenario. Both the in-plane and out-of-plane lattice parameters can be determined from RSM results. The lattice constants of PMN-PT are found to be $a = 3.985$ Å and $c = 4.046$ Å. From TEM EDS results (as will be discussed in the following

subsection 4.3.4), the composition of PMN-PT layer is found to be close to 0.66PMN - 0.34PT. Compared to the lattice constants of tetragonal bulk 0.65PMN – 0.35PT with a = 4.000 Å and c = 4.044 Å, the patterned PMN-PT sample has a smaller in-plane lattice, while a slightly larger out-of-plane lattice. The smaller in-plane lattice constant, in combination with a larger out-of-plane lattice constant indicates a residual strain caused by epitaxy (partially relaxed) with a compressed state. The compression increases the out-of-pane strain. The lower intensity of the peaks received from the patterned sample is compatible with the lower coverage (only 10 %) and thickness. More information could be obtained using a high-resolution X-ray diffractometer, i.e., a synchrotron X-ray diffractometer with a beam spot size in micron range [123]. Previous experiment findings from tetragonal 70-nm-sized $Pb(Zr_{0.20}Ti_{0.80})O_3$ patterns revealed that the nanoislands exhibited high tetragonality as expected for this composition, with non-tilted a-domains and elongated c-domains [31], [117], [124]. In our case, the film composition is close to the one of tetragonal symmetry. And, in addition, this symmetry is imposed by the epitaxy on the square lattice of SRO/STO.
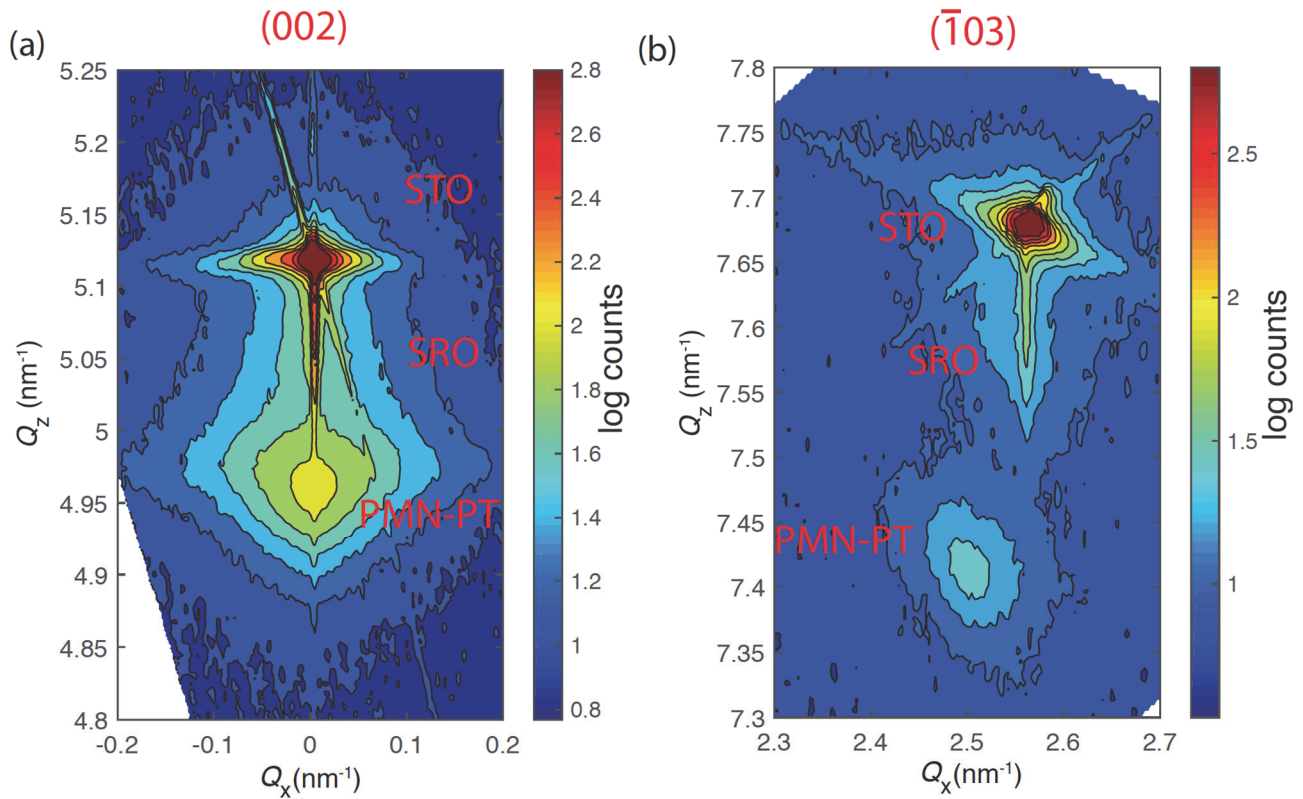
Figure 4.12 - Reciprocal-space maps results around the (a) (002) and (b) ($\bar{1}$03) STO reflections of a sample containing 0.64PMN-0.36PT (52 nm)/SRO (20 nm) films with patterned nanostructures.

4.3.4 TEM investigation results of the nanostructures.

TEM studies were performed for the same sample of 40 nm PMN-PT with 20 nm SrRuO₃ sample with patterned nanostructures on Nb-doped SrTiO₃ substrate. All TEM operations were performed by Dr. Cosmin Sandu at CIME-EPFL. An electron transparent thin lamella was taken from a region with squares and beam structures, as shown in Figure 4.13(a). This region was covered by a protective coating composed of carbon and platinum. A side view of the prepared lamella is shown in Figure 4.13(b). Discrete nanostructures are visible.
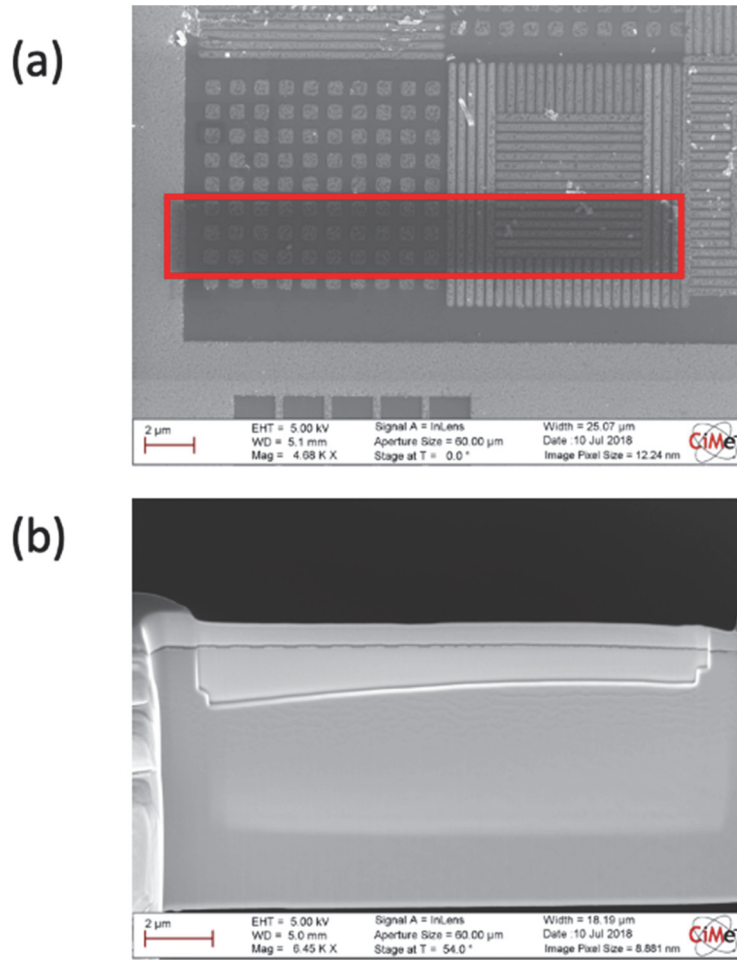
Figure 4.13 - (a) SEM image of the PMN-PT/SrRuO₃ nanostructures grown on Nb-doped SrTiO₃ substrate with HSQ/AlOₓ sacrificial mask. The red rectangle denotes the region is chosen for TEM lamella preparation. (b) Side view of the prepared TEM lamella. Discrete nanostructures are visible at the interface.

We then characterize some of the nanostructures. TEM images of a PMN-PT/$SrRuO_3$ heterostructure are shown in Figure 4.14. The diameter derived from the cross-section image amounts to 300 nm. It was obtained with a mask opening of 250 nm. The outer 25 nm were grown underneath the HSQ mask. It is noticed that this boundary region is hardly thinner than the rest of the structure, as if the matter was poured into the mold. This is a sign of high surface mobility of adatoms and strong lateral growth. As a consequence, the PMN-PT/$SrRuO_3$ heterostructures have a profile following the shape of the AlO_x mold, producing the obtuse angle at the edge of the nanostructure. Since the edge is suspended, the strain state must be different, a modified domain pattern is expected.

A high-resolution TEM image (HRTEM) is shown in Figure 4.14c. The bright region around the nanostructure consists of carbon, which is topped by a platinum layer. Together, these layers protect the sample during focused ion etching when preparing the lamella. HRTEM confirmed that the nanostructures consist of epitaxially growth single crystals, even at the outer border. From the fast Fourier transform (FFT) patterns, shown in the insets, the same {100} orientation of PMN-PT and $SrTiO_3$ were observed, confirming the XRD results.

A combination of TEM and energy dispersive spectroscopy (EDS) was used to analyze the chemical composition and its spatial distribution (Figure 4.15a). A very focused, narrow electron beam was employed to measure a line scan (line 1 in Figure 4.15a). The elemental intensities are depicted in Figure 4.15b. The intensities of region 2 (Figure 4.15a) were integrated to obtain an energy scan with a reasonably low noise, shown in Figure 4.15c. These figures reveal that the $SrRuO_3$ layer has a uniform thickness of 10 nm, and sharp interfaces with STO and PMN-PT. It grows nicely in a layer-by-layer mode. In contrast, the PMN-PT thickness varies between 8 nm to 14 nm, which can be explained by an initial nucleation of separate grains (island growth). The resulting roughness leads to a reduced slope of composition intensities at the PMN-PT surface as compared to the interface with SRO. The Mg peak is relatively weak. This results in an artificially increased relative intensity inside STO due to a relatively higher noise level from the background.
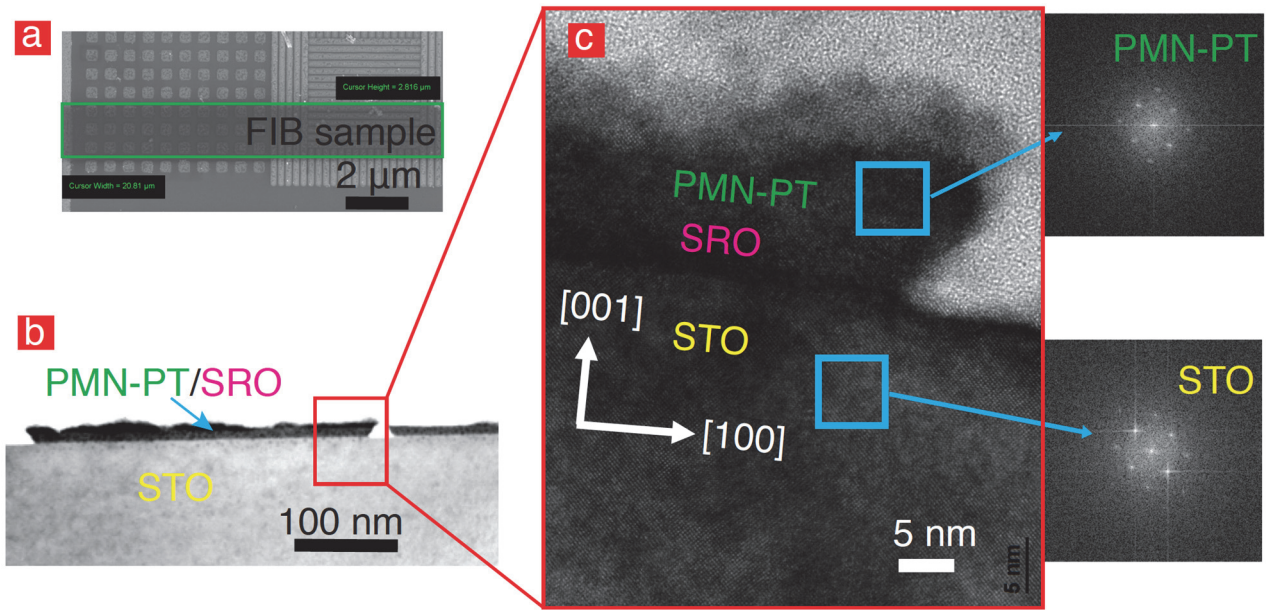
Figure 4.14 - (a) SEM image of pattered structures for TEM invetigations. (b) PMN-PT/SrRuO₃ heterostructures cross-sectional TEM image of the nano-lamella. (c) High-resolution TEM image of PMN-PT, SrRuO₃ and SrTiO₃. Electron diffraction patterns shown in the insets prove that the PMN-PT nanostructure is an epitaxial single crystal even inside the edge structure.

The elemental composition of PMN-PT was derived from spectrum Figure 4.16c. The data were obtained from the peaks that do not overlap. The quantitative analysis of all the elements is shown in Table 1. The ratio of PMN and PT is about 64/36; this is slightly lower than the value of 67/33 of the target. The ratio between Pb and the total amount of Nb, Ti and Mg amounts to 0.87, indicating a lead deficiency due to lead loss during deposition. The ratio between Nb and Mg is obtained as 2.11, which deviates only by 5 % from the expected value of 2.0. The obtained composition indicates that the film is in the tetragonal state. This result confirms the XRD data. The observed lead deficiency motivated as to use henceforth a target with a 5% lead excess.
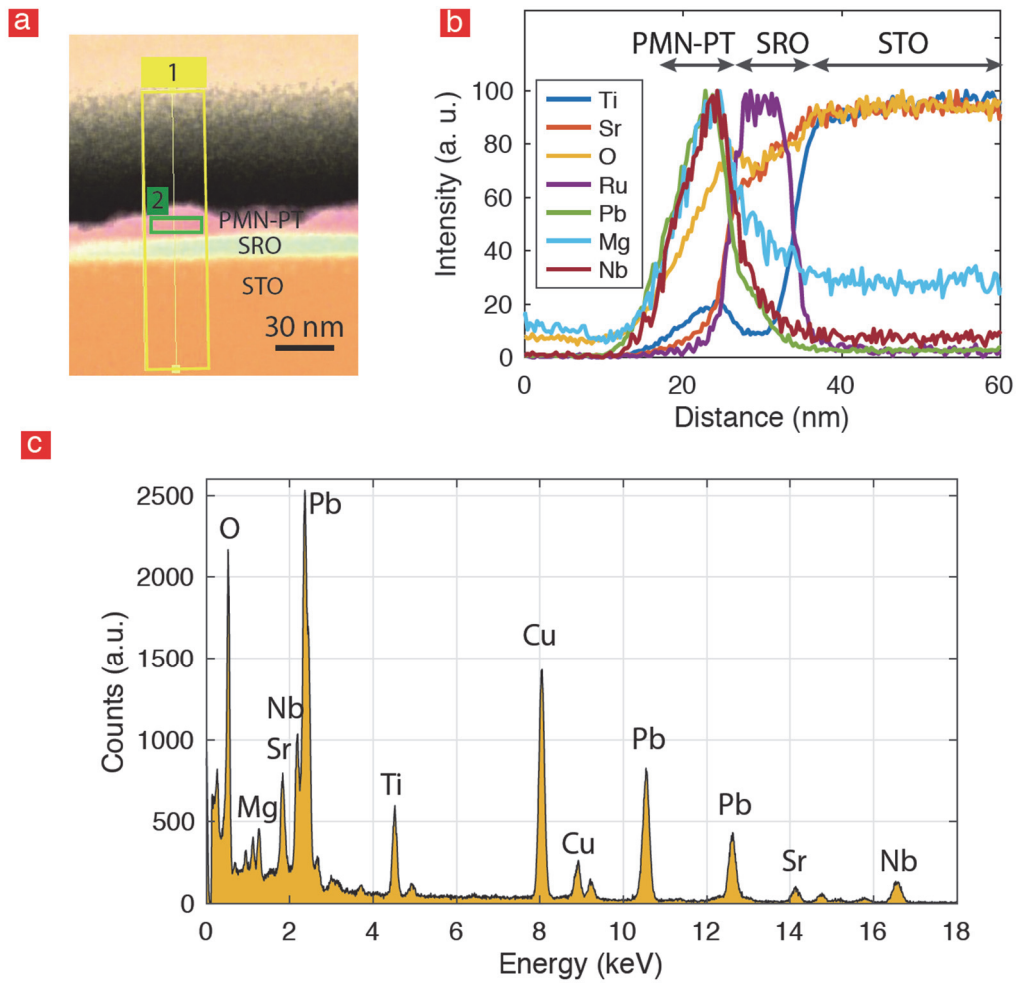
Figure 4.15 - STEM-EDS mapping of a PMN-PT nano lamella, as shown in fig. 5. (a) False-colour elemental composition map. (b) Elemental composition line scan along line 1 in (a) shows the distribution of Pb, Mg, Nb, Sr, Ru, Ti and O across the layers. (c) Labelled EDS spectrum from the PMN-PT region marked with rectangle 2 in (a).

Table 4.1 - EDS Quantitative Analysis of PMN-PT nanostructure

Element	Line	weight %	atomic %	Target
Mg	K	1.1	4.5	4.4
O	K	9.6	60	60
Ti	K	3.8	8.0	6.7
Pb	L	39.8	19.2	20
Nb	L	8.8	9.5	8.9
Sum		100	100	100

Figure 4.16 shows the EDS maps of all the elements (except O which presents in all layers) for PMN-PT (64/36)/SrRuO$_3$ heterostructure grown on Nb-doped SrTiO$_3$ substrate. They illustrate that SrRuO$_3$ layer was uniform with clear interfaces with STO and PMN-PT, as verified by the value of intensity of Ru shown in Figure 4.16c. The Mg, Nb intensities are weak, resulting in noisy maps. The maps of Pb, Mg, Nb in PMN-PT follow well the shape of PMN-PT layer with variant thickness. The intensities of Pb, Mg, Nb and Ti is slightly higher at the interface. However, the low signal-to-noise ratio, as well as the very small thickness of PMN-PT layer, makes this observation ambiguous.
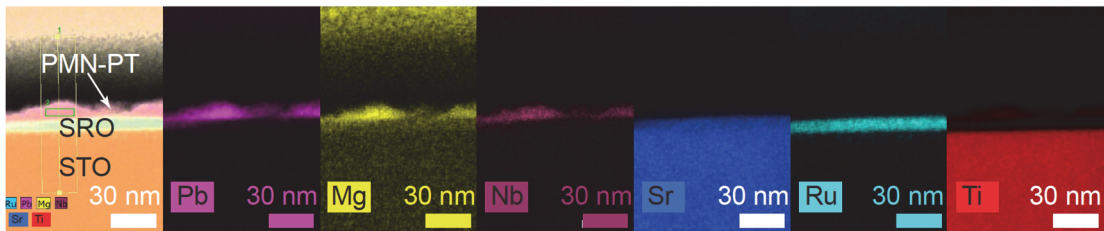
Figure 4.16 - (a) EDS map for different elements for PMN-PT (64/36)/SrRuO$_3$ a nanostructure grown on Nb-doped SrTiO$_3$ substrate with HSQ/AlO$_x$ sacrificial mask.

4.4   Conclusions

In conclusion, we have developed a process to fabricate epitaxial nanostructures of PMN-PT on Nb-doped $SrTiO_3$ substrate. The bottom electrode layer can also be patterned in the same step. The patterning process utilizes a sacrificial mask consists bilayer of HSQ/AlO_x, where HSQ is a high-resolution negative tone ebeam resist. The formed undercut profile of the bilayer mask is favorable for lift-off. The deposited oxides grew inside the nanostructure-confined region and expands in the mold. The thickness of the nanostructures increased with expansion of the opening width, and becomes finally close to the thickness of unstructured film.

A representative device was studied in detail with SEM, AFM, XRD and TEM. The minimum features obtained are $\sim$ 70 nm dots. From 250 nm openings in the bilayer mask, the obtained structures have a lateral dimension of $\sim$ 300 nm. The TEM and XRD results proved that the heterostructures were epitaxially grown. The PMN-PT layer was deposited using stoichiometric targets with compositions 67/33, and the film composition was found to be $\sim$ 64/36, in tetragonal side. The sample with nanostructures and unstructured film was probed by high resolution reciprocal space maps (RSMs), the results indicated the sample have slightly higher c. This is likely due to domains with elongated c-axis in PMN-PT nanostructures under compressive strain on $SrRuO_3/SrTiO_3$. High resolution characterization approaches are required to directly study the insights of the lift-off fabricated PMN-PT nanostructures.

Chapter 5   Piezoresponse force microscopy measurements

In the previous chapters, we have developed PMN-PT thin films and a lift-off route to fabricate nanostructures. Both, the films and the nanostructures exhibit the desired phase and composition, as was proven by HR-XRD and TEM/EDS characterizations. However, we do not have a direct evidence for their ferroelectricity. To answer this question, we investigated the PMN-PT films and nanostructures by means of piezoresponse force microscopy (PFM). Two compositions of PMN-PT were studied: PMN-PT 64/36 and PMN-PT 60/40. The studied film samples had a thickness of 20 to 50 nm, while the nanostructures had a thickness between 10 nm to 22 nm. We first mapped the domain patterns from the as-deposit samples, and then poled and switched polarization by applying a DC bias on the tip. The PFM results revealed that the samples were ferroelectric. The PMN-PT nanostructures were individually addressable, preserving ferroelectric properties. Our results show a clear polarization switching of the patterned, 12 to 15 nm high PMN-PT nanostructures with a stable piezoelectric response that was larger than ~10 pm/V and possibly reaching even ~100 pm/V, Furthermore, short-range ($10 - 20$ nm) ferroelectric domain patterns prominently appear after poling the nanostructured ferroelectrics, indicating the coexistence of 180 ° domains.

5.1   PFM experiments

The PFM measurements of out-of-plane piezoresponse were performed with the AFM Cypher from Asylum research of Oxford instruments. The samples were attached to a conductive AFM stage with silver paint (G3692 from Plano GmbH). A wire with magnet heads was used to connect the stage to the ground signal. The Igor Pro v. 15.09.112 program was used for the real time control of the AFM and the data acquisition.

5.1.1   Probes

Two types of conductive probes were used, one type is ASYELEC.02-R2 (Asylum Research) and the other type is HQ:NSC35/Pt (MikroMasch). For some samples, we only measured the AFM topography with ac-taping mode using tips of type Scanasyst-Fluid+ (Bruker). Details of the tip are given in Table 5.1.

Table 5.1 - Details of the tips used for AFM measurements [125]–[127].

Model	Resonance frequency (kHz)	Company	Tip radius (nm)	Tip Coating	Spring constant (N/m)
Scanasyst-Fluid+	150	Bruker	12	-	0.7
ASYELEC.02-R2	285	Asylum Research	25	Ti/Ir	42
HQ:NSC35/Pt (Tip c)	150	MikroMasch	<30	Pt	5.4

5.1.2   Tuning of the tip

The PFM measurement were performed with the Dual AC Resonance Tracking (DART) mode [69]. After engaging the surface and the contact was made, the cantilever was tuned to find the resonance frequency. The typical working frequencies for HQ:NSC35/Pt and ASYELEC.02-R2 tips are 800 kHz and 350 kHz respectively. One representative result of tuned resonance peak of HQ:NSC35/Pt tip is shown in Figure 5.2. Once the resonance frequency was found stabilized, we set the drive frequency close to this value. The two frequencies, f_1 and f_2 used in DART, had a separation of 10 kHz.
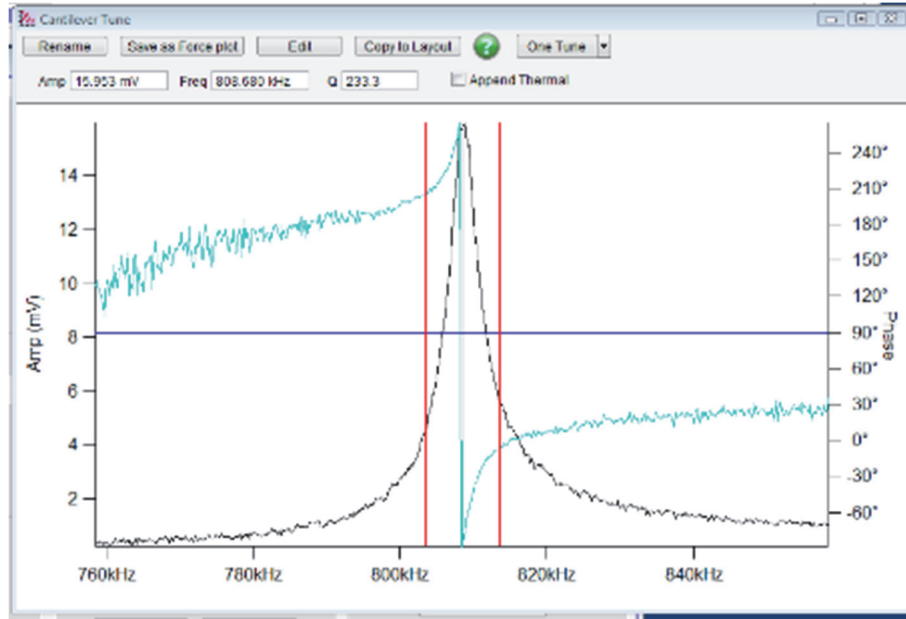
Figure 5.1 - Tuning of an HQ:NSC35/Pt AFM tip (k = 5.4 N/m) in air. The two red lines represent the two ac frequencies applied in DART mode.

Benefiting from resonance enhancement in DART mode, the cantilever response is essentially multiplied by the quality factor (Q) of the cantilever [69], [128].

$$A = d_{33}V_{ac}Q \tag{5.1}$$

The Q depends on tip's geometry and elasticity, as well as the local contact conditions on sample surface. Typical Q in our case ranges from 10 – 100. This implies that the measured piezoresponse amplitude is amplified by a factor of 10 – 100.

5.1.3   Domain patterns measurements

From the output signals from the PFM measurements, the phase shift of the vibration with respect to the excitation signal measures the direction of the polarization (up or down), and the amplitude measures the extent of local piezoelectric vibration. The general setting for performing the DART

measurements are: a setpoint of 0.3 - 0.5 V, a driver amplitude of 0.5 V or 1 V, a scan rate of 0.5 - 2 Hz and a scan resolution of 256×256 or 512×512.

In ferroelectrics, the polarization can be switched by applying an electric field that is higher than the coercive field. This can be done by scanning the AFM tip to which a DC voltage higher than coercive voltage is superimposed. The scanned area is then subject to the so formed DC field, and switches the polarization if not already pointing in the direction of the field. The scanned area under high voltage is thus poled by this procedure. In the ideal case, only one domain is left (0° domain). Two types of poling processes were performed. One type is poled with scanning a region with either positive or negative DC bias. The other type is poled with firstly scanning a region followed by scanning a smaller region inside with a opposite DC bias. The domain patterns are scanned afterwards to check the poling effects.

5.1.4 Hysteresis loop measurements

We measured the ferroelectric samples hysteresis loops with DART Switching Spectroscopy PFM (SS-PFM) [69]. For a local switching testing at a certain point, the AC frequency should be determined first by tuning the cantilever contact resonance frequency. Then the tip is applied with a mixed driving signal of a stepwise increasing DC electric bias with a superimposition of an AC driving signal, which has been set previously by tuning. A schematic view of the drive signal as a function of time is shown in Figure 5.2. The DC voltage should be higher than coercive voltage to pole the sample and switch the ferroelectric domains. The 'ON' and 'OFF' correspond to the status of DC signal. At 'ON' state, typical amplitude-voltage hysteresis loop is influenced by the interference between piezoelectric resonance and electrostatic effect [129]–[131]. Here we only considered the hysteresis loops recorded at off-state, when the DC voltage is removed.

In our work, the amplitude of DC voltage was set to be 6 ~ 9 V, the frequency of one cycle of hysteresis loop was 1 Hz and the period of individual pulse was 0.01 s. Most measurements were recorded for 4 cycles. A typical waveform of the input signal is shown in Figure 5.3.
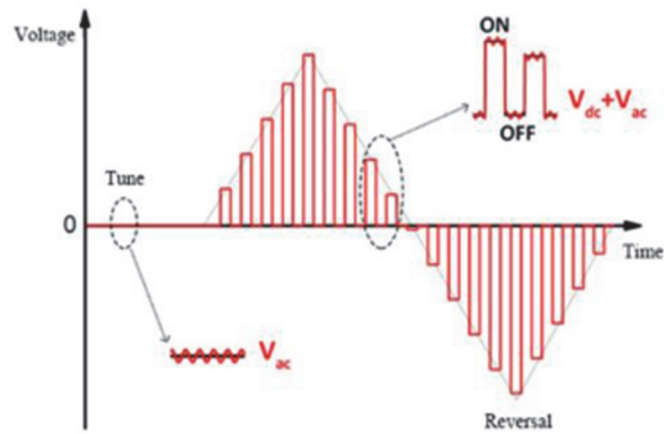
Figure 5.2 - Schematic diagram of driving signal loaded during SSPFM measurement. From Ref. [131]
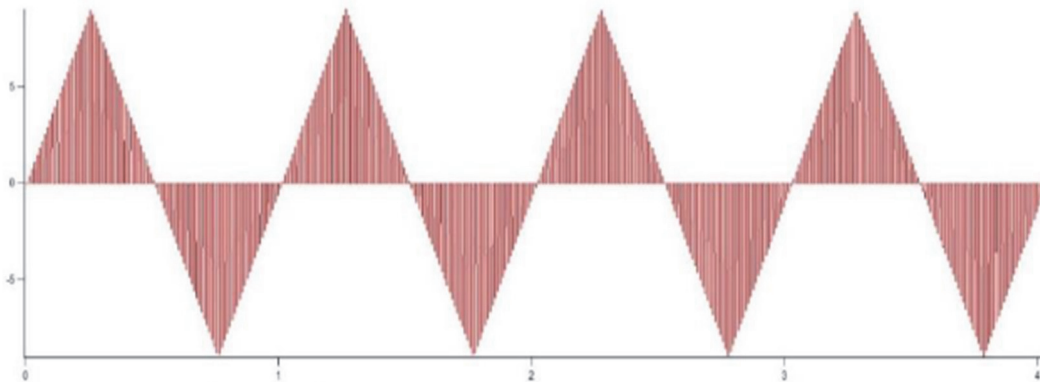
Figure 5.3 - The scan waveform for measuring in-field and remnant hysteresis loops for SS-PFM in this work.

5.2   Results and discussion

This section presents the PFM study results of PMN-PT 64/36 and PMN-PT 60/40 samples with plane films as well as patterned nanostructures.

- **22 nm PMN-PT 64/36 film on 20 nm SRO/Nb:STO**
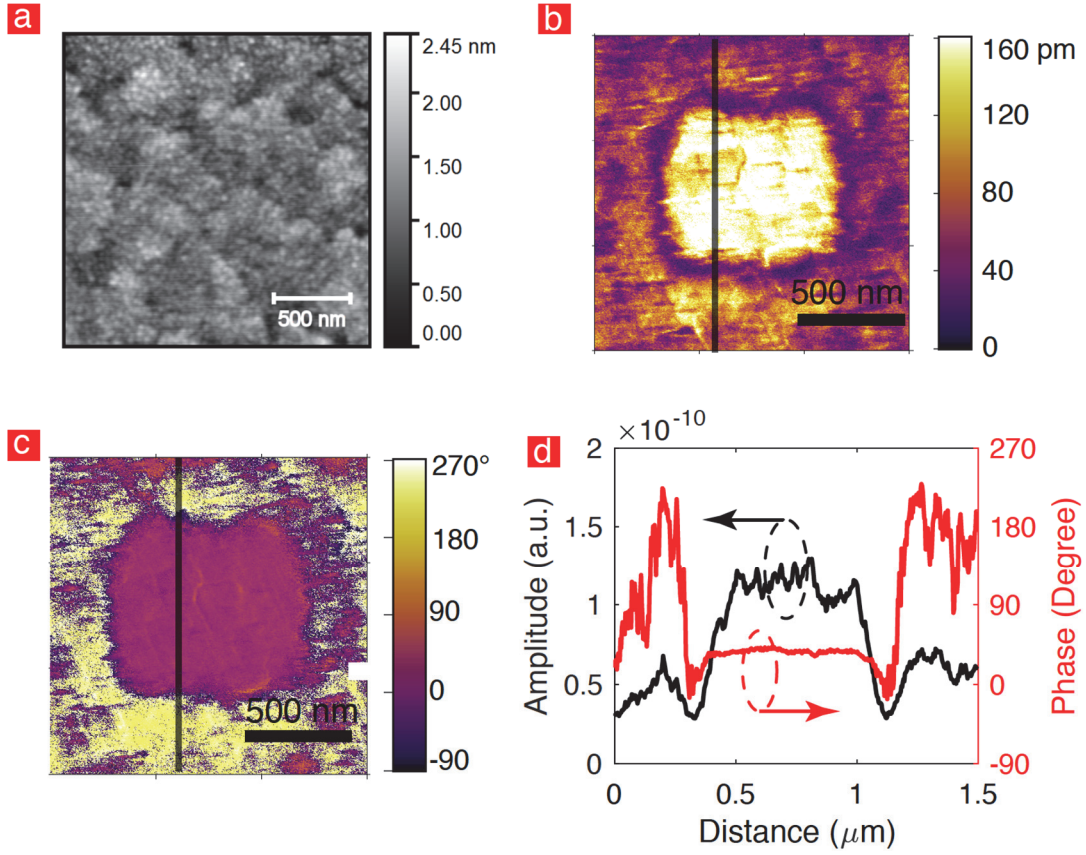
Figure 5.4 - PFM images for PMN-PT (22nm)/SrRuO$_3$(20nm) on Nb:SrTiO$_3$ substrate. The scanned area is 1.5×1.5 μm^2 large. (a) Topography image of the sample surface. After poling a square region of 500×500 nm^2 with -7 V DC bias, images of amplitude (b) and phase (c) were collected. (d) Scan along the line given in sub-figures b and c.

We first studied a film sample of 22 nm PMN-PT 64/36 on 20 nm SRO/Nb:STO. AFM topography image shown in Figure 5.4 (a) indicates that the film is grown in step-flow growth mode. The film showed an extremely low roughness, with a root mean square value of $\sim$ 76 pm in the 2×2 μm^2 scanned area. The as-deposit film of PMN-PT contains very small 180° domains. By scanning with a positive voltage, the scanned area did not show much differences in phase image. However, scanning with a negative voltage of -7 V, the scanned region (500×500 nm^2) was clearly visible in the

phase image. According to the phase and amplitude image, the poled region had quite a stable amplitude of 120 pm/V at a well-defined phase (there is an off-set of 30° form the zero-phase). Outside this region, the phase is rather unstable and the amplitude is small. Nevertheless, one can conclude that the as-deposit film exhibits in majority very small domains with down polarization (phase 30°+180°=210°). It is expected that with smaller thickness, the PMN-PT 64/36 film grown on SRO/Nb:STO has a preferred downwards self-polarization, which is though not complete. This is consistent with the experimental findings on PMN-PT 67/33 grown on Nb:STO or SrRuO$_3$, as reported in Ref. [132]. The lowest piezoelectric response occurs as expected at the boundaries between different polarized regions, i.e. at the "written" domain walls.
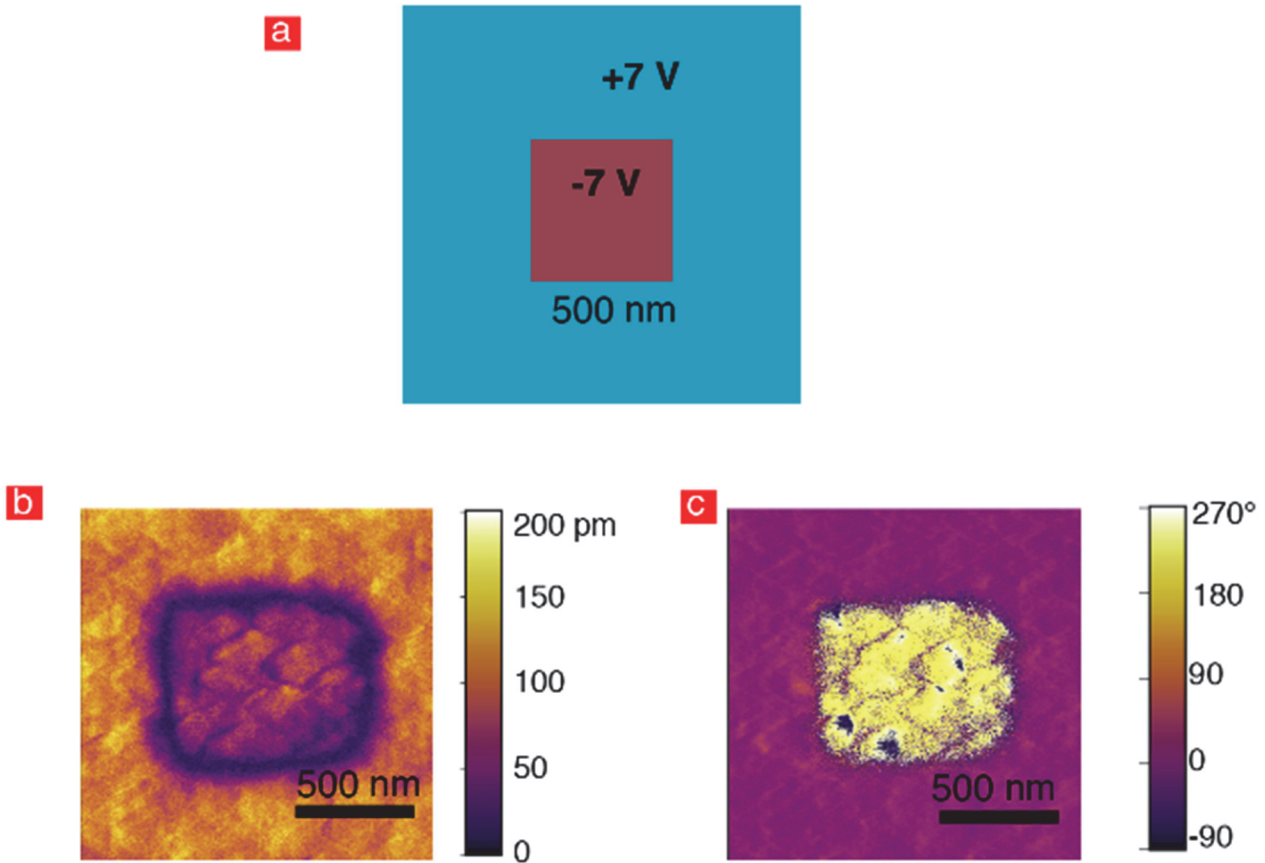
Figure 5.5 - PFM images for PMN-PT (22nm)/SrRuO$_3$(20nm) on SrTiO$_3$ substrate. (a) poling conditions. (b) amplitude image and (c) phase image.

We performed another poling process with a 'box in box' scan on the same sample. Firstly, a 2.0 × 2.0 µm^2 square area was scanned with +7 V DC and then a 500 × 500 nm^2 square was written with -

7 V DC bias in the center of previously poled region. A schematic view of the poling conditions and resulting PFM amplitude and phase images are shown in Figure 5.5. All the small domains with down polarization were switched by applying a +7 V DC bias. The results confirm that the polarization is switchable with both downwards and upwards electric fields.

- **square structure of 12 nm PMN-PT 64/36 and 6 nm SRO on Nb:STO**

We then tried to pole a patterned structure of 12 nm PMN-PT 64/36 on 20 nm SRO/Nb:STO square structure (~ 1 μm wide). The detailed condition for poling is shown Figure 5.5e. We first scanned a 1.7-μm-wide square region containing the PMN-PT square in center with 5 V. Then inside, a 600-nm-wide square region was scanned with periodically switched bias of -5 V, +5 V and -5 V. In the regions poled with negative and positive voltages, the PFM amplitude (Figure 5.6c) and (Figure 5.6d) phase images showed clear contrasts.
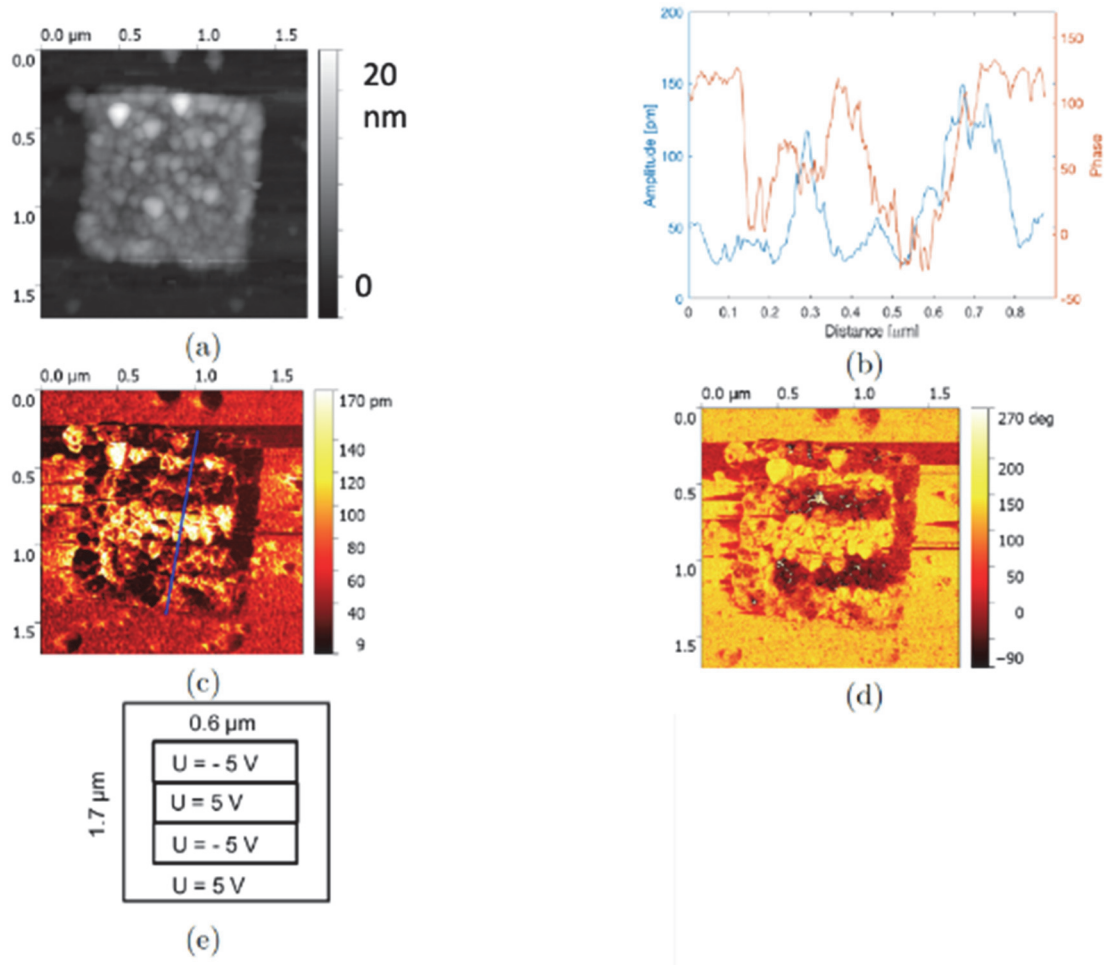
Figure 5.6 - AFM topography image of a square structure (~ 1.1 μm wide and ~ 12 nm high) of PMN-PT/SrRuO₃ heterostructure. After poling under conditions shown in (e), amplitude (c) and phase image (d) were recorded with profile along the lines shown in (b).

- **50 nm PMN-PT 60/40 on 20 nm SRO/Nb:STO**

The 50 nm PMN-PT 60/40 on 20 nm SRO/Nb:STO sample was annealed in oxygen at 550 °C during 10 minutes to reduce further oxygen vacancies. PFM images of this sample are shown in Figure 5.7. Regions of reduced amplitude in Figure 5.7b represent domain walls that separate ferroelectric domains of opposite polarizations. From the phase image in Figure 5.7c, it can be seen that, two distinct domain states with random bubble-like patterns have a phase difference of about 200°. To estimate

the irregular domain size, we can follow a few steps to extract a characteristic in-plane length Λ [133], [134], which is the domain periodicity. For regular domains, Λ equals to domain periodicity, while in non-periodic system, it reveals the distance between domains of the same polarization. The first step is to perform Fast Fourier transformation (FFT) of the raw PFM phase image using software Gwyddion (version 2.53) 2D-FFT module [135]. The obtained image is shown in Figure 5.7e. Next, we integrate the FFT data with respect to the azimuthal angle and symmetrize the results to have the profile shown in Figure 5.7f. As described in Ref. [133], the curve have two symmetric peaks that correspond to the domain separation in real space. From this method, a rough estimation of the characteristic length scales of 50 nm PMN-PT film was found to be 38 nm.
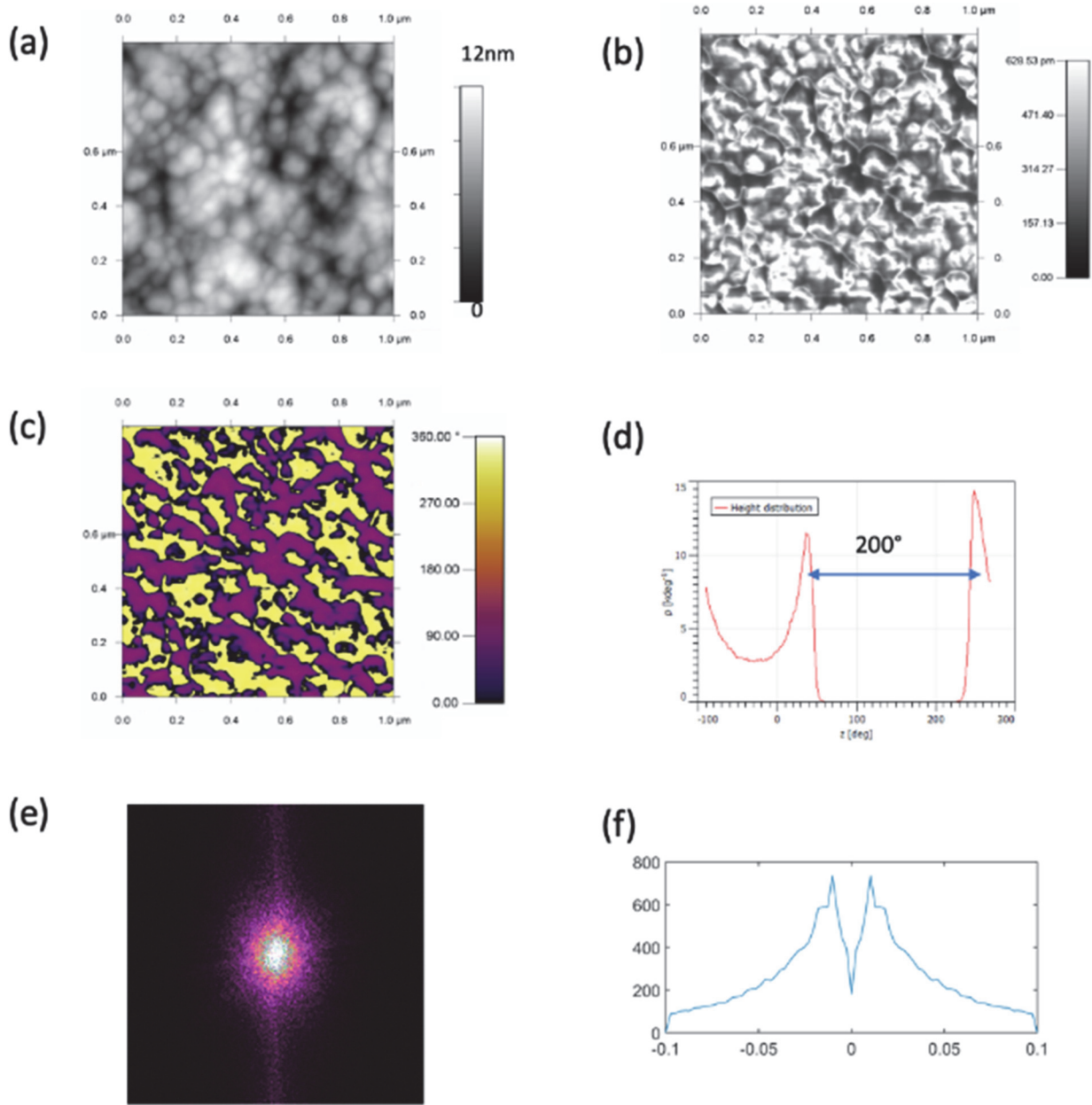
Figure 5.7 - (a) Topography image, (b) amplitude and (c) phase PFM image for a 50-nm-thick PMN-PT 60/40 film sample on 20 nm SRO grown on Nb:STO substrate. (d) represents the histogram of the phase in (c). (e) shows the FFT of the phase image. By integration of the FFT data with respect to the azimuthal angle and symmetrize the results, we obtained the profile shown in (f). The distance between the shoulders was used to estimate the domain size.
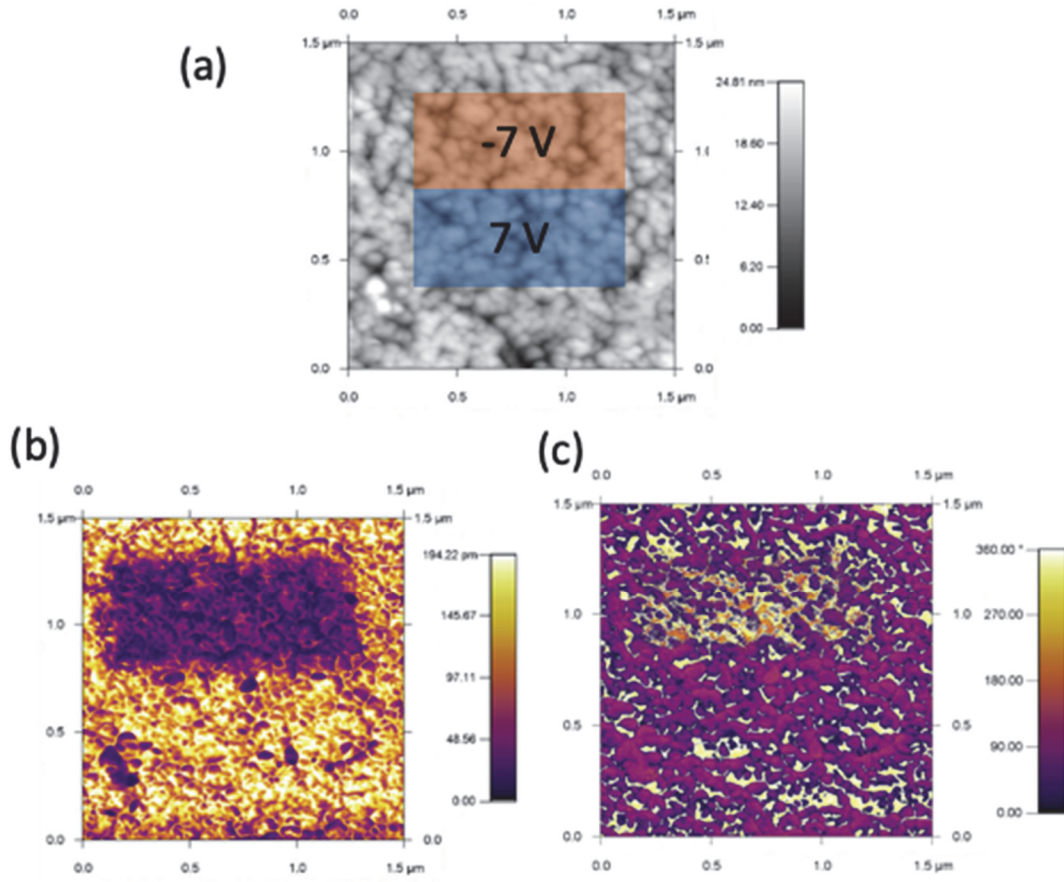
Figure 5.8 - Poling a 50-nm-thick PMN-PT 60/40 film sample on 20 nm SRO grown on Nb:STO STO substrate with PFM. (a) topography image with poling condition. (b) amplitude and (c) phase PFM image.

The poling results of the same sample were shown in Figure 5.8. The results indicated that the PMN-PT film can be switched under -7 V DC bias on the tip, while certain amount of domains were not completely switched. After switching to upward polarization, the region showed a weaker piezoresponse.

- **20 nm PMN-PT 60/40 nanostructures on 20 nm SRO/Nb:STO**

The 20 nm PMN-PT 60/40 nanostructures on 20 nm SRO/Nb:STO sample were annealed under the same conditions as mentioned before (in oxygen at 550 °C during 10 minutes).

Figure 5.9 shows the first measurement results of PFM images from a nano-island, without poling with DC bias. As seen from the phase image in Figure 5.9c, the island consisted two parts in about the same size with opposite polarizations.
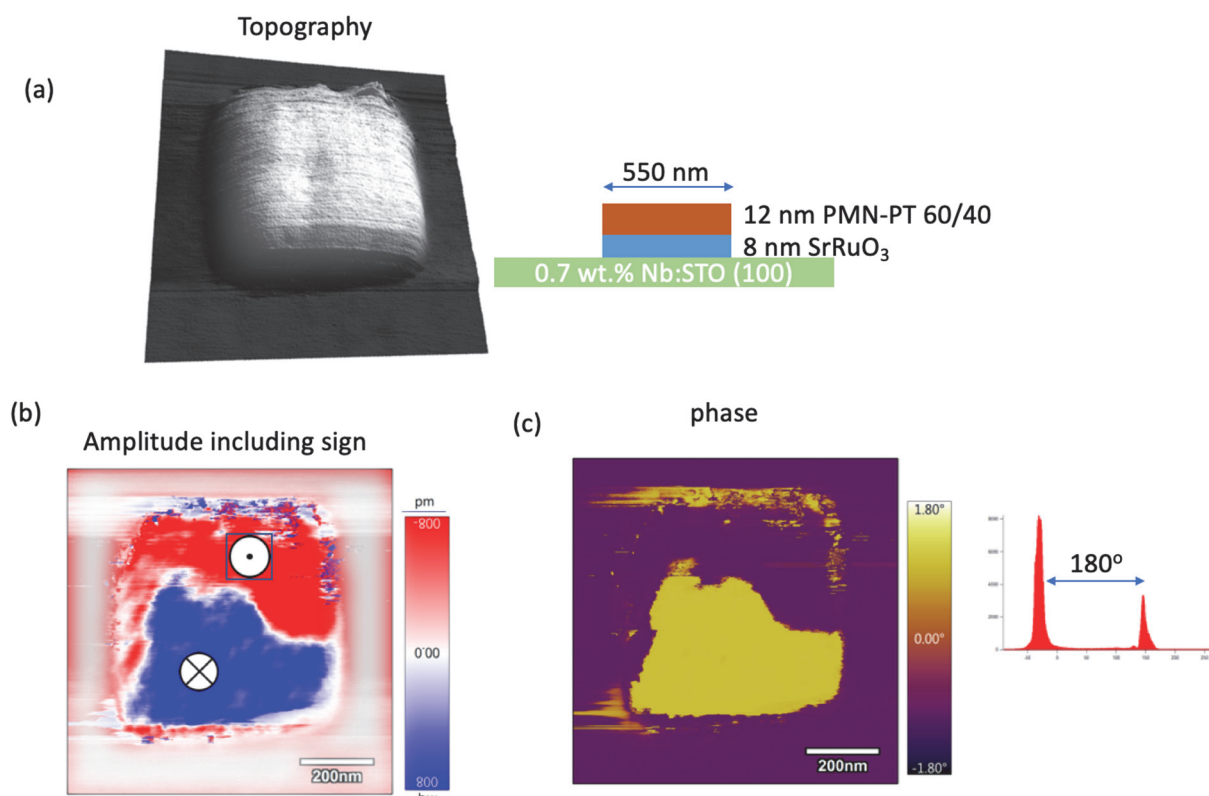
Figure 5.9 - AFM topography image of an annealed nano-island of 0.60PMN-0.40PT (12nm) /SrRuO$_3$ (8nm)/ SrTiO$_3$ heterostructures. The size is around 550 nm. Out-of-plane PFM amplitude image (b) and phase image (c).

As we kept scanning the same island up and down serval times with the same settings (V_{ac} = 1V, f_0 = 780 kHz, scan rate was 0.5 Hz and resolution was 512 × 512 lines. Each scan took about 8 minutes.), we found that the region with initial upwards polarization gradually turned to downwards polarization. Even without the effect from an external applied DC field, this nano-island finally completely switched to the downwards polarization after it was scanned for 7 times in about 1 hour. This is likely due to the built-in electric field for PMN-PT/SRO which stabilizes the downward direction, thus induces downward switching when the domains are shaken by an AC field.
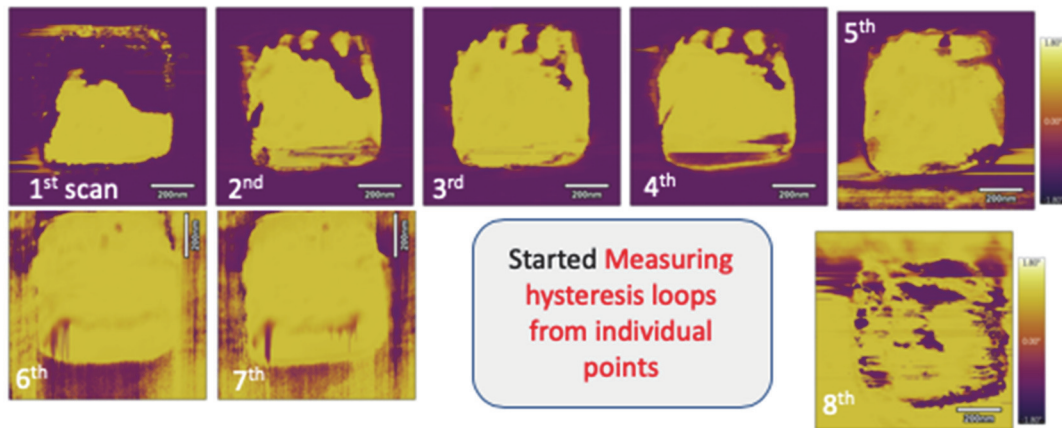
Figure 5.10 - Evolution PFM phase image of with continuous scanning for several times in about 1hour. After the 7th scan, loop hysteresis loops were measured at individual points. After we came back to the same region in 8th scan, small regions around these points were switched (by a negative DC bias). Nano-island had a size around 550 nm with 0.60PMN-0.40PT (12nm) /SrRuO$_3$ (8nm)/ SrTiO$_3$ heterostructures.
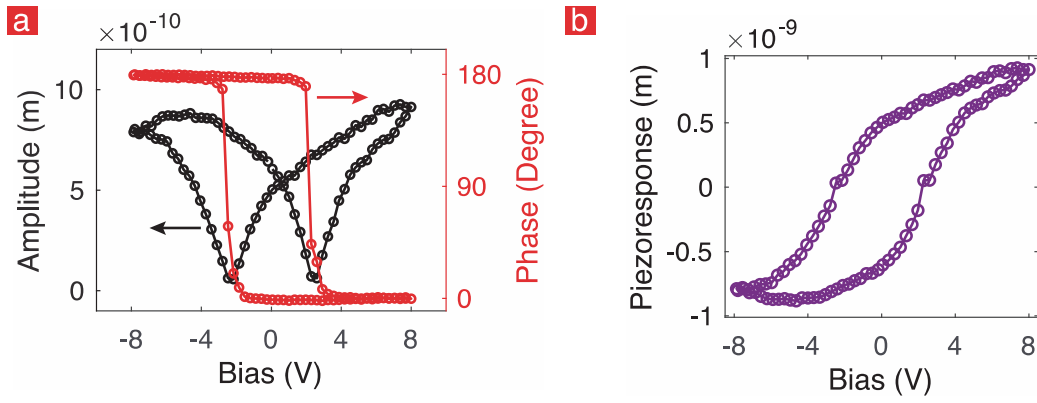
Figure 5.11 - (a) Measured phase and amplitude response loop as a function of the applied DC bias by PFM. (b) The piezoresponse from a 550 nm wide dot of 0.60PMN - 0.40PT (12nm)/SrRuO3(8nm).
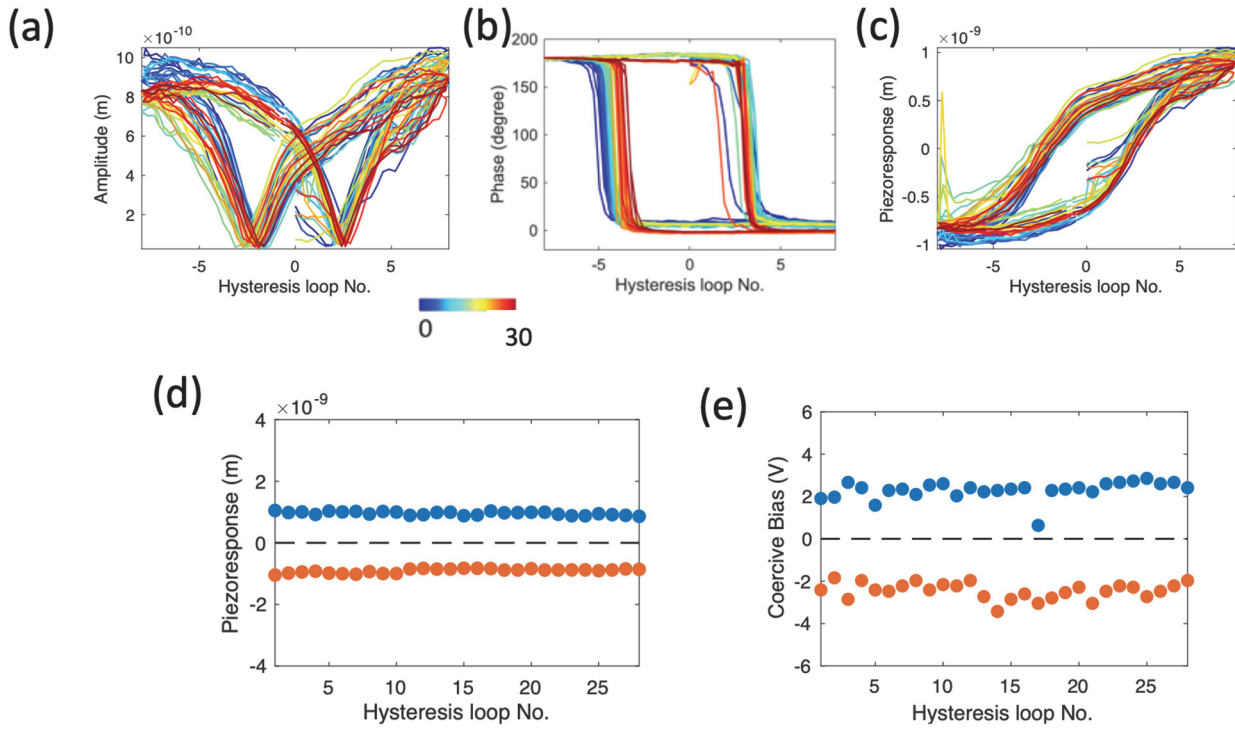
Figure 5.12 - Measured amplitude (a) and phase response (b) loop; (c) derived piezoresponse loop; extracted coercive voltages (d) and peak piezoresponse (e) for 30 cycles from a point on a 550 nm wide square of 0.60PMN - 0.40PT (12nm)/SrRuO3(8nm)/STO.

Hysteresis loop measurements were performed on this individual nanoplates, after the self-polarization turned stable as shown in Figure 5.10. Typical results from one point are shown in Figure 5.11. The measured piezoresponse was rather stable from the results recorded over 30 cycles, shown in Figure 5.12. The amplitudes measured with the DART method are amplified by a factor of 10 to 100 [136]. The amplitudes observed as high as 1 nm/V would this correspond to response of 10 to 150 pm/V for the thickness mode piezoelectric effect. The absolute value of negative coercive voltage (~ 2.6V) is slightly higher than the positive coercive voltage (~ 2.4V).

We performed a poling process on another nano-island in similar size. Figure. 5.13 shows a poled region written into a nano platelet. Some features in the amplitude image indicate domain patterns, having the same phase in the response, as it can be with domains having a polarization relation enclosing an angle of 90° or less, as e.g. *a/c* domain patterns in tetragonal {100} films. One can identify amplitude hills and valleys running parallel or orthogonal to the in-plane crystallographic directions, which would correspond to a tetragonal symmetry. At some places one can identify features including angles of 120°, corresponding to a rhombohedral symmetry. Typical dimensions of these features are a width of 10 to 15 nm, and a length of 20 to 30 nm. These dimensions correspond to 0.5 to 1.5 times the PMN-PT film thickness. These domain patterns do not have a larger coherence. This is rather expected for a material that is close to a relaxor phase. Lebeau and coworkers have shown that in PMN single crystals there are chemically ordered regions (COR) of the typically 3 nm diameter. Although the cation diffusion during thin film growth is mainly on the surface, and not in the bulk (see ref. [137]), one can assume that these CORs exist certainly as well, possibly even more pronounced and larger. This would explain that films close to the morphotropic phase boundary may exhibit both symmetries, even when nominally on the tetragonal side like PMN-PT 60/40.
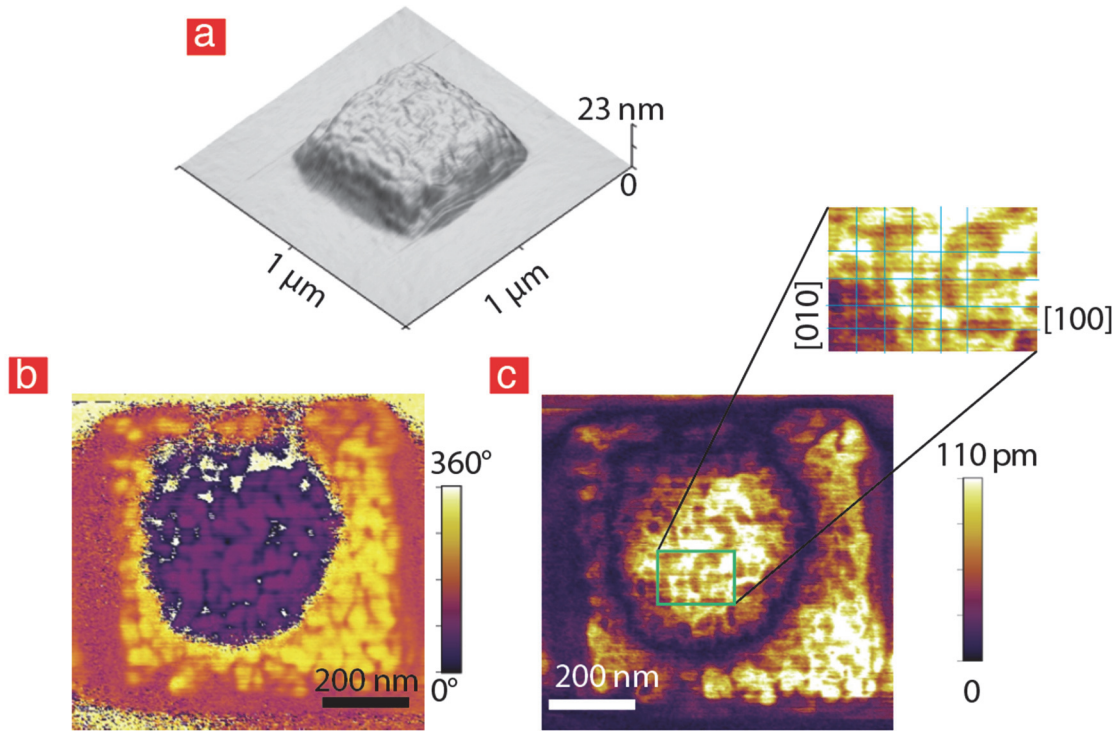
Figure 5.13 - (a) AFM topography image of a nano-island of 0.60PMN-0.40PT(12nm) /SrRuO$_3$(8nm)/ SrTiO$_3$ heterostructures, which were annealed in oxygen prior to measurements. The size is around 550 nm. Out-of-plane PFM amplitude image (b) and phase image (c) of the nano-island after being poled with -7 V DC bias written within a 250 × 250 nm^2 square in the centre of the nano-island.

5.3   Summary and conclusions

Ferroelectric response of the developed PMN-PT films and nanostructures was characterized by piezoresponse microscopy. The nanostructures were individually addressable and found to be still ferroelectric. With a thickness below about 20 nm, the as-deposit PMN-PT film and nanostructures on SRO/Nb:STO tend to be self-polarized with downwards direction. Plain film areas and nano features were consecutively switched by a negative bias applied to the tip. Hysteresis loop measurements on a 12-nm-thick PMN-PT 60/40 nanostructure revealed high piezoresponse, roughly in a range 10-150

pm/V. The piezoresponse was stable during a large number of recorded loops. After poling annealed PMN-PT 60/40 nanostructure by external DC bias applied to the AFM tip, domain features corresponding both rhombohedral and tetragonal symmetry were observed. Logically, the chemically ordered regions have some spread in composition and may manifest with tetragonal and rhombohedral symmetry. The observations confirm the successful growth of high quality ferroelectric PMN-PT films around the MPB. The developed nanostructuration process maintains functional ferroelectric properties. The domain patterns in the un-poled film exhibit dimension of around the film thickness (12 nm). Polar nanoregions of a pure PMN phase are expected to be rather in the range of 5 nm. It would be interesting to learn whether PNRs are still present at the MPB composition, how they would manifest in an ultrathin film, and how they would influence domains.

Chapter 6   Summary and outlook

6.1   Summary

The goal of this thesis was to study the ferroelectricity of (1-x)[Pb(Mg1/3Nb2/3)O3]-x[PbTiO3] (PMN-PT) nanostructures. At a composition around the morphotropic phase boundary (x=0.33), the perovskite material PMN – PT provides an extremely high piezoelectric strain under an applied electric field. This remarkable behavior makes it of great interest for the application in piezo-electronic transistors (PET).

The investigations in this thesis were carried out in serval stages: growing high quality epitaxial PMN-PT films, fabrication of damage-free nanostructures and characterization of their ferroelectric properties by PFM.

In the first step, PMN-PT films were epitaxially grown on $SrRuO_3$-buffered $SrTiO_3$ substrates by pulsed laser deposition (PLD). We have optimized the growth conditions to obtain phase-pure perovskite (001)-oriented films on prepared flat $SrTiO_3$ substrates with TiO_2-termination. It was found that the deposition temperature played the most important role for phase formation in PMN-PT layer. The optimal deposition T for PMN-PT was 575°C, avoiding any pyrochlore phase. We improved the surface roughness to ~100 pm by increasing the O_2 pressure from 0.25 mbar to 0.50 mbar. By adding 5 mol.% PbO excess to the stoichiometric targets, the lead content increased by 7% in the resulting film. From one representative sample of a 50 nm thick film of PMN-PT 60/40 on 20 nm $SrRuO_3$, reciprocal space maps (RSMs) produced by high resolution X-ray diffraction revealed that $SrRuO_3$ was grown coherently on the $SrTiO_3$ substrate, while PMN-PT was structurally relaxed with a = 4.001 Å and c = 4.031 Å. The a-values is practically identical to literature values of monocrystals.

Next, we developed a novel lift-off process for patterning PMN-PT into nanostructures. The process can be adapted to pattern one layer only or to pattern heterostructures of multilayers (such as PMN-PT/SRO) in single lift-off step. The bilayer lift-off mask consisted of high-resolution electron-beam resist hydrogen silsesquioxane (HSQ) on top of amorphous aluminium oxide (AlO_x). After exposure to define precise patterns by means of high energy e-beam lithography, HSQ was developed in

TMAH. In the same step, AlO$_x$ was etched isotropically in TMAH, forming an underetch in AlO$_x$. The lateral underetch has a width of about the same as the AlO$_x$ layer thickness. The HSQ/AlO$_x$ bilayer mask, with exposed SrTiO$_3$ substrate surface, served as a mold for PMN-PT growth. The removal of the bilayer mask was performed in 6M NaOH aqueous solution. The film structures grown inside the openings follows the shape of the mold, producing the obtuse angle at the edge of the nanostructure. The thickness of the nanostructures varied with the width of the openings, and is less than the film thickness. The minimum features fabricated with this method have a lateral size ~ 70 nm with a film thickness of 12 nm. In order to predict the thickness decrease, we considered the fact that the flux arriving from the opening has is distributed on a larger area. The derived value from our model agreed well with the measured thickness. HRXRD measurements was performed on one sample with PMN-PT 64/36 after lift-off. Although focusing on an area containing both plane film and discrete nanostructures, we observed only pure perovskite phase with (00l) reflections in PMN-PT. The lattice constants were derived from x-ray reciprocal space mapping as $a = 3.985$ Å and $c = 4.046$ Å. Apparently the thinner film is less relaxed. Further studies with high resolution synchrotron XRD with beam spot size in about micron size would give more insights of the PMN-PT nanostructure. Of particular interest would to investigate domain patterns in relation to chemically ordered regions.

Finally, the investigations of ferroelectric properties of PMN-PT samples produced a number of interesting findings. The samples of PMN-PT are in composition of 60/40 and 66/34 grown on SRO/Nb:STO. Both plane film and nanostructures of PMN-PT with a thickness under 20nm preferred a downwards polarization due to a built-in electric field. Extended PMN-PT films show strong self-poling, leading to a more homogeneous phase and amplitude contrast. The arrays of nanodots and nano line structures exhibit ferroelectric properties. The features can be poled in up and down direction. The piezoelectric response cannot be quantified precisely with the applied DART method. However, it is certainly larger than 10 pm/V, and may reach 100 pm/V. The patterned PMN-PT plate exhibited good ferroelectric behavior, in as much the polarization could be defined by the tip, complete regions could be switched, and rewritten in films that are only 12 nm thick. The coercive voltage amounted to about 4 V, and the piezoelectric thickness mode response was measured in the range of 10 to 150 pm/V. This result shows firstly that the structure is piezoelectric as required for the application in a piezoelectric transducer for logic applications. Secondly, the elements can be poled with low voltages if the auto-polarization induced by process and interfaces is not yet sufficient.

The overall achieved results constitute a step towards nanoscale engineering of ferroelectrics for the advancement of efficient electromechanical device applications.

6.2   Outlook

A few aspects can be explored to extend the studies related to this thesis.

The usage of HSQ/AlO$_x$ bilayer mask with undercut profile combines well for an efficient lift-off technique that can be applied at higher temperatures (600 °C). However, it inevitably limits the resolution of this method. The minimum PMN-PT features we achieved have a size of ~70 nm, grown from openings of 40 nm patterns in HSQ. By reducing the thickness of AlO$_x$, we expect less underetch, leading to smaller lateral size of the mold, thus the nanostructures grown inside it. This was indeed consistent with what we found when reducing the AlO$_x$ thickness from 50 nm to 30 nm. But the thickness of AlO$_x$ cannot be too small. Otherwise, if the nanostructure thickness exceeds the AlO$_x$ layer thickness, the lift-off process would be difficult. Moreover, the HSQ will react with PMN-PT in the form of PbO interdiffusion.
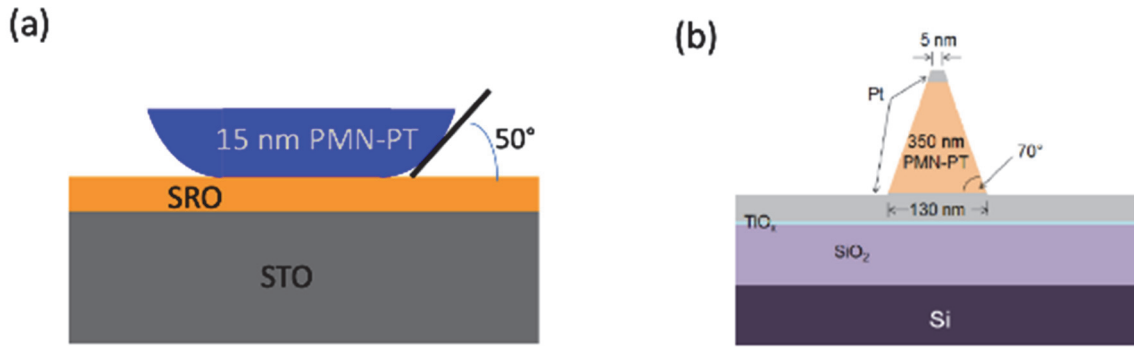
Figure 6.1 - (a) schematic view of the cross section of nanostructure fabricated by lift-off process. Compared with that of a nanostructure obtained by dry etch process (b), from Ref. [138].

As we observed from TEM images of the nanostructure cross-section, the PMN-PT/SrRuO$_3$ heterostructures formed an obtuse angle $\sim 120°$ at the edge of the nanostructure. In contrast, the sidewall of dry-etched patterns have an acute angle $\sim 70°$, which is often undesirable. In extreme case, the shrinkage of size in top could make the top electrode pinch off [138].

The structural profile at the edge may be interesting for studying size effect in ferroelectrics. Size effect have attracted a lot of interest. Typically, this was measured on ferroelectric structures of different sizes. By reducing the lateral size, higher aspect ratio is obtained, leading to a higher degree of declamping. The reduced stress constraints due to declamping provide a boost in piezoresponse, as have been reported by other researchers [138]–[140]. In our case, the thickness of the obtained nanostructures is 7 nm ~25 nm, which is too small compared with width (70 nm up). Thus, there is not much variation of degree of declamping. But our developed process can be adapted to pattern ferroelectric perovskite structures with larger thickness and aspect ratio ~ 1. Nevertheless, the edge of lift-off fabricated structures, is even partially suspended. The strain state must differ a lot between the free edge and the strained central region. A stronger local piezoresponse is expected at the edge. This could be possibly proved by using careful PFM measurements with more quantitative evaluation. The DART technique of PFM, although enhance the weak piezo response, have an amplifying factor Q that strongly depends on local conditions. Alternatively, arrays of dots, planarized by a polymer, and equipped with a reflecting layer could be analyzed by Double Beam Laser Interferometer (DBLI). However, this would require quite a complex device fabrication considering all the electrode connections.
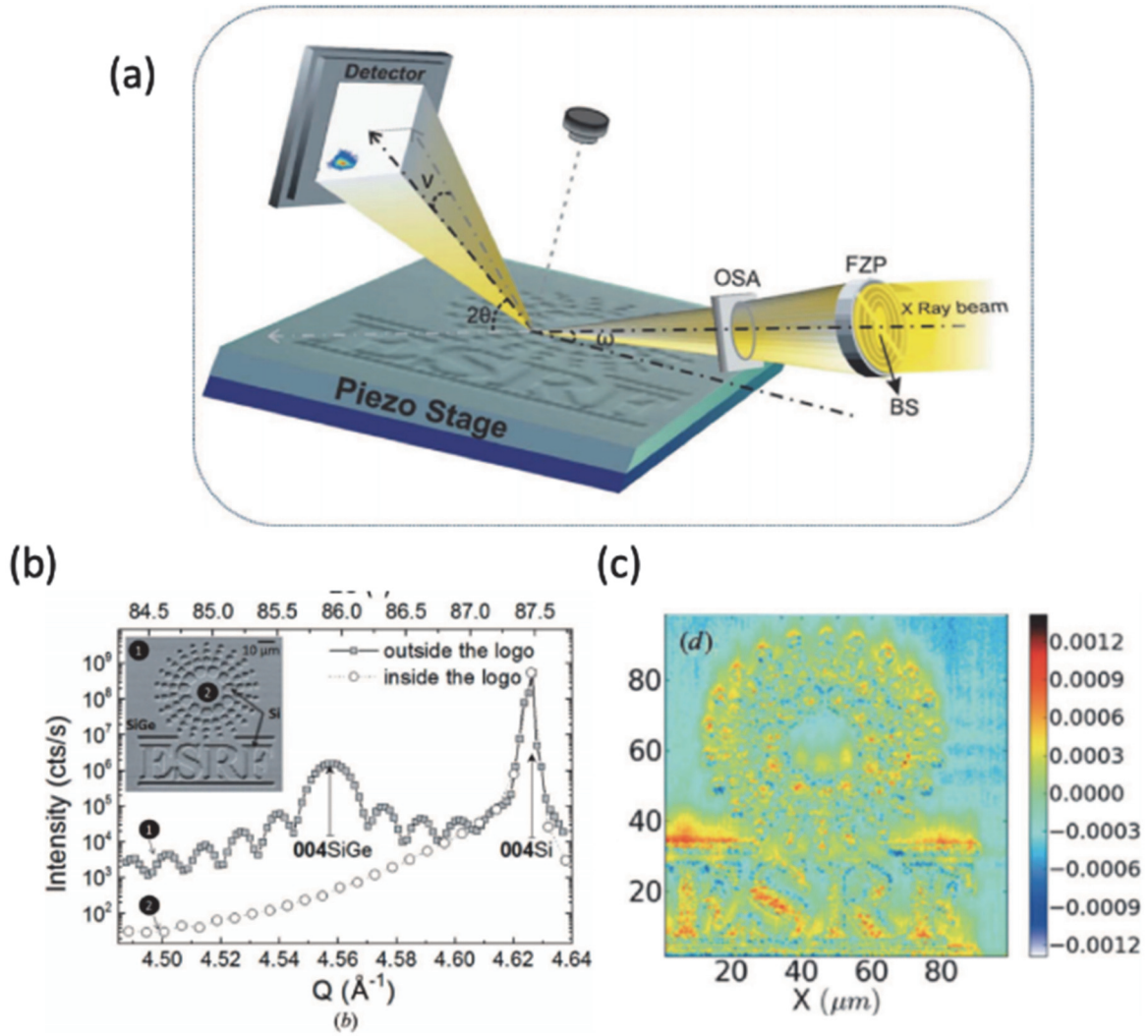
Figure 6.2 - (a) Schematic overview of the experimental setup of scanning X-ray diffraction technique using ID01 beamline in ESRF. (b) theta-2theta scans showing inside and outside of the a Si0.8Ge0.2 structure on Si substrate. (c) Map of local strain extracted from RSMs results. Adapted from Ref. [141].

High resolution synchrotron x-ray diffraction would definitely provide in-depth investigations of the domain structures. First, a very high intensities of X-ray radiation, for example from a synchrotron source, is required for study the nanostructures. It is evident as we observed a much lower intensity of PMN-PT peak on a nanostructured sample than that from a plain film sample. Secondly, with a focused beam, we could directly study insights of nanostructures in a small region, or one individual nanostructure or even locally inside the one nanostructure. For example, the ID01[142] beamline of

The European Synchrotron Radiation Facility (ESRF) provides a beam focus area of typically 65.0 × 56.0 nm^2, with the best record of 30 × 30 nm^2. The focused beam can be translated on a sample at different position (*x, y*) by moving a piezo stage. At each investigated small region on the sample, 3D reciprocal scan maps (RSMs) can be recorded by tilting another stage to reach any Bragg reflection. This technique, called Scanning X-ray diffraction microscopy, then give the diffraction intensities as a function of (Q_x, Q_y, Q_z, *x, y*), allowing comprehensive study of local structure. Figure 6.2 shows a schematic view of the setup and one example of experimental results of extracted strain maps in a 100 × 100 μm^2 area [141].

With electron beam lithography technique, complex shape of the patterns can be defined. Different shapes rather than island and lines of nanostructures can be fabricated subsequently with lift-off process. We fabricated ring structures with width ~200 nm an inner diameter 200 - 400 nm. The rings were proved to be ferroelectric and can be poled up and down, as shown in Figure 6.3. This might inspire more thoughts on applications of ferroelectrics in nano devices.
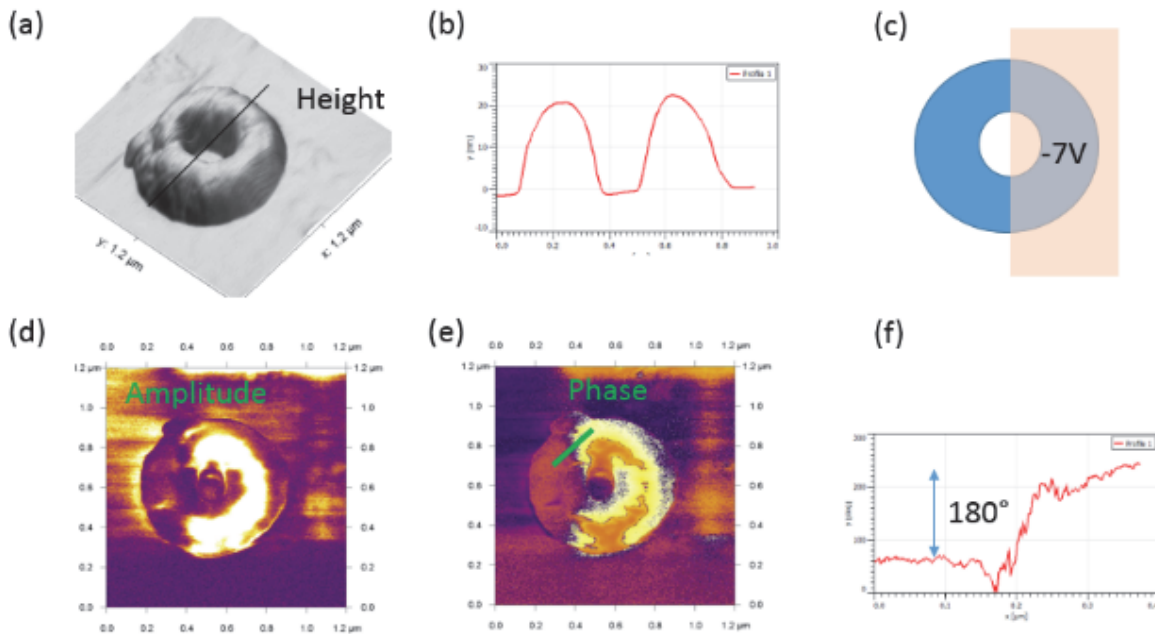
Figure 6.3 - PFM measurements on one ferroelectric nano ring structure of 13 nm PMN-PT 60/40 and 8 nm SrRuO$_3$ on Nb:SrTiO$_3$. (a). 3D AFM image. (b) height profile along a line. (c) the right half of the ring was poled with -7 V (d) amplitude and (e) phase image after poling. The profile in (f) indicates that the successfully poled region had a phase shift ~180°.

We only studied the epitaxial PMN-PT grown on SrRuO$_3$ buffered STO, having a lattice mismatch ~ 2.2% between SRO and PMN-PT. By using a different substrates, like DyScO$_3$, or even by introducing a interfacial layer of Pb(Zr$_{(1-x)}$Ti$_x$)O$_3$ interfacial layer compositions (x = 0.2 - 0.8), a smaller mismatch is expected. PMN-PT can be also grown on Si substrates, with a SrTiO$_3$ buffer layer. The lift-off technique could be used to pattern damage-free SRO/PMN-PT/SRO sandwich structures. Silicon substrate could be isotropically etched in selective area by KOH solution in the next step, releasing free-standing structures of SRO/PMN-PT/SRO [143]. Devices containing such structures with PMN-PT as active material could have wide applications in MEMS and NEMS for sensing or actuation.

Appendix: Fabrication of PMN-PT nanostructures Runcard

Project : PMN-PT lift-off

Operator : Xiao Di

Created : 2018.01.18 **Last revision** : 2019.05.10

Substrates : Nb:SrTiO3 <100> 5 x 5mm, 500um in thickness, 0.7 wt.% doping

Step N°	Description	Work-	Equipment	Program / Parameters	Target
0	**Substrate Preparation**				
0.1	IPA clean	PM lab	ultrasonic bath		30 mins
0.2	BHF etch	PM lab		NH4F : HF = 7:1	1 min
0.3	Clean	PM lab	IPA and DI		
0.3	Anneal	PM lab	oven	Pl1 = 1100°C, Pd = 3h	
0.4	Check	PM lab	AFM Cypher		
1	**ALD AlOx**				
1.1	ALD AlOx	CMi Z4	ALD	Recipe: Al2O3 - 30 nm	30 nm
2	**EBEAM LITHOGRAPHY**				
2.1	Pre bake	CMi Z7	hot plate		5 mins 150°C
2.2	HSQ 1541-002	CMi Z7	spin coater	5000 rpm	35 nm
2.3	load on stage	CMi Z7	stage 16, mi-	load sample on stage, rec-	
2.4	ebeam exposure	CMi Z7	Vistec	20180123_5mm.job	dose 800 - 1000
2.5	develop and etch	CMi Z7	wetbench	TMAH 25%	16 mins
2.6	Inspection	CMi Z7	optical micro-	check after etch	
2.7	Check	CMi Z1	LEO 1550		
2.8	check	PM lab	AFM Cypher	check structure	
3	**PLD**				
3.1	preablation	PM lab	PLD	5 Hz, 2 mins	
3.2	SRO	PM lab	PLD	625°C, 20 mins, 8 sccm	20 nm
3.3	PMN-PT	PM lab	PLD	575°C, 42 mins, 70 sccm	50 nm
3.4	Cool down	PM lab	PLD	100 sccm O2	20°C
3.5	Check	CIME	SEM Gemini	surface morphology	
3.6	Check	PM lab	XRD	theta-2theta	perovskite, (00l)
3.7	Check	PM lab	AFM Cypher		
4	**Lift-off**				
4.1	Lift-off	PM lab	ultrasonic bath	4M NaOH for 5 hours	
4.2	Clean	PM lab	IPA and DI		
4.2	Check	CIME	SEM Gemini		

Bibliography:

[1]   R. H. Dennard, F. H. Gaensslen, V. L. Rideout, E. Bassous, and A. R. LeBlanc, "Design of ion-implanted MOSFET's with very small physical dimensions," *IEEE Journal of Solid-State Circuits*, vol. 9, no. 5, pp. 256–268, Oct. 1974.

[2]   W. Haensch *et al.*, "Silicon CMOS devices beyond scaling," *IBM Journal of Research and Development*, vol. 50, no. 4.5, pp. 339–361, Jul. 2006.

[3]   T. N. Theis and P. M. Solomon, "It's Time to Reinvent the Transistor!," *Science*, vol. 327, no. 5973, pp. 1600–1601, Mar. 2010.

[4]   P. M. Solomon *et al.*, "Pathway to the Piezoelectronic Transduction Logic Device," *Nano Lett.*, vol. 15, no. 4, pp. 2391–2395, Apr. 2015.

[5]   A. M. Ionescu and H. Riel, "Tunnel field-effect transistors as energy-efficient electronic switches," *Nature*, vol. 479, no. 7373, pp. 329–337, Nov. 2011.

[6]   W. Hansch, C. Fink, J. Schulze, and I. Eisele, "A vertical MOS-gated Esaki tunneling transistor in silicon," *Thin Solid Films*, vol. 369, no. 1, pp. 387–389, Jul. 2000.

[7]   W. Y. Choi, B. Park, J. D. Lee, and T. K. Liu, "Tunneling Field-Effect Transistors (TFETs) With Subthreshold Swing (SS) Less Than 60 mV/dec," *IEEE Electron Device Letters*, vol. 28, no. 8, pp. 743–745, Aug. 2007.

[8]   S. Datta and B. Das, "Electronic analog of the electro-optic modulator," *Applied Physics Letters*, vol. 56, no. 7, pp. 665–667, Feb. 1990.

[9]   T. J. K. Liu, D. Markovic, V. Stojanovic, and E. Alon, "The relay reborn," *IEEE Spectrum*, vol. 49, no. 4, pp. 40–43, Apr. 2012.

[10]   D. Newns, B. Elmegreen, X. H. Liu, and G. Martyna, "A low-voltage high-speed electronic switch based on piezoelectric transduction," *Journal of Applied Physics*, vol. 111, no. 8, p. 084509, Apr. 2012.

[11]   D. M. Newns *et al.*, "The PiezoElectronic Switch: A Path to High Speed, Low Energy Electronics," *Advances in Science and Technology*, vol. 90, pp. 93–102, Oct. 2014.

[12]   J. B. Chang *et al.*, "First realization of the piezoelectronic stress-based transduction device," *Nanotechnology*, vol. 26, no. 37, p. 375201, Sep. 2015.

[13] D. M. Newns, B. G. Elmegreen, X.-H. Liu, and G. J. Martyna, "High Response Piezoelectric and Piezoresistive Materials for Fast, Low Voltage Switching: Simulation and Theory of Transduction Physics at the Nanometer-Scale," *Adv. Mater.*, vol. 24, no. 27, pp. 3672–3677, Jul. 2012.

[14] N. Domingo *et al.*, "Giant reversible nanoscale piezoresistance at room temperature in Sr2IrO4 thin films," *Nanoscale*, vol. 7, no. 8, pp. 3453–3459, Feb. 2015.

[15] R. R. Keech, "Dimensional Scaling of Perovskite Ferroelectric Thin Films," 2016.

[16] C. H. Ahn, K. M. Rabe, and J.-M. Triscone, "Ferroelectricity at the Nanoscale: Local Polarization in Oxide Thin Films and Heterostructures," *Science*, vol. 303, no. 5657, pp. 488–491, Jan. 2004.

[17] P. Muralt, "Ferroelectric thin films for micro-sensors and actuators: a review," *J. Micromech. Microeng.*, vol. 10, no. 2, p. 136, 2000.

[18] P. Muralt, "Recent Progress in Materials Issues for Piezoelectric MEMS," *Journal of the American Ceramic Society*, vol. 91, no. 5, pp. 1385–1396, May 2008.

[19] S.-H. Baek, M. S. Rzchowski, and V. A. Aksyuk, "Giant piezoelectricity in PMN-PT thin films: Beyond PZT," *MRS Bulletin*, vol. 37, no. 11, pp. 1022–1029, Nov. 2012.

[20] P. Muralt, R. G. Polcawich, and S. Trolier-McKinstry, "Piezoelectric Thin Films for Sensors, Actuators, and Energy Harvesting," *MRS Bulletin*, vol. 34, no. 09, pp. 658–664, Sep. 2009.

[21] S. Trolier-McKinstry and P. Muralt, "Thin Film Piezoelectrics for MEMS," *Journal of Electroceramics*, vol. 12, no. 1–2, pp. 7–17, Jan. 2004.

[22] "Orienting Ferroelectric Films."

[23] D. Akai, M. Yokawa, K. Hirabayashi, K. Matsushita, K. Sawada, and M. Ishida, "Ferroelectric properties of sol-gel delivered epitaxial Pb(Zrx,Ti1-x)O3 thin films on Si using epitaxial r-Al2O3 Layers," *Applied Physics Letters*, vol. 86, no. 20, p. 202906, May 2005.

[24] S. E. Park and T.R. Shrout, "Ultrahigh strain and piezoelectric behavior in relaxor based ferroelectric single crystals," *J.Appl.Phys.*, vol. 82, pp. 1804–1811, 1998.

[25] D. Damjanovic, "A morphotropic phase boundary system based on polarization rotation and polarization extension," *Appl.Phys.Lett.*, vol. 97, p. 062906, 2010.

[26] F. Li *et al.*, "The origin of ultrahigh piezoelectricity in relaxor-ferroelectric solid solution crystals," *nature communications*, vol. 7, p. 3807, 2016.

[27] P. R. Willmott and J. R. Huber, "Pulsed laser vaporization and deposition," *Rev. Mod. Phys.*, vol. 72, no. 1, pp. 315–328, Jan. 2000.

[28] M. Boota, "STRUCTURAL, FERROELECTRIC AND PIEZOELECTRIC properties of epitaxial PMN-PT by PLD," 2014.

[29] L. E. Cross, "Relaxorferroelectrics: An overview," *Ferroelectrics*, vol. 151, no. 1, pp. 305–320, Jan. 1994.

[30] R. Keech *et al.*, "Lateral scaling of Pb(Mg1/3Nb2/3)O3-PbTiO3 thin films for piezoelectric logic applications," *Journal of Applied Physics*, vol. 115, no. 23, p. 234106, Jun. 2014.

[31] N. Banerjee, G. Koster, and G. Rijnders, "Submicron patterning of epitaxial PbZr0.52Ti0.48O3 heterostructures," *Appl. Phys. Lett.*, vol. 102, no. 14, p. 142909, Apr. 2013.

[32] B. Noheda, D. E. Cox, G. Shirane, J. Gao, and Z.-G. Ye, "Phase diagram of the ferro-electric relaxor (1−x)PbMg1/3Nb2/3 O3 − x PbTiO3," *Phys.Rev.B*, vol. 66, p. 054104, 2002.

[33] R. R. Mehta, B. D. Silverman, and J. T. Jacobs, "Depolarization fields in thin ferroelectric films," *Journal of Applied Physics*, vol. 44, no. 8, pp. 3379–3385, Aug. 1973.

[34] S. H. Baek, J. Park, D. M. Kim, and al et, "Giant Piezoelectricity on Si for Hyperactive MEMS," *Science*, vol. 334, pp. 958–961, 2011.

[35] N. Setter *et al.*, "Ferroelectric thin films: Review of materials, properties, and applications," *Journal of Applied Physics*, vol. 100, no. 5, p. 051606, Sep. 2006.

[36] L. W. Martin and A. M. Rappe, "Thin-film ferroelectric materials and their applications," *Nature Reviews Materials*, vol. 2, no. 2, p. natrevmats201687, Nov. 2016.

[37] M. E. Lines and A. M. Glass, *Principles and Applications of Ferroelectrics and Related Materials*. Oxford University Press, 2001.

[38] D. Damjanovic, "Ferroelectric, dielectric and piezoelectric properties of ferroelectric thin films and ceramics," *Rep. Prog. Phys.*, vol. 61, no. 9, p. 1267, 1998.

[39] S. H. Baek *et al.*, "Giant Piezoelectricity on Si for Hyperactive MEMS," *Science*, vol. 334, no. 6058, pp. 958–961, Nov. 2011.

[40] D. Damjanovic, "Comments on Origins of Enhanced Piezoelectric Properties in Ferroelectrics," *IEEE Transactions on Ultrasonics, Ferroelectrics, and Frequency Control*, vol. 56, no. 8, pp. 1574–1585, Aug. 2009.

[41] V. A. Shuvaeva, A. M. Glazer, and D. Zekria, "The macroscopic symmetry of Pb(Mg $_{1/3}$ Nb $_{2/3}$) $_{1-x}$ Ti $_x$ O $_3$ in the morphotropic phase boundary region (x = 0.25–0.5)," *Journal of Physics: Condensed Matter*, vol. 17, no. 37, pp. 5709–5723, Sep. 2005.

[42] F. Li, S. Zhang, Z. Xu, X. Wei, J. Luo, and T. R. Shrout, "Composition and phase dependence of the intrinsic and extrinsic piezoelectric activity of domain engineered (1−x)Pb(Mg1/3Nb2/3)O3−xPbTiO3 crystals," *Journal of Applied Physics*, vol. 108, no. 3, p. 034106, Aug. 2010.

[43] Burns and Dacol, "Glassy polarization behavior in ferroelectric compounds Pb(Mg13Nb23)O3 and Pb(Zn13Nb23)O3 - ScienceDirect," *Solid State Communications*, vol. 48, no. 10, 1983.

[44] F. Li *et al.*, "The origin of ultrahigh piezoelectricity in relaxor-ferroelectric solid solution crystals," *Nature Communications*, vol. 7, p. 13807, Dec. 2016.

[45] R. A. Cowley, S. N. Gvasaliya, S. G. Lushnikov, B. Roessli, and G. M. Rotaru, "Relaxing with relaxors: a review of relaxor ferroelectrics," *Advances in Physics*, vol. 60, no. 2, pp. 229–327, Apr. 2011.

[46] M. Ohring, *Materials Science of Thin Films: Deposition and Structure*. Academic Press, 2002.

[47] H. Brune, "Epitaxial Growth of Thin Films in Solid-Solid Interfaces and Thin Films," Wiley-VCH Verlag GmbH & Co. KGaA, 2014.

[48] K. Oura, M. Katayama, A. V. Zotov, V. G. Lifshits, and A. A. Saranin, "Growth of Thin Films," in *Surface Science: An Introduction*, K. Oura, M. Katayama, A. V. Zotov, V. G. Lifshits, and A. A. Saranin, Eds. Berlin, Heidelberg: Springer Berlin Heidelberg, 2003, pp. 357–387.

[49] Z. Zhang and M. G. Lagally, "Atomistic Processes in the Early Stages of Thin-Film Growth," *Science*, vol. 276, no. 5311, pp. 377–383, Apr. 1997.

[50] G. K. Hubler and D. B. Chrisey, *Pulsed laser deposition of thin films*. New York : J. Wiley, 1994.

[51] H.-U. Krebs *et al.*, "Pulsed Laser Deposition (PLD) -- A Versatile Thin Film Technique," in *Advances in Solid State Physics*, B. Kramer, Ed. Springer Berlin Heidelberg, 2003, pp. 505–518.

[52] M. Kawasaki *et al.*, "Atomic Control of the SrTiO$_3$ Crystal Surface," *Science*, vol. 266, no. 5190, pp. 1540–1542, 1994.

[53] A. Biswas, C.-H. Yang, R. Ramesh, and Y. H. Jeong, "Atomically flat single terminated oxide substrate surfaces," *Progress in Surface Science*, vol. 92, no. 2, pp. 117–141, May 2017.

[54] J. G. Connell, B. J. Isaac, G. B. Ekanayake, D. R. Strachan, and S. S. A. Seo, "Preparation of atomically flat SrTiO3 surfaces using a deionized-water leaching and thermal annealing procedure," *Applied Physics Letters*, vol. 101, no. 25, p. 251607, Dec. 2012.

[55] S. Woo *et al.*, "Surface properties of atomically flat poly-crystalline SrTiO3," *Scientific Reports*, vol. 5, p. 8822, Mar. 2015.

[56] K. D. Vernon-Parry, "Scanning electron microscopy: an introduction," *III-Vs Review*, vol. 13, no. 4, pp. 40–44, Jul. 2000.

[57] D. B. Williams and C. B. Carter, "The Transmission Electron Microscope," in *Transmission Electron Microscopy: A Textbook for Materials Science*, D. B. Williams and C. B. Carter, Eds. Boston, MA: Springer US, 1996, pp. 3–17.

[58] "TEM lamella preparation – CIME." [Online]. Available: https://cime.epfl.ch/electron-microscopy/introduction-to-em/fib-techniques/page-26795-en-html/. [Accessed: 04-Sep-2019].

[59] B. D. Cullity, *Elements of x-ray diffraction*, 2d ed. Reading, Mass: Addison-Wesley Pub. Co, 1978.

[60] H. Bubert and H. Jenett, Eds., *Thin Film Analysis by X-Ray Scattering*. Weinheim: Wiley-VCH, 2002.

[61] C. Suryanarayana and M. G. Norton, *X-ray diffraction, Original text: A Practical Approach*. Springer US, 1998.

[62] P. F. Fewster, "Reciprocal space mapping," *Critical Reviews in Solid State and Materials Sciences*, vol. 22, no. 2, pp. 69–110, Jun. 1997.

[63] P. N. Pala and M. Karabiyik, "Electron Beam Lithography (EBL)," in *Encyclopedia of Nanotechnology*, P. B. Bhushan, Ed. Springer Netherlands, 2012, pp. 718–740.

[64] Frye and Collins, "Oligomeric silsesquioxanes, (HSiO3/2)n |," *Journal of the American Chemical Society*, vol. 92, no. 19, 1970.

[65] D. R. S. Cumming, S. Thoms, J. M. R. Weaver, and S. P. Beaumont, "3 nm NiCr wires made using electron beam lithography and PMMA resist," *Microelectronic Engineering*, vol. 30, no. 1, pp. 423–425, Jan. 1996.

[66] A. E. Grigorescu and C. W. Hagen, "Resists for sub-20-nm electron beam lithography with a focus on HSQ: state of the art," *Nanotechnology*, vol. 20, no. 29, p. 292001, 2009.

[67] P. Güthner and K. Dransfeld, "Local poling of ferroelectric polymers by scanning force microscopy," *Appl. Phys. Lett.*, vol. 61, no. 9, pp. 1137–1139, Aug. 1992.

[68] E. Soergel, "Piezoresponse force microscopy (PFM)," *J. Phys. D: Appl. Phys.*, vol. 44, no. 46, p. 464003, 2011.

[69] B. J. Rodriguez, C. Callahan, S. V. Kalinin, and R. Proksch, "Dual-frequency resonance-tracking atomic force microscopy," *Nanotechnology*, vol. 18, no. 47, p. 475504, 2007.

[70] S. V. Kalinin and A. Gruverman, *Scanning Probe Microscopy: Electrical and Electromechanical Phenomena at the Nanoscale*. New York: Springer-Verlag, 2007.

[71] Z.-G. Ye, "High-Performance Piezoelectric Single Crystals of Complex Perovskite Solid Solutions," *MRS Bulletin*, vol. 34, no. 04, pp. 277–283, Apr. 2009.

[72] M. Boota, E. P. Houwman, M. D. Nguyen, G. Lanzara, and G. Rijnders, "Effect of fabrication conditions on phase formation and properties of epitaxial (PbMg$_{1/3}$Nb$_{2/3}$O$_3$)$_{0.67}$-(PbTiO$_3$)$_{0.33}$ thin films on (001) SrTiO$_3$," *AIP Advances*, vol. 6, no. 5, p. 055303, May 2016.

[73] D. Lavric, R. A. Rao, Q. Gan, J. J. Krajewski, and C.-B. Eom, "Epitaxial thin film heterostructures of relaxor ferroelectric Pb(Mg1/3Nb2/3)O3-PbTiO3," *Integrated Ferroelectrics*, vol. 21, no. 1–4, pp. 499–509, Sep. 1998.

[74] S.-Y. Chen, C.-M. Wang, and S.-Y. Cheng, "The effect of pyrochlore phase on formation mechanism and electrical properties of perovskite PZMN relaxors," *Materials Chemistry and Physics*, vol. 49, no. 1, pp. 70–77, Jun. 1997.

[75] J.-P. Maria, W. Hackenberger, and S. Trolier-McKinstry, "Phase development and electrical property analysis of pulsed laser deposited Pb(Mg1/3Nb2/3)O3–PbTiO3 (70/30) epitaxial thin films," *Journal of Applied Physics*, vol. 84, no. 9, pp. 5147–5154, Oct. 1998.

[76] S. Y. Lee, M. C. C. Custodio, H.-J. Lim, R. S. Feigelson, J.-P. Maria, and S. Trolier-McKinstry, "Growth and characterization of Pb(Mg1/3Nb2/3)O3 and Pb(Mg1/3Nb2/3)O3–PbTiO3 thin films using solid source MOCVD techniques," *Journal of Crystal Growth*, vol. 226, no. 2, pp. 247–253, Jun. 2001.

[77]   S. D. Bu *et al.*, "Perovskite phase stabilization in epitaxial Pb(Mg1/3Nb2/3)O3–PbTiO3 films by deposition onto vicinal (001) SrTiO3 substrates," *Applied Physics Letters*, vol. 79, no. 21, pp. 3482–3484, Nov. 2001.

[78]   S. Yamanaka, T. Maekawa, H. Muta, T. Matsuda, S. Kobayashi, and K. Kurosaki, "Thermophysical properties of SrHfO3 and SrRuO3," *Journal of Solid State Chemistry*, vol. 177, no. 10, pp. 3484–3489, Oct. 2004.

[79]   F. Bai *et al.*, "X-ray and neutron diffraction investigations of the structural phase transformation sequence under electric field in 0.7Pb(Mg1∕3Nb2∕3)-0.3PbTiO3 crystal," *Journal of Applied Physics*, vol. 96, no. 3, pp. 1620–1627, Aug. 2004.

[80]   S.-H. Baek and C.-B. Eom, "Epitaxial integration of perovskite-based multifunctional oxides on silicon," *Acta Materialia*, vol. 61, no. 8, pp. 2734–2750, May 2013.

[81]   G. Koster *et al.*, "Structure, physical properties, and applications of SrRuO3 thin films," *Rev. Mod. Phys.*, vol. 84, no. 1, pp. 253–298, Mar. 2012.

[82]   S. Liu, B. Ma, M. Narayanan, S. Tong, R. Koritala, and U. Balachandran, "Microstructure and electrical properties of LaNiO3 thin films by RF sputtering for the growth of (Pb,La)(Zr,Ti)O3 films on silicon and nickel substrates," *Journal of Vacuum Science & Technology A*, vol. 30, no. 6, p. 061505, Nov. 2012.

[83]   H. Yang, A. Jin, Q. Luo, J. Li, C. Gu, and Z. Cui, "Electron beam lithography of HSQ/PMMA bilayer resists for negative tone lift-off process," *Microelectronic Engineering*, vol. 85, no. 5, pp. 814–817, May 2008.

[84]   L. Yang *et al.*, "Orientation control of LaNiO3 thin films by RF magnetron sputtering with different oxygen partial pressure," *Journal of Crystal Growth*, vol. 311, no. 17, pp. 4241–4246, Aug. 2009.

[85]   N. Wakiya, T. Azuma, K. Shinozaki, and N. Mizutani, "Low-temperature epitaxial growth of conductive LaNiO3 thin films by RF magnetron sputtering," *Thin Solid Films*, vol. 410, no. 1–2, pp. 114–120, May 2002.

[86]   G.-C. Chao and J.-M. Wu, "Effect of LaNiO3 electrode on electrical properties of RF-magnetron-sputtered Pb (Zr, Ti) O3 ferroelectric thin films," *Japanese Journal of Applied Physics*, vol. 40, no. 3R, p. 1306, 2001.

[87] J. Fowlie *et al.*, "Conductivity and Local Structure of LaNiO3 Thin Films," *Adv. Mater.*, p. n/a-n/a, Mar. 2017.

[88] Z. Zhang *et al.*, "Effects of process parameters on the microstructure and conductive properties of LaNiO3 thin films," *OPTOELECTRONICS AND ADVANCED MATERIALS-RAPID COM-MUNICATIONS*, vol. 7, no. 3–4, pp. 201–206, 2013.

[89] K. Tsubouchi *et al.*, "Epitaxial growth and surface metallic nature of LaNiO3 thin films," *Applied Physics Letters*, vol. 92, no. 26, p. 262109, Jun. 2008.

[90] W. L. Li, T. D. Zhang, D. Xu, Y. F. Hou, W. P. Cao, and W. D. Fei, "LaNiO3 seed layer induced enhancement of piezoelectric properties in (1 0 0)-oriented $(1 - x)$BZT–xBCT thin films," *Journal of the European Ceramic Society*, vol. 35, no. 7, pp. 2041–2049, Jul. 2015.

[91] B. G. Chae *et al.*, "Comparative analysis for the crystalline and ferroelectric properties of Pb(Zr,Ti)O3 thin films deposited on metallic LaNiO3 and Pt electrodes," *Thin Solid Films*, vol. 410, no. 1–2, pp. 107–113, May 2002.

[92] M.-S. Chen, T.-B. Wu, and J.-M. Wu, "Effect of textured LaNiO3 electrode on the fatigue improvement of Pb(Zr0.53Ti0.47)O3 thin films," *Applied Physics Letters*, vol. 68, no. 10, pp. 1430–1432, Mar. 1996.

[93] A. FERRI, A. D. COSTA, R. DESFEUX, M. DETALLE, G. S. WANG, and D. RèMIENS, "NANOSCALE INVESTIGATIONS OF ELECTRICAL PROPERTIES IN RELAXOR Pb(Mg1/3Nb2/3)O3-PbTiO3 THIN FILMS DEPOSITED ON PLATINUM AND LaNiO3 ELECTRODES BY MEANS OF LOCAL PIEZOELECTRIC RESPONSE," *Integrated Ferroelectrics*, vol. 91, no. 1, pp. 80–96, May 2007.

[94] L. J. McGilly, P. Yudin, L. Feigl, A. K. Tagantsev, and N. Setter, "Controlling domain wall motion in ferroelectric thin films," *Nat Nano*, vol. 10, no. 2, pp. 145–150, Feb. 2015.

[95] L. J. McGilly, L. Feigl, and N. Setter, "Domain nucleation behavior in ferroelectric films with thin and ultrathin top electrodes versus insulating top layers," *Thin Solid Films*, vol. 636, pp. 214–219, Aug. 2017.

[96] U. Gabor *et al.*, "Structural peculiarities of 0.67 Pb(Mg1/3Nb2/3)O3–0.33 PbTiO3 thin films grown directly on SrTiO3 substrates," *Journal of the European Ceramic Society*, vol. 38, no. 13, pp. 4453–4462, Oct. 2018.

[97] X. Di and P. Muralt, "Highly (100)-oriented metallic LaNiO3 grown by RF magnetron sputtering," in *2017 Joint IEEE International Symposium on the Applications of Ferroelectric (ISAF)/International Workshop on Acoustic Transduction Materials and Devices (IWATMD)/Piezoresponse Force Microscopy (PFM)*, 2017, pp. 33–36.

[98] C.-C. Yang, M.-S. Chen, T.-J. Hong, C.-M. Wu, J.-M. Wu, and T.-B. Wu, "Preparation of (100)-oriented metallic LaNiO3 thin films on Si substrates by radio frequency magnetron sputtering for the growth of textured Pb(Zr0.53Ti0.47)O3," *Applied Physics Letters*, vol. 66, no. 20, pp. 2643–2645, May 1995.

[99] K. M. Satyalakshmi *et al.*, "Epitaxial metallic LaNiO3 thin films grown by pulsed laser deposition," *Applied Physics Letters*, vol. 62, no. 11, pp. 1233–1235, Mar. 1993.

[100] H. Suzuki *et al.*, "Orientation control and electrical properties of PZT/LNO capacitor through chemical solution deposition," *Journal of the European Ceramic Society*, vol. 26, no. 10–11, pp. 1953–1956, 2006.

[101] D. Rémiens *et al.*, "PMN-PT thin films grown by sputtering on silicon substrate: influence of the annealing temperature on the physico-chemical and electrical properties of the films," *Res. Chem. Intermed.*, vol. 34, no. 2–3, pp. 201–215, Feb. 2008.

[102] K. Zheng, J. Lu, and J. Chu, "A Novel Wet Etching Process of Pb(Zr,Ti)O3 Thin Films for Applications in Microelectromechanical System," *Jpn. J. Appl. Phys.*, vol. 43, no. 6S, p. 3934, Jun. 2004.

[103] S. Ezhilvalavan and V. D. Samper, "Ferroelectric properties of wet-chemical patterned PbZr0.52Ti0.48O3 films," *Appl. Phys. Lett.*, vol. 86, no. 7, p. 072901, Feb. 2005.

[104] L. Che, E. Halvorsen, and X. Chen, "An optimized one-step wet etching process of Pb(Zr0.52Ti0.48)O3thin films for microelectromechanical system applications," *J. Micromech. Microeng.*, vol. 21, no. 10, p. 105008, Sep. 2011.

[105] J. Agnus, I. A. Ivan, and S. Queste, "Dry etching of single crystal PMN-PT piezoelectric material," in *2011 IEEE 24th International Conference on Micro Electro Mechanical Systems (MEMS)*, 2011, pp. 237–240.

[106] I. A. Ivan, J. Agnus, and P. Lambert, "PMN–PT (lead magnesium niobate–lead titanate) piezoelectric material micromachining by excimer laser ablation and dry etching (DRIE)," *Sensors and Actuators A: Physical*, vol. 177, pp. 37–47, Apr. 2012.

[107] J. Baborowski, "Microfabrication of Piezoelectric MEMS," *Journal of Electroceramics*, vol. 12, no. 1, pp. 33–51, Jan. 2004.

[108] S. Mancha, "Chemical etching of thin film PLZT," *Ferroelectrics*, vol. 135, no. 1, pp. 131–137, Oct. 1992.

[109] D. RÉMIENS *et al.*, "Piezoelectric Response of Pzt Nanostructures Obtained by Focused Ion Beam," *Integrated Ferroelectrics*, vol. 100, no. 1, pp. 16–25, Dec. 2008.

[110] D. Vijay, S. Desu, and W. Pan, "Reactive Ion Etching of Lead Zirconate Titanate (PZT) Thin Film Capacitors," *Journal of The Electrochemical Society*, vol. 140, 1993.

[111] Y. Lin, Q. Liu, T. Tang, X. Yao, and W. Huang, "Magnetically Enhanced Reactive Ion Etching of Lead Zirconate Titanate Thin Film by CHF3 Plasma," *Jpn. J. Appl. Phys.*, vol. 39, no. 1R, p. 320, Jan. 2000.

[112] J. W. Lau and J. M. Shaw, "Magnetic nanostructures for advanced technologies: fabrication, metrology and challenges," *Journal of Physics D: Applied Physics*, vol. 44, no. 30, p. 303001, Aug. 2011.

[113] J. Peng, C. Chao, J. Dai, H. L. W. Chan, and H. Luo, "Micro-patterning of 0.70Pb(Mg1/3Nb2/3)O3–0.30PbTiO3 single crystals by ultrasonic wet chemical etching," *Materials Letters*, vol. 62, no. 17, pp. 3127–3130, Jun. 2008.

[114] S. Q. Lee, H. J. Kim, K. H. Park, Y. K. Hong, and K. S. Moon, "High-sensitive MEMS acoustic sensor using PMN-PT single-crystal diaphragm," in *Optomechatronic Actuators, Manipulation, and Systems Control*, 2006, vol. 6374, p. 637409.

[115] A. Stanishevsky, B. Nagaraj, J. Melngailis, R. Ramesh, L. Khriachtchev, and E. McDaniel, "Radiation damage and its recovery in focused ion beam fabricated ferroelectric capacitors," *Journal of Applied Physics*, vol. 92, no. 6, pp. 3275–3278, Aug. 2002.

[116] V. Nagarajan *et al.*, "Dynamics of ferroelastic domains in ferroelectric thin films," *Nature Materials*, vol. 2, no. 1, pp. 43–47, Jan. 2003.

[117] W. Lee *et al.*, "Individually addressable epitaxial ferroelectric nanocapacitor arrays with near Tb inch−2 density," *Nature Nanotechnology*, vol. 3, no. 7, pp. 402–407, Jul. 2008.

[118] N. Banerjee, M. Huijben, G. Koster, and G. Rijnders, "Direct patterning of functional interfaces in oxide heterostructures," *Appl. Phys. Lett.*, vol. 100, no. 4, p. 041601, Jan. 2012.

[119] J. Golden, H. Miller, D. Nawrocki, and J. Ross, "Optimization of Bi-layer Lift-Off Resist Process," *http://www.microchem.com/*, p. 4.

[120] H. Namatsu, T. Yamagouchi, K. Nagase, and K. Kurihara, "Nano-patterning of a hydrogen silsesquioxane resist with reduced linewidth fluctuations," *Microelectronic Engineering*, vol. 41–42, p. 1998.

[121] J. K. W. Yang and K. K. Berggren, "Using high-contrast salty development of hydrogen silsesquioxane for sub-10-nm half-pitch lithography," *J.Vac.Sci.Techn.B*, vol. 25, pp. 2025–2029, 2007.

[122] M. D. Groner, F. H. Fabreguette, J. W. Elam, and S. M. George, "Low-Temperature Al_2O_3 Atomic Layer Deposition," *Chemistry of Materials*, vol. 16, no. 4, pp. 639–645, Feb. 2004.

[123] "X-ray diffraction imaging (X-ray topography)." [Online]. Available: http://www.esrf.eu/home/UsersAndScience/Experiments/StructMaterials/ID19/Techniques/Diffraction/Overview.html. [Accessed: 27-Sep-2019].

[124] N. Banerjee, "Epitaxial perovskite oxide devices fabricated by lift-off technology," info:eu-repo/semantics/doctoralThesis, Wöhrmann Print Services, Zutphen, 2014.

[125] "ASYELEC.01-R2 - Probes." [Online]. Available: https://afmprobes.asylumresearch.com/probes/asyelec-01-r2.html. [Accessed: 20-Mar-2018].

[126] "SCANASYST-FLUID+ - Bruker AFM Probes." [Online]. Available: https://www.bruker-afmprobes.com/p-3728-scanasyst-fluid.aspx. [Accessed: 29-Sep-2019].

[127] "HQ:NSC35/Pt." [Online]. Available: www.spmtips.com/afm-tip-hq-nsc35-pt. [Accessed: 29-Sep-2019].

[128] Asylum Research, "Asylum Research Applications Guide v16A." 2018.

[129] S. Hong *et al.*, "Principle of ferroelectric domain imaging using atomic force microscope," *Journal of Applied Physics*, vol. 89, no. 2, pp. 1377–1386, Jan. 2001.

[130] S. Hong, H. Shin, J. Woo, and K. No, "Effect of cantilever–sample interaction on piezoelectric force microscopy," *Applied Physics Letters*, vol. 80, no. 8, pp. 1453–1455, Feb. 2002.

[131] M.-H. Zhang *et al.*, "(K,Na)NbO₃-based Lead-free Piezoelectric Materials: An Encounter with Scanning Probe Microscopy," *J. Korean Ceram. Soc*, vol. 54, no. 4, pp. 261–271, Jul. 2017.

[132] P. Miao *et al.*, "Ferroelectricity and Self-Polarization in Ultrathin Relaxor Ferroelectric Films," *Scientific Reports*, vol. 6, p. 19965, Jan. 2016.

[133] C. Lichtensteiger, S. Fernandez-Pena, C. Weymann, P. Zubko, and J.-M. Triscone, "Tuning of the Depolarization Field and Nanodomain Structure in Ferroelectric Thin Films," *Nano Lett.*, vol. 14, no. 8, pp. 4205–4211, Aug. 2014.

[134] S. Fernandez-Peña, C. Lichtensteiger, P. Zubko, C. Weymann, S. Gariglio, and J.-M. Triscone, "Ferroelectric domains in epitaxial PbxSr1−xTiO3 thin films investigated using X-ray diffraction and piezoresponse force microscopy," *APL Materials*, vol. 4, no. 8, p. 086105, Aug. 2016.

[135] "Gwyddion – Free SPM (AFM, SNOM/NSOM, STM, MFM, …) data analysis software." [Online]. Available: http://gwyddion.net/. [Accessed: 28-Sep-2019].

[136] B. J. Rodriguez, C. Callahan, S. V. Kalinin, and R. Proksch, "Dual-frequency resonance-tracking atomic force microscopy," *Nanotechology*, vol. 18, no. 47, p. 475504, 2007.

[137] K. Brinkman, Y. Wang, D. Su, A. K. Tagantsev, P. Muralt, and N. Setter, "The Impact of chemical ordering on the dielectric properties of lead scandium tantalate Pb„Sc1/2Ta1/2…O3 thin films," *J.Appl.Phys.*, vol. 102, p. 044110, 2007.

[138] R. Keech *et al.*, "Declamped Piezoelectric Coefficients in Patterned 70/30 Lead Magnesium Niobate–Lead Titanate Thin Films," *Adv. Funct. Mater.*, p. n/a-n/a, Jan. 2017.

[139] S. Buhlmann, B. Dwir, J. Baborowski, and P. Muralt, "Size effect in mesoscopic epitaxial ferroelectric structures: Increase of piezoelectric response with decreasing feature size," *Applied Physics Letters*, vol. 80, no. 17, pp. 3195–3197, Apr. 2002.

[140] J. F. Ihlefeld, D. T. Harris, R. Keech, J. L. Jones, J.-P. Maria, and S. Trolier-McKinstry, "Scaling Effects in Perovskite Ferroelectrics: Fundamental Limits and Process-Structure-Property Relations," *J. Am. Ceram. Soc.*, p. n/a-n/a, Jul. 2016.

[141] G. A. Chahine *et al.*, "Imaging of strain and lattice orientation by quick scanning X-ray microscopy combined with three-dimensional reciprocal space mapping," *J Appl Cryst*, vol. 47, no. 2, pp. 762–769, Apr. 2014.

[142] "ID01 - Microdiffraction imaging." [Online]. Available: http://www.esrf.eu/UsersAndScience/Experiments/XNP/ID01. [Accessed: 27-Sep-2019].

[143] U. K. Bhaskar *et al.*, "A flexoelectric microelectromechanical system on silicon," *Nat Nano*, vol. advance online publication, Nov. 2015.

Xiao DI

MSc in Electrical Engineering

xiaodi.epfl@gmail.com

Rue de Bassenges 2, Ecublens VD, CH-1024, Switzerland

Education

10.2015 – present *Lausanne, Switzerland*	**Swiss Federal Institute of Technology Lausanne (EPFL)**: *PhD Student in Microelectronics and Microsystems* Electroceramic Thin Films Laboratory, advisor: Prof. Paul Muralt. Co-advisor: Prof. Dragan Damjanovic
09.2009 – 11.2011 *Lausanne, Switzerland* *Grennoble, France* *Turin, Italy*	*International Master Degree in Micro Nanotechnologies for Integrated Systems* **Swiss Federal Institute of Technology Lausanne (EPFL)**, **Grenoble Institute of Technology (INPG) and Polytechnic University of Turin (POLITO)**
09.2005 – 07.2009 *Harbin, China*	**Harbin Institute of Technology**: *Bachelor Degree in Mechanical Engineering*

Research and Work Experience

10.2015 – present *Lausanne, Switzerland*	**EPFL**: *research assistant in Microelectronics and Microsystems* Piezoelectric and ferroelectric thin film deposition and characterization, micro- and nanofabrication, cleanroom and thin film processing. Finite element modeling. Advisor: Prof. Paul Muralt. Co-advisor: Prof. Dragan Damjanovic
09.2012 – 07.2015 *Hong Kong, China*	**City University of Hong Kong**: *research assistant* Design piezoelectric MEMS resonators for RF applications. Supervisor: Prof. Joshua E.Y. Lee
03.2011 – 09.2011 *Zurich, Switzerland*	**Swiss Federal Institute of Technology Zurich (ETHZ)**: *master thesis* Thermal actuator based microsystem platform design for CNT-transistor characterizations under tensile strain. Supervisor: Prof. Christopher Hierold

Languages

Chinese	native speaker	**English**	fluent
French	A1 level		

Computer skills

Programming   Matlab, Python, Mathematica, Labview.

Software   Microsoft Office suite, COMSOL Multiphysics, photolithography mask design, Adobe design suite.

Publications

Peer-reviewed journals:

1. X. Di, C.S. Sandu, D. Park and P. Muralt, Study of nanostructured single crystal PMN-PT films: fabrication and characterizations, ACS Nano (submitted).
2. C.S. Sandu, F. Parsapour, X. Di, R. Nigon, L. Riemer, T. LaGrange and P. Muralt, "Reduction of ab-normal oriented grains in Al0.62Sc0.38N thin films by applying RF-bias", Thin Solid Films. (under review)

Conference proceedings and presentations:

1. X. Di, C.S. Sandu, J. Guo, D. Park and P. Muralt, Epitaxial Growth of PMN-PT Thin Films and Nanostructures, in 2019 ISAF-ICE-EMF-IWPM-PFM (F2CP2) Joint Conference, Lausanne Switzerland, 14 - 19 July, 2019.
2. X. Di and P. Muralt, " Epitaxially grown PMN-PT nano structures" in The 16th International Workshop on Nanomechanical Sensors, Lausanne, Switzerland, June 19-21, 2019
3. X. Di and P. Muralt, "Sub-micron Ferroelectric Structures Fabricated by Lift-off Method," in The 44th International Conference on Micro and Nano Engineering, Copenhagen, Denmark, Sept. 24-27, 2018.
4. X. Di and P. Muralt, Growth and PFM study of PMN-PT thin films, in 2018 IEEE ISAF-FMA-AMF-AMEC-PFM (IFAAP) Joint Conference, Hiroshima Japan, May 27 – June 1, 2018.
5. X. Di and P. Muralt, Highly (100)-oriented metallic LaNiO3 grown by RF magnetron sputtering, in Proceedings of 2017 IEEE ISAF- IWATMD - PFM Joint conference, Atlanta, GA, USA, May 7-11, 2017, pp. 3336.
6. X. Di, and J. E.-Y. Lee, "Reducing anchor loss in piezoelectric-on-silicon laterally vibrating resonators by combination of etched-slots and convex edges," in proceedings of The 18th Int. Conf. on Solid-State Sensors, Actuators and Microsystems (Transducers 2015). (pp. 2033 - 2036). Anchorage, AK, USA, 21-25 Jun 2015.
7. X. Di, and J. E.-Y. Lee, "Reducing anchor loss in contour mode resonators", in Materials Workshop, Lysin Switzerland, Dec 13-15, 2015.
8. H. Zhu, X. Di, and J. E.-Y. Lee, "2D phononic crystal for anchor loss reduction in a 142MHz AlN-on-silicon micromechanical resonator," in The 40th International Conference on Micro and Nano Engineering, Lausanne, Switzerland, Sept. 22-26, 2014.
9. S.-W. Lee, X. Di, M. Muoth, C. Roman, S. Truax, and C. Hierold, "Embedded MEMS actuators for CNT straining tests," in Annual Meeting of nano-tera.ch, Zurich, Switzerland, April 26, 2012.